SCUOLA DI DOTTORATO
UNIVERSITÀ DEGLI STUDI DI MILANO-BICOCCA

Dipartimento di / Department of

Physics “G. Occhialini”

Dottorato di Ricerca in / PhD program Physics and Astronomy Ciclo / Cycle XXXVI
Curriculum in Applied Physics and Electronics

Design and development of a thermal neutron GEM detector based on multi-layer $^{10}B_4C$ technology.

Cognome / Surname Cancelli Nome / Name Stephanie

Matricola / Registration number 761720

Tutore / Tutor: Dr. Marco Tardocchi

Supervisor: Prof. Gabriele Croci

Coordinatore / Coordinator: Prof. Stefano Ragazzi

ANNO ACCADEMICO / ACADEMIC YEAR 2022/2023

Contents

Abstract

The work presented in this thesis is related to the development and characterisation of a Gas Electron Multiplier (GEM) detector for thermal neutrons.

Thermal neutron detection is nowadays mostly based on ^{3}He, a noble gas with a high neutron cross-section (5330 b for thermal neutrons). Since 2010, the ^{3}He availability is rapidly decreased due to its use in the strategic military field, thus new alternatives have been explored to compensate the ^{3}He shortage. Moreover, the recent upgrades of the neutron facilities require new dedicated neutron detectors with good features, such as a high detection efficiency and a good spatial resolution.

Based on these premises, several neutron converters have been studied and coupled with detectors. GEM detectors have been optimised for thermal neutrons through the use of the ^{10}B, where neutrons are converted via the nuclear reaction ^{10}B(n,α)^{7}Li.

This PhD thesis shows a new GEM detector optimised for neutron detection thanks to the use of the innovative boron-GEM foils, i.e. GEM foils covered on both sides with a boron layer.

The new detector, named MBGEM, has been developed to reach a high detection efficiency through stacking the boron GEM foils, since they increase the neutron conversion. The detector is made of two parts: the six boron GEM foils stack and the three standard GEM foils stack. The boron GEM foils stack is the neutron conversion region, while the standard GEM foils stack is necessary to multiply the electrons arriving from the boron GEM foils stack. During my PhD work, the detector has been assembled at the Milano-Bicocca University and Istituto per la Scienza e la Tecnologia dei Plasmi (ISTP) of CNR, where the preliminary tests have been conducted.

The detector has been preliminarily characterised with an X-ray source to study the capability to extract electrons from the GEM foil holes. This study has confirmed the good operation of the two stacks coupling (conversion stack and electron multiplication stack), in fact the primary electrons produced inside the boron stack are guided with a

unitary gain and without losses through the boron GEM until they reach the triple GEM foils, where electrons are multiplied.

Then, the study of the capability to sustain high count rates has been performed with a thermal neutron beam at the TRIGA Mark II reactor at the Laboratorio Energia Nucleare Applicata (L.E.N.A.). The MBGEM detector has shown a linear response up to a thermal neutron flux of 10^6 n/s*cm^2.

The final detector characterisation has been performed with a pulsed neutron source, the ISIS Neutron and Muon Source (UK), with a thermal and epithermal neutron beam of 10^7 n/s*cm^2 at the VESUVIO experiment. The MBGEM detector main features have been determined with a series of measurements. In particular, it has been estimated the detection efficiency of neutrons from 0.5 Å up to 6 Å, the detector stability during time and the detector capability to discriminate the neutrons from gamma rays.

The data analysis highlights a detection efficiency of 16% at 1.8 Å(25 meV), a detector stability of 99% and capability to discriminate gamma rays from neutrons is $1.36 * 10^{-5}$ γ/n.

The good properties shown by the MBGEM detector suggest the possibility to use it to perform different experiments at spallation sources, where detectors capable to sustain high fluxes are required. In particular, it will be possible to use the MBGEM to perform experiments in transmission geometry aimed to determine the total neutron cross section of samples, but also for SANS (Small-Angle Neutron Scattering), where detectors need to sustain high count rates.

Chapter 1

Neutron interaction with matter

In 1932 Chadwick supposed the existence of neutrons and he confirmed his prevision the same year with the paper *"The existence of a Neutron"*:

> In conclusion, I may restate briefly the case for supposing that the radiation the effects of which have been examined in this paper consists of neutral particles rather than of radiation quanta. Firstly, there is no evidence from electron collisions of the presence of a radiation of such a quantum energy as is necessary to account for the nuclear collisions. Secondly, the quantum hypothesis can be sustained only by relinquishing the conservation of energy and momentum. On the other hand, the neutron hypothesis gives an immediate and simple explanation of the experimental facts; it is consistent in itself and it throws new light on the problem of nuclear structure. [1]

Since 1932 neutron physics is largely advanced and neutrons have demonstrated to have peculiar properties which make them perfect tools to study both the structure and dynamics of matter.

The neutron is a subatomic particle, made of two down quarks and one up quark; it is a Fermion with no charge and it has a mass of 939 $\mathrm{MeV/c^2}$.

As free particles, neutrons decay $\beta-$ via the reaction:

$$\mathrm{n} \rightarrow \mathrm{p} + \mathrm{e}^- + \bar{\nu_e}$$

with a half life (τ) of 882 s, while inside the nucleus neutrons are stable particles [2].

Neutrons are conventionally divided into categories based on their kinetic energy $\mathrm{E_n}$:

- Cold neutrons: $\mathrm{E_n} < 25\mathrm{meV}$.

- Thermal neutrons: $\simeq$ 25meV.
- Epithermal neutrons: up to 100 eV.
- Fast neutrons: from 100 eV to MeV.

Cold, thermal and epithermal ones are also called *slow neutrons*.

1.1 Neutron Sources

The main neutron sources described in this section are: spontaneous fission sources, (α,n) nuclear reaction sources, photoneutron emission, neutron tube and neutron pulsed sources. [2]

1.1.1 Spontaneous Fission

Heavy nuclei, with an atomic number A higher than 200 (transuranic heavy nuclei), are characterized by a higher neutron(N)/proton(Z) ratio than light nuclei. Under this condition same nuclei do not have spherical shape, but they have an elliptical shape due to their large potential barrier, so it is energetically convenient for such nuclei to divide in two parts. The two fission fragments are emitted back to back due to the momentum conservation and these products are lighter than the initial nuclei [3]. During this process, the excess neutrons and the energy are released.

A common spontaneous fission neutron source is ^{252}Cf, which has half-life (τ) of 2.65 y and two decay channels: either α-emission and neutron emission with branching ratio (B.R.) of 96.9% and 3.1% respectively; one microgram of the sample produces 10^6n/s.

1.1.2 Radioisotopes (α, n) Sources

α particles are generated from the decay of heavy nuclei and they can produce neutrons via reactions with other nuclei. Thus, using an appropriate target it is possible to create a neutron source. The chosen target is generally beryllium in order to produce neutrons from the following reaction:

$$\alpha +^{9}\mathrm{Be} \rightarrow^{12}\mathrm{C} + \mathrm{n}$$

with a Q-value (the available energy from the reaction) of 5.71 MeV. The commonly used α-sources are ^{239}Pu (τ of 24000 y) and ^{241}Am (τ of 433 y); the choice between them depends on availability, costs and half-life.

1.1.3 Photoneutron Sources

Using the interaction between photons and an appropriate material, such as berillium or deuterium, it is possible to produce neutrons.

Target nuclei absorb gamma ray photons and they de-excite emitting free neutrons; the main reactions are:

- $h\nu + ^9\mathrm{Be} \rightarrow ^8\mathrm{Be} + \mathrm{n}$ Q-value=-1.666 MeV
- $h\nu + ^2\mathrm{H} \rightarrow \mathrm{H} + \mathrm{n}$ Q-value=-2.226 MeV

The advantage of using this technique is the emission of approximately monoenergetic neutrons due to the use of monoenergetic gamma rays and the neutron yield (Y_n) is $10^{-6}\mathrm{n}/\gamma$.

1.1.4 Neutron Tube

The system is based on the acceleration of deuterium and its collision with a target. Generally targets are either deuterium or tritium, giving the following neutron-producing reactions:

- $\mathrm{D} + \mathrm{D} \rightarrow ^3\mathrm{He} + \mathrm{n}$ Q-value=3.26 MeV.
- $\mathrm{D} + \mathrm{T} \rightarrow ^4\mathrm{He} + \mathrm{n}$ Q-value=17.6 MeV.

Neutrons are emitted in D-D and D-T reaction with an energy of 2.5 MeV and 14.2 MeV and neutron yields are $\mathrm{Y}_n = 10^9\mathrm{n/s}$ and $\mathrm{Y}_n = 10^{11}\mathrm{n/s}$ respectively.

1.1.5 Pulsed Source

Pulsed neutron sources[4] are made of the components in figure 1.1; neutrons are produced by nuclear reactions following collisions between an accelerated pulsed particle beam and a target, which creates fast neutrons (MeV energies). Pulsed sources are produced using either photoneutron from electrons (as explained in the subsection 1.1.3) or spallation by protons or even fission. The main facilities associated to these approaches are electron linear accelerator, proton spallation sources and some kind of pulsed reactors. To perform some kind of experiments, such as the neutron scattering, it is necessary to have thermal neutrons and this slowdown is generally performed by a polyethylene or water moderator.

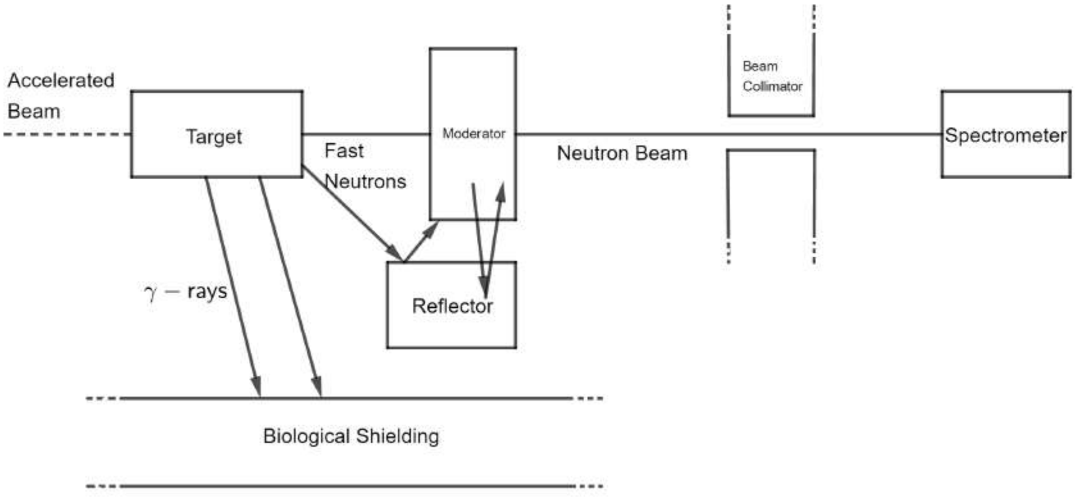

Figure 1.1: Neutron pulsed source scheme.

Around the moderator, some reflectors scatter back fast neutrons escaping from the moderator itself and a biological shield protect users and instrumentation from the radiation and reduces the background given by fast neutrons.

Considering an ideal spectrum of a pulsed source [4], it shows the different contribution from fast, epithermal and thermal neutrons; in conclusion the spectrum shows the advantage of the use of this source, in fact it is possible to remove the fast neutron background from the spectrum just by not collecting the first neutrons which reach the detector.

Proton Spallation Sources

The word *spallation* comes to the verb *to spall*, in fact during this reaction prontons enter like a splinter into the nuclei. To obtain this reaction, prontons must penetrate nuclei, and they must have a very high energy, in the order 800 MeV (grater than electrons from accelerator, 50 MeV). Since the proton range is in the order of tens of centimeters, this reaction affects many number of nuclei; in fact, the neutron yield is 30 neutrons per protons.

Pulsed proton facilities are made of a proton accelerator. Then, proton bunches are extracted and sent to the neutron target.

1.2 Neutron interaction with matter

Since neutrons have no charge, they do not interact with matter through Coulomb force but the interaction is only between neutrons and nuclei in the range of Strong interaction (about 10^{-15}m).

The main parameter, which describes the probability of the interaction between neutrons and nuclei, is the *cross section* (σ): it has the unit of an area and the meaning of a probability and it is usually measured in barns ($10^{-28}\mathrm{m}^2$).

As described in the first section, neutrons have different energies and this implies that neutrons have different ways to interact with matter that depend on their energies.

The main interaction mechanisms are:

- Elastic scattering: A(n,n)A. During this process both kinetic energy and momentum are conserved. This process is predominant for slow/thermal neutrons.
- Inelastic scattering: A(n,n')A. The final nucleus is in an excited state and deexcites emitting gamma rays. This process is relevant for fast neutrons.
- Absorption (or radiative capture): n+(Z,A)→(Z,A+1)+γ, where Z is the number of protons. In this case σ has a dependence on the velocity of neutrons: $\sigma \propto 1/\mathrm{v_n} \propto 1/\sqrt{\mathrm{E_n}}$.
- Capture with particle emission: it involves nuclear reactions of type e.g. (n,p), (n,D), (n,α). In this process $\sigma \propto 1/\mathrm{v_n}$.

1.3 Slow neutron detection

Since my PhD work is related to the realization of slow neutron detectors, in this section it is given a general overview on the slow neutron detection methods.

The slow neutron detection is based on the "conversion" of neutrons into charged particles in order to collect them and to obtain an electrical signal. The nuclear reaction must be chosen in order to have σ as high as possible (see fig.1.2), thus the detector can be built with small dimensions without losing the detection efficiency (defined as the ratio between the number of the recorded pulses and number of the incident particles on the detector).

The possible reaction products from the collision between target nuclei and neutrons are recoiling nuclei, protons, alpha particles and fission fragments.

For slow neutron detection the most commonly used converter reactions are:

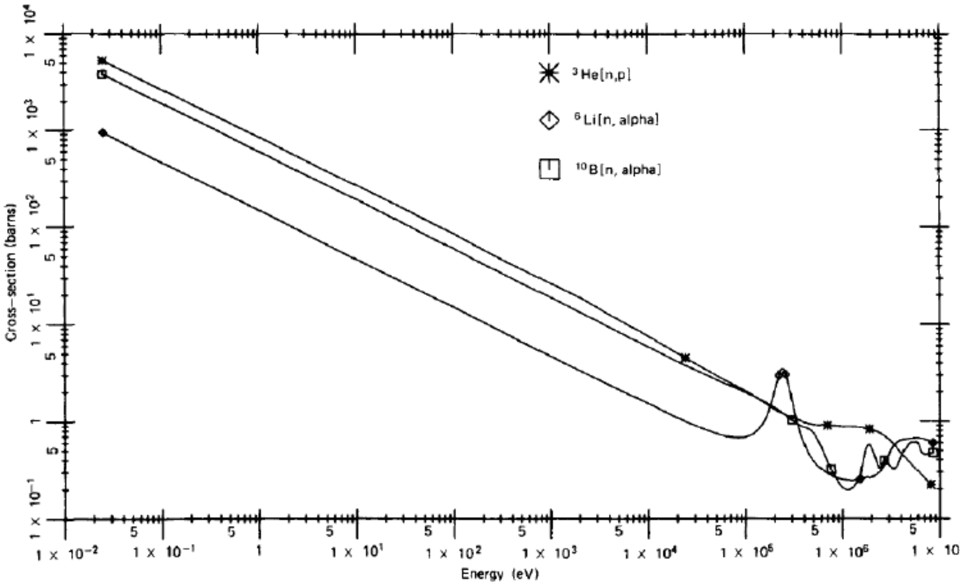

Figure 1.2: Neutron cross section of the three main nuclear reaction used to detect slow neutron:^{3}He(n,p), $^{10}\mathbf{B}(n,\alpha)$ and $^6\mathbf{Li}(n,\alpha)$ with a σ of 5330, 3840 and 940 barns respectively. [2]

- **The $^{10}\mathbf{B}(n,\alpha)^7\mathbf{Li}$ nuclear reaction** :

$$^{10}\mathrm{B}+\mathrm{n}=\begin{cases} ^7\mathrm{Li}+\alpha & \text{Q-value=2.792 MeV ground state, B.R.= 6\%} \\ ^7\mathrm{Li}^*+\alpha & \text{Q-value=2.31 MeV excited state, B.R.= 94\%} \end{cases}$$

The Q-value energy is much higher than the neutron kinetic energy, so the energy given to the two products is about just the Q-value itself. Because of momentum conservation, the two products are emitted back-to-back and the energy is divided as $\mathrm{E_{Li}} = 0.84$MeV and $\mathrm{E}_\alpha = 1.47$MeV.

σ for thermal neutrons (σ_{TH}) is 3840 barns and decreases rapidly with increasing of the neutron energy (see fig.1.2).

- **The $^6\mathbf{Li}(n,\alpha)^3\mathbf{He}$ nuclear reaction**:

$$^6\mathrm{Li}+\mathrm{n}={}^3\mathrm{H}+\alpha \quad \text{Q-value=4.78 MeV}$$

The two products are emitted back-to-back with the following energies: $\mathrm{E_{3_H}} = 2.73$MeV and $\mathrm{E}_\alpha = 2.05$MeV. σ_{TH} is 940 barns, but this low value (with respect to the previous σ_{TH} of boron reaction) is compensated by the higher Q-value which means a high energy given to the products.

- **The ^{3}He$(n,p)^3$H nuclear reaction**:

  $$^3\mathrm{He} + \mathrm{n} = {}^3\mathrm{H} + \mathrm{p} \quad \text{Q-value=0.764 MeV}$$

  The products emitted back-to-back have energies of: $\mathrm{E}_{3_\mathrm{H}} = 0.191\mathrm{MeV}$ and $\mathrm{E}_\mathrm{p} = 0.573\mathrm{MeV}$. σ_{TH} is 5330 barns and it decreases with a 1/v dependence.

- **Neutron capture reaction of ^{157}Gd**: ^{157}Gd has a σ of 250000 barns for thermal neutron capture. The charged products from this reaction are gamma rays and conversion electrons, in particular electrons of 72 keV. These products give a contribution to gamma background grater than the previous reactions.

- **Fission reactions induced from neutrons**: Sometimes it is convenient to use fissile materials, such as ^{233}U, ^{235}U and ^{239}Pu, due to their large fission cross-sections for slow neutrons. The main feature of this fission reaction is the large Q-value (around 200 MeV), thus the fission fragments release enough energy to produce a signal easily distinguishable from background signals, given for example by other reactions or gammas.

1.4 Slow Neutron detectors

In the following subsection, the operation principle of the most common slow neutron detectors based on the reactions described in the previous section will be reported.

1.4.1 Boron-based neutron detector: the BF$_3$ tube

The BF$_3$ is a gas detector operating in the proportional regime (see the next chapter). The advantage to use this device is that the active area is the entire detector. The device is a cylinder tube made of an outer aluminum cathode and smaller inner central wire anode.

Neutrons are converted between cathode and anode; then, alpha and lithium are emitted back to back and released inside the gas, ionising it. If the tube dimensions are very larger than the alpha range free path, alpha and lithium release all their energy inside the detector and the energy spectrum shows the full energy for the exited state at 2.31 MeV and for the ground state at 2.79 MeV. If this condition is not realised, the BF$_3$ has an effect, named *the Wall effect*, that affects the energy spectrum. This effect happens when alpha or lithium particles are produced near the tube wall, then the

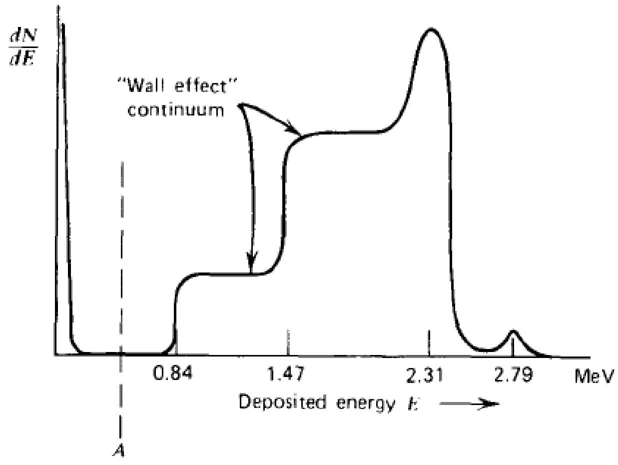

Figure 1.3: Representation of a typical BF_3 tube energy spectrum where the energy peaks and the wall effect are shown. [2]

particles travel inside the gas releasing only a part of their energy before being absorbed by the wall. As consequence, the energy spectrum shows a continuum before the full energy peak, from $E_{Li} = 0.84MeV$ (only the Lithium is detected) until $E_{Li} + E_{\alpha}$ and from $E_{\alpha} = 1.47MeV$ until $E_{\alpha} + E_{Li}$.

This detector is used as a counter, since it does not give any information about the energy spectrum of the initial neutrons. The detection efficiency of thermal neutrons for a 30 cm long tube filled with 80 kPa BF_3 is around 90% and 3.6% for 100 eV (only for neutrons that travel along the full tube length). If neutrons move along the perpendicular axis of the tube or near the end of the tube, the detection efficiency decrease due to the presence of a dead space inside the detector.

The BF_3 tubes are insensitive to gammas, since gammas have a low stopping power, then they release only small fraction of their energy inside the detector. This energy can be easily discriminate setting a suitable LLD.

1.4.2 Lithium-based scintillators

The most common slow neutron detectors based on the lithium reaction are scintillators, in particular crystalline lithium iodide. The energy spectrum shows only the full energy peak at 4.78 MeV, since lithium products reactions does not have excited state

The two products energies are fully deposited in the detector (due to their negligible path inside the crystal), then the spectrum it is not affected by the wall effect as in gas detectors. For these detectors, it must be taken into account the scintillation efficiencies and, for the lithium iodide, electrons and charged particles have the same values (electrons of 4.71 MeV and alphas of 4.78 MeV provide the same light).

Thus, gammas produce pulses with height proportional to their energies and, as consequence, the gamma discrimination is not so immediate as in gas detector, where gammas release only a small fraction of their energies.

1.4.3 The ^{3}He tubes

The ^{3}He tubes are gaseous detectors, which operate as proportional counters (see Chapter 2). The reaction products (p and ^{3}He) ionise the gas, and they release inside the detector their energies producing an energy spectrum with a full energy peak at 764 keV.

As for the BF_3 detectors, ^{3}He tubes can be affected by the wall effect if the products range is comparable with tube dimensions. A way to reduce the wall effect is to increase the gas pressure in order to reduce the charged products range. A pressure increase has also as consequence an increase of the detection efficiency (from 25% at 1 atm for thermal neutron to 76% at 5 atm).

1.4.4 Fission counters

Detector based on fission reaction are widely used since the reaction liberates high energy (around 200 MeV) and 160 MeV is provided to its products. The high energy of the fragments is released inside the detector producing high pulses, thus it is very easy discriminate pulses from the background.

The most common detectors based on fission reactions are the fission chambers, where the fissile material is deposited on the inner surface. The pulse high spectrum depends on fissile surface thickness and also on the geometric system where the fragments are collected. If the fissile deposit is comparable with the fragment ranges, the spectrum shows a double peak. If the deposit is thicker than the ranges, the fragments release their energies in the deposit and the spectrum presents a distortion. The detection efficiency is related to the deposit, some fission chambers have more deposit than one in order to increase the detection efficiency.

The fission fragments are emitted back to back, thus if both fragments can be detected, it is possible to perform coincident measurements and discriminate the fragments from other particles, such as alphas.

Chapter 2

Gas detectors

Since this work is focused on the construction and characterisation of a gaseous detector based on the GEM technology, this chapter will briefly introduce the operation principles of these devices. The idea behind it is to observe the effects due to the passage of a charged particle into a gas. The particle ionizes the gas along its path and, as a result, an *ion pair* (positive ion and free electron) is created, which produces a detectable electronic signal.

2.1 Operational regimes

Gas detectors are operated in different voltage regimes (ΔV), so three main modes of operation are possible: ionization, proportional and Geiger-Mueller mode (fig.2.1). Working in these regimes, three detector categories may be described: ionization chambers, proportional counters and Geiger-Mueller detectors.

2.1.1 Ionization mode

Free electrons and ions created in a gas move with random thermal motion and generate a diffusion process away from regions of high density. Diffusion is grater for electrons than for ions due to their lower mass and the electron "cloud" will spread from the origin point with Gaussian spatial distribution. The standard deviation of this distribution is defined as $\sigma = \sqrt{2\mathrm{Dt}}$, where the diffusion coefficient D comes from the kinetic gas theory and t is the elapsed time . During these collisions, electrons, ions and neutral gas molecules can have different behaviors:

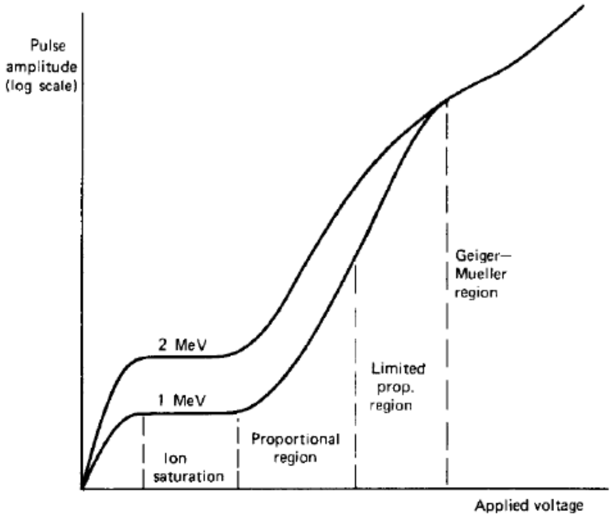

Figure 2.1: The picture shows the operation regions of gaseous detector. The increase of the applied voltage determines an increase of the pulse amplitude. There is a transition region between proportional region and Geiger-Mueller region called *Limited proportional region*, inside which some non-linearity is observed. [2]

- Charge transfer collisions: a positive ion hits a neutral gas molecule and an electron is transferred to the ion reversing the two initial states.
- Electron attachment: a free electron is captured by a neutral molecule which becomes a negative ion.
- Recombination: an electron and an ion recombine giving a neutral molecule.

If an external electric field is applied in the region containing the ionized gas, the electrostatic force guides charges away from the point of origin. The charge particle motion is given by the thermal motion and the drift motion and the drift velocity $\mathrm{v_D}$, which is positive for ions and negative for electrons, is defined as:

$$\mathrm{v_D} = \frac{\mu \mathrm{E}}{\mathrm{P}} \tag{2.1}$$

where E is the electric field, P the gas pressure and μ is the mobility of the particle. Considering a gas with medium atomic number at P=1 atm, E=10^4 V/m, ions have $\mathrm{v_D}$ of about 1 m/s (they travel for 1 cm inside the detector in 10 ms). In the same condition free electrons cover the same space in a few μs thanks to their mass 2000 times lower than any possible ion mass.

The most common gas detector is the ionization chamber, in which the gas is encapsulated between anode and cathode. Applying a small ΔV ($< 10^6$ V/m)between anode and cathode, free electrons move towards the anode and ions to the cathode, where they are collected. This motion produces a detectable signal, the amplitude of which is proportional to the released energy of the particle. The applied ΔV is not enough to produce an electron multiplication (this behavior is specific in the proportional mode described in the following subsection), thus only high ionizing particles, such as α and heavy ions, can produce a signal distinguishable from the noise.

2.1.2 Proportional mode

Increasing the applied ΔV over a given threshold (typically the applied field is 10^6 V/m for every gas at atmospheric pressure), the proportional mode is reached. Electrons from gas ionization are accelerated and, as they collide against other electrons, a second ionization happens. This multiplication process is known as *Townsend avalanche* and it is described by Townsend equation:

$$d\mathrm{n} = \alpha \mathrm{n}\, d\mathrm{n}$$

which describes the increase of the number of the electrons per unit path length and where α is called the *Townsend coefficient* for the gas.

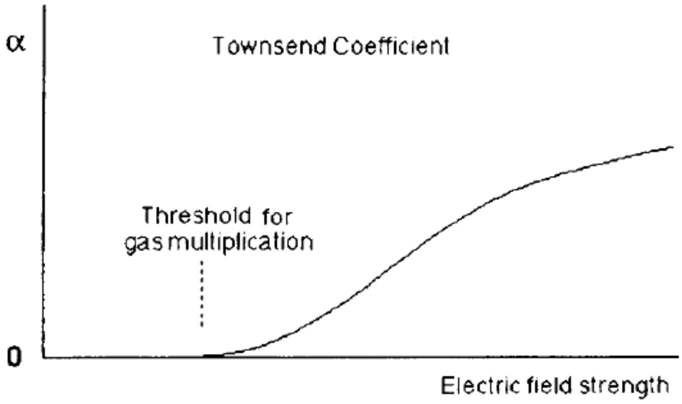

Figure 2.2: Townsend coefficient trend for a typical gas.[2]

The value of α is zero below the threshold (as shown in fig.2.2) and above the threshold increases with the electric field. For a uniform field, α is constant and the previous equation becomes:

$$\mathrm{n(x)} = \mathrm{n(0)} e^{\alpha \mathrm{x}}$$

so, the number of produced electrons increases exponentially with the distance during the multiplication and this is due to a disuniformity of the field along the electron path. The electron multiplication has as a consequence the amplification of the charge in this regime and the number of the final multiplied charges it still proportional to the initial number of the ion pairs produced by the interacting particle, and eventually to the particle energy. Thanks to this principle of operation, proportional counters (the detectors which work in proportional mode) can be used to detect radiation, such as X-rays, for which the number of produced primary electron-ion pairs is too small to produce a detectable signal. An example of this device is the multi-wire proportional counter, which is made of two large plates (the cathodes) and in their middle a series of wires (the anode) are positioned with a distance of 1 or 2 mm. An uniform electric field is created along the electrodes. Once the electron-ion pairs are formed, electrons are guided towards the wires where they are accelerated and avalanches are generated, then a signal is created on the wires. Increasing the voltage, the electrons are fast collected, but the ions are slower than electrons. Thus, ions create a cloud, which create a shape distortion of the electric field within the detector. This is the limited proportionality region, where charge is collected but with the introduction of non-linear effects.

2.1.3 Geiger-Mueller multiplication mode

Geiger-Mueller counters are the third gas detector category based on ionization. Increasing the field ($E \gg 10^6$ V/m), the charge created by the positive ions is dominant; ions recombine with electrons with a consequent UV emission and an avalanche can trigger a second avalanche in a different position. This process is known as *Geiger discharge* and leads to an exponential growth of the number of avalanches for a single detected particle. All output pulses have on average the same amplitude and the information of the energy of the initial radiation is lost.

2.2 Micropattern Gas Detectors (MPGD)

From 1990s, new technologies have been developed in the gaseous detector field, which involve photolitography and etching techniques. Their configuration or readout allow to reach a spatial resolution in the order micrometers and to work at high rates. The main commons are: Microstrip Gas Chamber, Micromegas, Resistive Plate Chamber and Gas Electron Multiplier (GEM).

2.2.1 Microstrip Gas Chamber

Microstrip Gas Chambers (MSGC) were invented in 1988 by Oed [5]. They are made of a drift plane and a strip anode, whose electrodes are created with etching technique. The strips are realised with the photolitography technique [6], which allows a tight pitch and, as consequence, a better spatial resolution than multiwire proportional counters. The detectors work in a constant gas flow in order to avoid gas instabilities and the inner components are made of low-outgassing materials, in order to not contaminate the gas. The electric field is applied between the drift plane and the anode, then the electrons are moved towards the anode, where the avalanches are generated. The motion of the positive ions liberated during the avalanches generate the observed signal. The ions must travel a short distance to reach the cathode, then they are rapidly collected allowing the detector to operate at high rates. They are constantly fluxed with different kind of gases, such as noble gases, in order to work always with a clean gas reducing discharges and instability effects during time.

2.2.2 Micromegas

In 1996 a new gas detector has been developed and nowadays, it is widely used in different kind of experiments, such as COMPASS (hadronic physics) [7] and T2K (neutrino physics) [8]. The Micro-Mesh gaseous detectors (Micromegas) [9] are two parallel planes (cathode and anode) divided by a micro-hole mesh and the entire system is filled with gas. The incident radiation ionises the gas in the detector first part (between cathode and mesh). The presence of the electric field guides the primary electron towards the mesh, where they pass through while the positive ions are collected by the mesh. Thanks to a high electric field between the mesh and anode the electrons are multiplied and then collected. The first region is few millimeters in order to fully absorb the incident radiation, while the second region is around 0.1 mm in order to collect the electrons and create a very fast signal (in the order of nanoseconds).

2.2.3 Resistive Plate Chamber

The Resistive Plate Chamber (RPC) is a detector similar to the parallel plate avalanche counter (two parallel electrodes divided by a small gap), where the electrodes are made of bakelite, plastic or glass. These materials have high electrical resistivity ($10^9 - 10^{10}\Omega$/cm), which limits the discharges. The two planes are placed at few millimeters apart and the system is filled with gas. With this configuration, the electrons are collected very fast, thus the detector has a good time resolution (few ns depending on different gas mixtures [10]). The electrodes are assembled with a strip pattern in order to obtain the spatial resolution.

2.3 Gas Electron Multiplier

Inside MPGD category, Gas Electron Multiplier (GEM) detectors are nowadays largely used in various physics sectors, such as fundamental particle physics [11], medical physics [12] and plasma physics [13]. Developed in 1997 by F.Sauli [14] at CERN, the peculiarity of GEM detectors is the presence inside these devices of GEM foils.

The GEM foil is made of an insulating foil of 50 μm thickness, typically made of kapton, sandwiched between two conductive layers (usually copper) each of 5 μm thickness. The GEM foil is perforated using a photo lithographic technique creating a high density (50-100 mm^{-2}) of bi-conical holes (figure 2.3.b): the outer diameter is of 70 μm and the inner is 50 μm. The holes are placed in a hexagonal shape with 140 μm pitch (figure 2.3.a). The double-conical shape is fundamental to reach high gains (around 10^4), even if it brings the charging up effect (an electron accumulation around the rim, which is the retreat of the copper from the hole). If the detector application needed stronger GEM foils, it is possible to use the *thick* GEM foils, which are characterised by cylindrical holes and make the detector behavior more stable than standard GEM foils, but they cannot reach high gains.

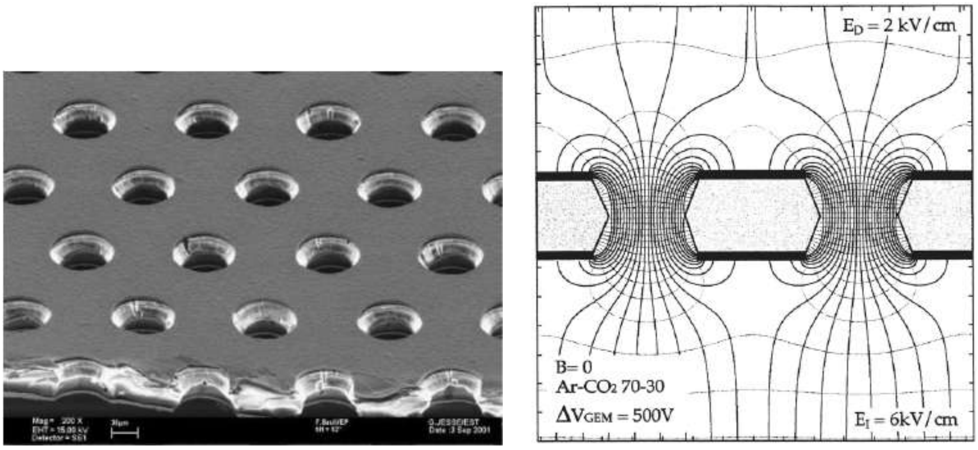

(a) **(b)**

Figure 2.3: (a) Microscopic view of GEM foil. [15] (b)Section of a GEM foil whit drawn electric field lines. [15]

This foil can be cut and bent in different shapes (square, cylindrical, etc. [15]) making it adaptable to different physical situations. Moreover, it has been seen that the correct GEM detector operation is possible until an area of 100 cm^2 [14]. In order to maintain optimal detector behavior with large areas, it is possible to "sectorise" the electrodes [16] with the further advantage to possibly disable a sector if there is damage without losing the entire foil.


(a) (b)

Figure 2.4: (a) Standard GEM foil. (b) Sectorised GEM foil [17].

The complete device is composed of a cathode, one or more GEM foils and an anode; the entire system is constantly fluxed at 5 l/h with a gas mixture of $ArCO_2$ (70%-30%). The choice of this gas mixture is due to its components properties: Ar is a noble gas, not inflammable and cheap (if compared with other gases, such as the ^3He [18]); the CO_2 is a quencher and it absorbs the photon emission due to the de-excitation of the Ar atoms.

The region between the cathode and the top of the GEM foil is called *drift gap* (figure 2.5), inside which the primary ionization occurs. Applying a ΔV to the electrodes of this region, the electrons are guided along the electric field lines inside the GEM foil holes (see fig.2.3.b).

Between the two copper layers of a GEM foil a ΔV from 200 V and 500 V is applied, creating a strong electric field. Once the electrons arrive inside the hole, they are accelerated and collide against other electrons of the gas, ionizing it. Multiplied electrons move inside the region between the second layer (the bottom) of the GEM foil and the anode, called *induction gap* (E_i), and are eventually collected by the anode. Meantime, ions move along electric field lines towards the cathode; if they pass near the foils, they don't enter inside the holes, but they are collected on the copper layer and neutralised. The output signal is thus given only by the electrons, which are faster than ions and provide a signal of few nanoseconds.

The signal depends on several factors, in particular: the applied fields, the number of the GEM foils and the distance between them (gap) and the gas mixture choice. Thus GEM detectors can sustain high rates (up to MHz/mm^2) compared to ^{3}He tubes which have the signal completely dominated by ions (maximum rate kHz/mm^2) [2].

Defining the *gain* of a GEM detector as the ratio between the number of the electrons produced into the holes and the numbers of the electrons entering into the holes, it is possible to improve this feature by optimising the electric field between the regions. Typically, the electric field of the drift gap (E_d) and transfer (T) are in the order of 1.5 kV/cm; in fact with low E_d and T values, primary charges can be lost by recombination while with high values, the electric field lines can end on the top surface of the GEM foil causing a loss of the electrons. With an E_d and T of 1.5 kV/cm a counting rate plateau region is reached, which means that all charges are collected in the GEM holes.

The electric field of the E_i determines the shape and size of the signal. In general the applied field E_i is about 5 kV/cm: if E_i is lower than this value, charge is lost on the bottom of GEM foil and if E_i is higher (for example 8 kV/cm in $ArCO_2$) the gain increases very fast and discharges can occur inside the induction region.

The other main GEM parameters [19] are:

- *Electron collection efficiency:* ratio between the number of electrons entering into the holes and the primary electrons.
- *Electron extraction efficiency:* ratio between the number of electrons, which are extracted from the holes and reach the anode, and the number of electrons produced by the multiplication.
- *Ion extraction efficiency:* ratio between the number of the ions coming from the holes and reaching the cathode and the number of the ions produced inside the holes after the electron multiplication.

The gain is strictly connected with the applied HV, but an intense HV (more than 500 V) applied to a single layer can cause discharges inside the detector. A safer method to increase the gain, reaching a value of 10^4, is to stack GEM foils in series and create a GEM foil cascade. Generally the connected foils are three, creating a *Triple GEM* detector. [18]

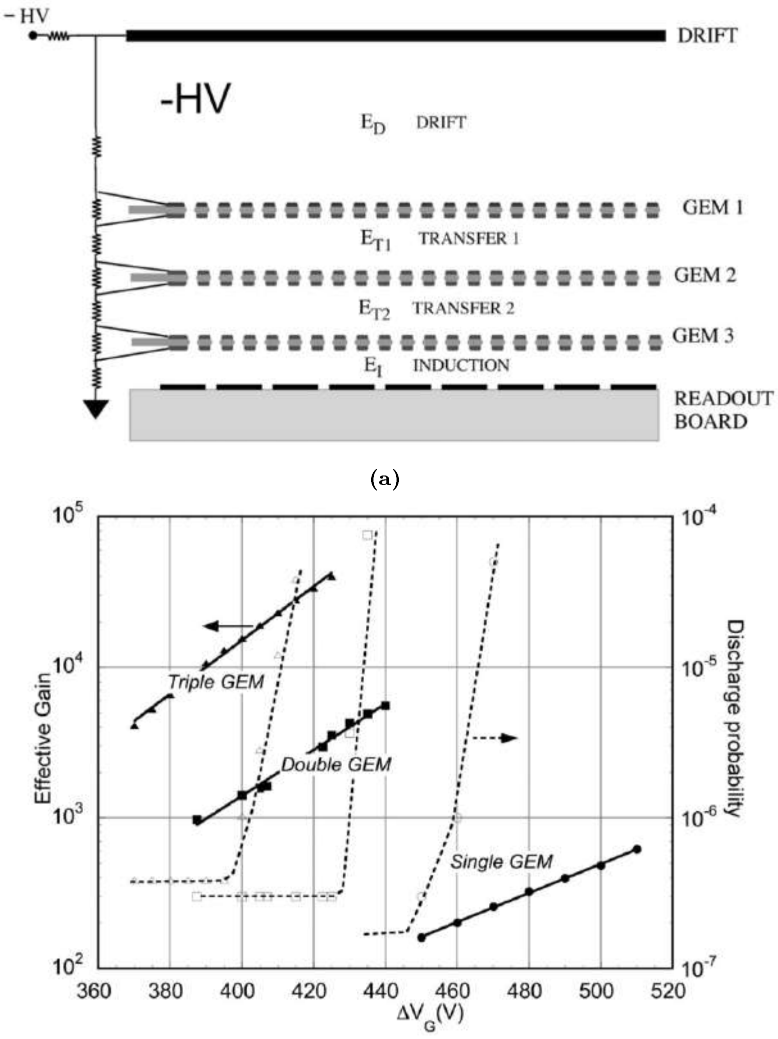

(a)

(b)

Figure 2.5: a) Schematic image of a triple GEM. [15] b) Gain trend of a different GEM detectors. It is possible reach high gain with low applied voltage using triple GEM detectors.[15]

This device is characterised by two *transfer regions* T_1 and T_2 with electric fields E_{T_1} and E_{T_2} of reduced intensity (typically 1 kV/cm) than E_D in order to guide the electrons into the holes.

Thanks to their principle of operation and their features, gaseous detectors based on GEM technology are useful in various physic fields. In fact, the work described in the next chapters will show GEM detectors optimised for neutron detection for condensed matter physics experiments.

Chapter 3

Simulations with Geant4

Numerical simulations aimed to determine the main parameters are needed to develop the device. Simulating the radiation interaction with matter, it is possible to provide the detector response.

The main work of this PhD thesis is related to an innovative thermal neutron detector. As mention in chapter 1, neutrons can be detected only if they are converted into charged particles with a proper neutron converter.

Thus, the novelty of this project lays in the combination of the GEM detector, described in chapter 2, with boron layers deposited on both sides of the GEM foils. Since the detector detection efficiency is strictly connected to the boron presence inside the detector, increasing the boron layers, the detection efficiency increases.

The simulations reported in this chapter have been performed with the open source Geant4 toolkit [20]. The boron-GEM (BGEM) foils structure has been created and then, several BGEM foils have been stacked. Then, thermal neutrons have been generated and the boron thickness and the gas gap thickness have been studied to determine the optimum detector configuration, which minimize the number of the boron layer and maximize the detection efficiency.

3.1 Geant4

Geant4 is an open source toolkit based on C++ code language, created custom at CERN [21] to simulate the radiation-matter interaction. Since it is based on object oriented programming code, the program is based on a *main* file and three mandatory classes: *DetectorConstruction*, *PhysicsList*, *PrimaryGeneratorAction*.

- *DetectorConstruction*: allows to define the materials and the detector geometry. The system is placed inside a mother volume, which is the world where the system is defined.
- *PhysicsList*: it is mandatory to define the particles and their interactions, i.e. electromagnetic or nuclear interaction.
- *PrimaryGeneratorAction*: it is mandatory to generate particles and their features, such as the energy and the position.

3.2 Detector simulations

The simulation main file contains the main instruction of the simulation:

- With the class *G4MTRunManager*, the instruction are given to begin and to manage the runs in Multi-thread mode.
- The chosen physics list, optimised for thermal neutrons and provided by the class *G4VUserPhysicsList*, is *QGSP_BERT_HP()*. QGSP_BERT_HP() contains the neutron cross sections for the main materials and it is very accurate for neutrons with energy below 20 MeV.
- The *PrimaryGeneratorAction* is implemented via the *General Particle Source* class (GPS) and all instruction are contained into a macro. The neutron energy has been set at 25 meV and the a two dimensional beam has been positioned at -1 m from the axis center. The beam direction is perpendicular to the detector and 10^6 neutrons have been generated for each simulation.
- The graphical visualisation is activated with the class G4UImanager and allows to reproduce the geometry and the radiation interaction.

The detector geometry has been build stacking several slabs, which reproduce the GEM foils of 10×10 cm^2 without holes. The scheme is reported in figures 3.1a and 3.1b, and it is the sequence of the following layers: boron, copper, kapton, copper and boron. Then, before and after each BGEM foils, the $ArCO_2$ 70%-30% gas mixture has been placed. The holes have been taken into consideration normalising the simulation results with the optical transparency coefficient, defined as the ratio between the total area and the total area occupied by the holes. It results to be 0.78.

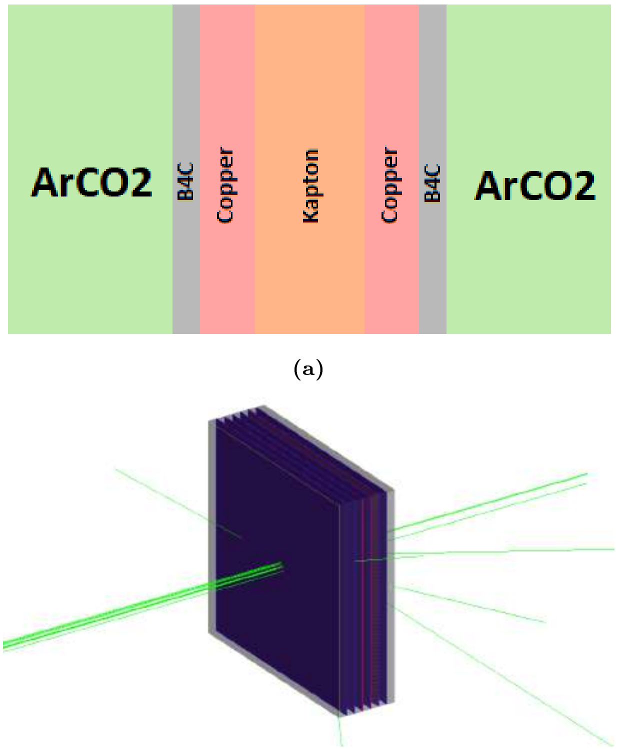

(a)

(b)

Figure 3.1: (a): MBGEM detector scheme implemented for the simulation with GEANT4 toolkit. (b) Detector geometry and neutron beam interaction.

The parameters studied during the simulations are:

- Gap thickness
- Boron thickness
- Number of MBGEM foils
- Detector efficiency
- Gamma-detector interaction

The gas mixture $ArCO_2$ has been implemented, and the energy released from the alpha and lithium inside the gas gap (BGAP) have been studied. The deposited energies have been considered only if they release an energy over 200 keV; the threshold is necessary to not consider the gamma-rays from the background.

The graphs in figure 3.2 shows the total counts trend normalised for number of the incident neutrons at the increase of the first BGAP value. Increasing the threshold from

150 keV up to 300 keV, the total counts decrease until 1 mm. These graphs shows that a threshold of 150 keV is sufficient to consider neutrons without event losses. In fact, setting a threshold over 150 keV, the events in the BGAP ranges below 1 mm are lost. The same graphs have been obtained also for the deposited energy for the lithium particles, and they show the same trend of the graphs reported in figure 3.2. Since the simulations cannot reproduce all the events that can affect a measurement during an experiment, the threshold has been set at 200 keV.

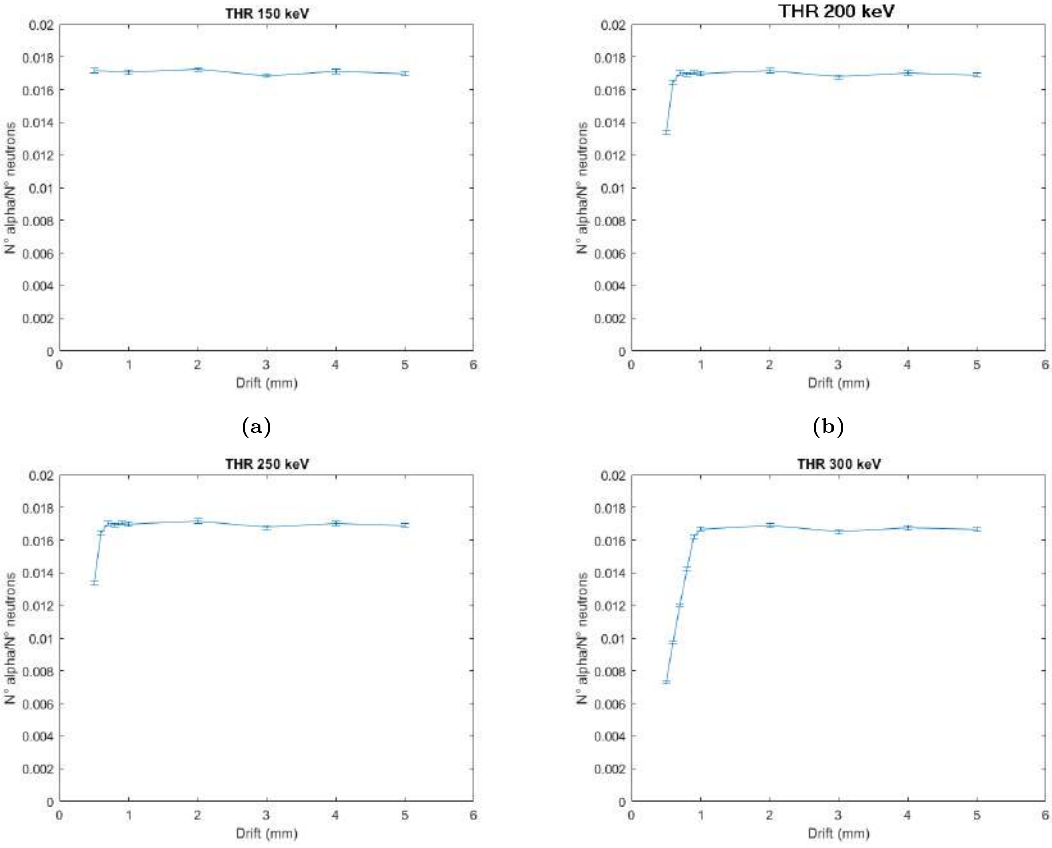

(a) (b)

(c) (d)

Figure 3.2: Total number of the α particles normalised for the incident neutrons at different BGAPs values with different thresholds.

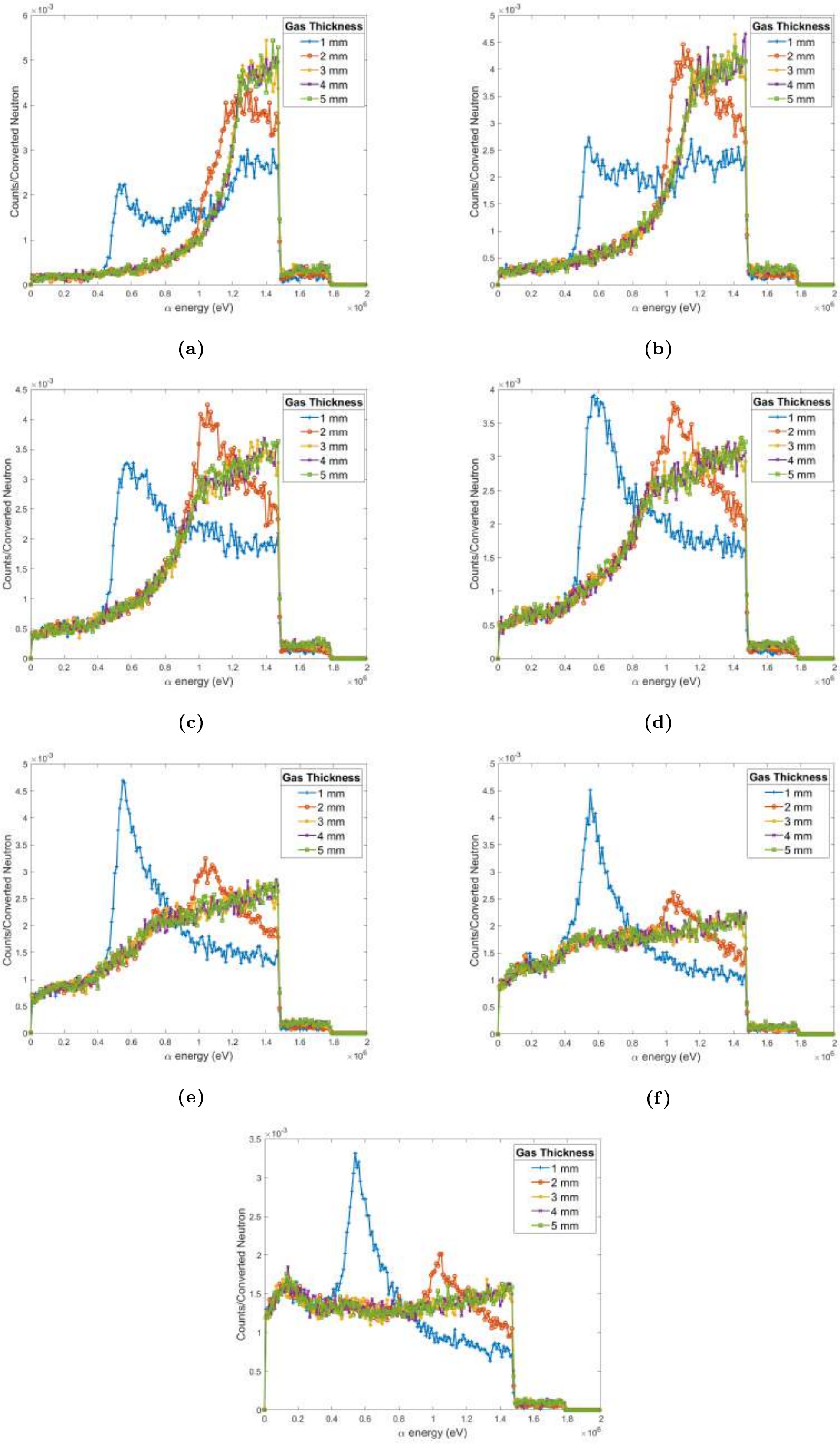

(a)

(b)

(c)

(d)

(e)

(f)

(g)

Figure 3.3: Energy deposition of alpha particles inside different thickness (from 1 to 5 mm) of $ArCO_2$ gas mixture with the two boron layers 0.5 μm(a), 0.7 μm(b), 1 μm(c) and 1.2 μm(d) thick.

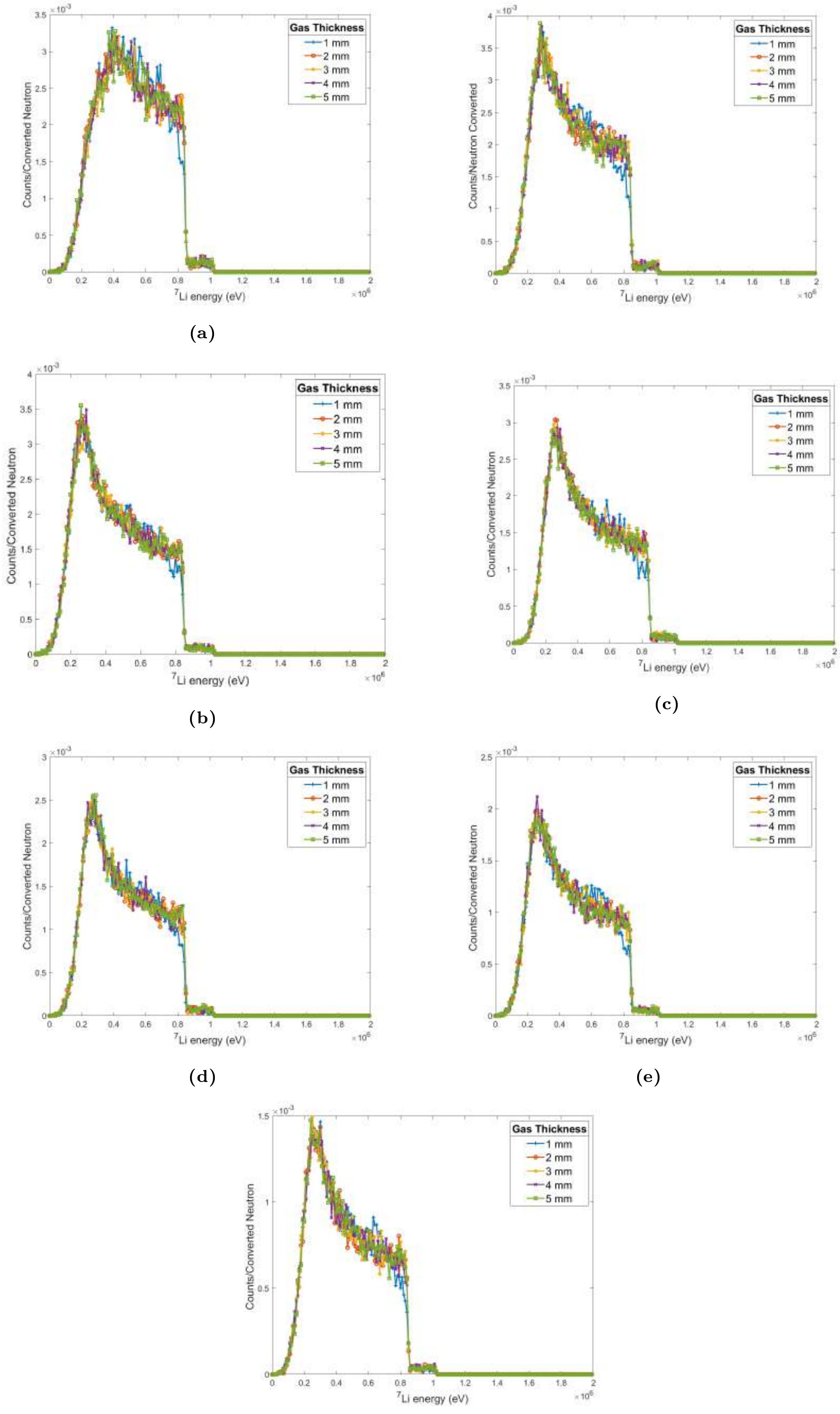

(a)

(b)

(c)

(d)

(e)

(f)

Figure 3.4: Energy deposition of lithium particles inside different thickness (from 1 to 5 mm) of $ArCO_2$ gas mixture with the two boron layers 0.5 μm(a), 0.7 μm(b), 1 μm(c) and 1.2 μm(d) thick.

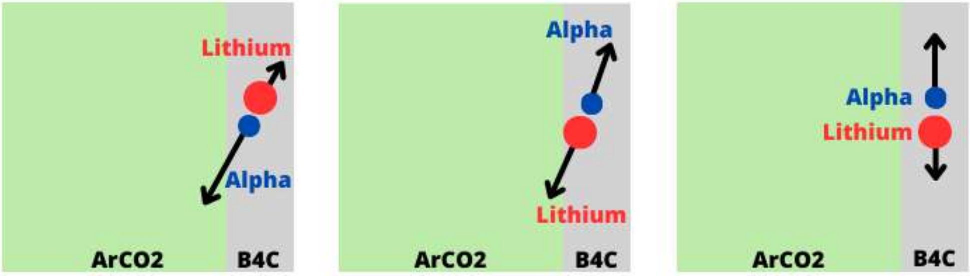

Figure 3.5: Scheme of the alpha and lithium emission and their escape from the boron layer.

Figures 3.3 and 3.4 show the energy deposited by alphas and lithiums in $ArCO_2$ with different gaps and different boron layers thickness. The reported graphs refer to the deposited energy in the first gap (BGAP1), for the other BGAPs, the obtained graphs have the same shape for all configurations, thus they are not reported. Increasing the BGAP thickness, the particles can deposit more energy inside the gas. This energy amount ionises the gas, thus alpha and lithium release enough energy with a BGAP from 2 mm for all the considered B_4C layer thicknesses. With these energies, electron-ion pairs con be formed. Thus, the BGAP has been fixed at 2 mm to have enough energy from α and Li to ionise the gas and to keep the detector with a compact design.

Another important parameter is the boron thickness. The charged products, from the neutron reaction with boron, are emitted back to back (see Chapter 1), thus only one particle or neither of the two are detected (see figure 3.5). In fact, the alpha or the lithium escape depends on the angle emission and the particles, which travel opposite to gas, are absorbed from the boron layer. Moreover, if the escape particle is emitted in the internal part of the layer, it loses a part of their energy inside the boron.

Thus, if the boron layers are chosen too thin, the neutron conversion efficiency decreases due to less interaction of the neutrons with the boron layers. On the other hand, if the boron is too thick, alpha and lithium are absorbed. For both cases, the events are lost resulting in a decrease of the detection efficiency.

Figure 3.6 shows the events in function of the energy deposition for alpha and lithium with BGAPs of 2 mm for different boron thickness normalised to the absorbed neutrons from the BGEM foil. It is visible that the counts decrease with the increase of the boron layer thickness due to increase of the α and Li particles that cannot escape from the boron layer. Moreover, these histograms consider only the counts for one BGEM foil. Inserting more than one BGEM foil, the number of the absorbed neutrons increase and

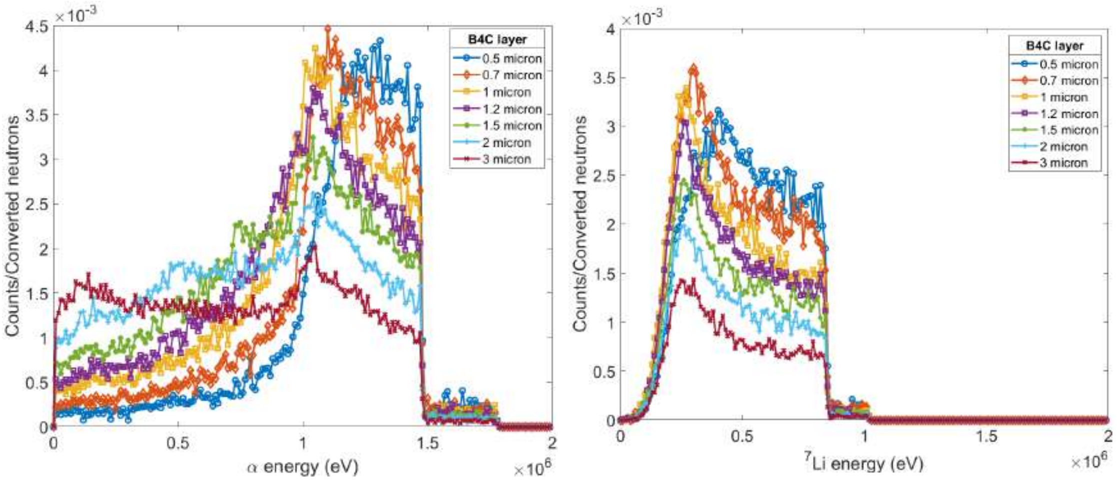

(a) (b)

Figure 3.6: Energy deposition of alpha (a) and lithium (b) particles inside 2 mm of $ArCO_2$ after the neutron conversion with different boron thickness.

fewer neutrons are available for the next foils. This effect is shown in figure 3.7a, where the plots of the total events have been normalised for the incident neutrons at different boron thicknesses (0.7, 1, 1.2, 1.5 and 2 μm) have been reported with respect to the number of the BGEM foils.

The trend highlights that the detection efficiency increases until the tenth BGEM foil, then the detection efficiency reaches a plateau region, which indicates that the incident neutrons are mostly converted.

The detection efficiency depends on also from the neutron energy, and simulations with different neutron energies (5 meV, 25 meV and 50 meV) have been performed. The results are reported inside figure 3.7 and, as expected, it follows the trend of the boron neutron cross section shown in figure 1.2 (chapter 1). In fact the efficiency decrease with the increase of the neutron energy.

Fixing the BGAPS at 2 mm and the B_4C at 1μm thick, simulations of the gamma-ray interaction have been performed; in particular gammas of 478 keV and 1 MeV have been generated. The 478 keV gammas come from the de-excitation of ^{7}Li and 1 Mev is the deposited gamma-rays energy chosen to represent the gamma-rays from the background. From this simulation, it has been evaluated the energy deposition inside the detector, considering all gaps. The energy depositions for 478 keV and 1 MeV is shown in figure 3.8. For both energies, there is a peak around 1 keV, which is lower than the alpha and lithium deposited energies (more than 0.5 MeV). Then, using this detector configurations,

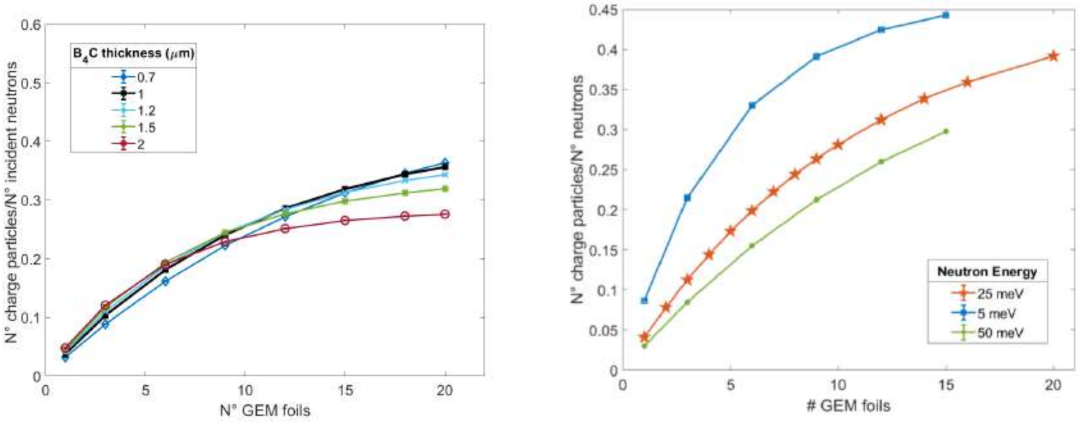

(a) **(b)**

Figure 3.7: (a) Efficiencies for different boron layer thicknesses with respect to the number of the BGEM foils. (b)Efficiencies at the increase of the number of the BGEM foils at 5 meV, 25 meV and 50 meV.

the gammas can not affect the measurements, since they have less energies than alpha and lithium.

Thus, the detector configuration is given by:

- a BAGPs of 2 mm.
- a $^{10}B_4C$ thickness of 1 μm.

3.3 CAD models

The detector has been designed with CATIA CAD software [22]. The detector has been composed of a fiberglass box, where inside at least 6 BGEM foils can be inserted, and a kapton window. The electronic readout (GEMINI, chapter 5) has been positioned on the top of the detector, in order to be out of the neutron beam.

3.4 Conclusions

The simulation results reported in this chapter highlight the configuration to build up the MBGEM detector. The energy deposition of α and lithium particles indicates that a gap of 2 mm is necessary to have energy to ionise the gas. The boron thickness simulation suggests that 1 μm layer is a good choice to have a good conversion efficiency.

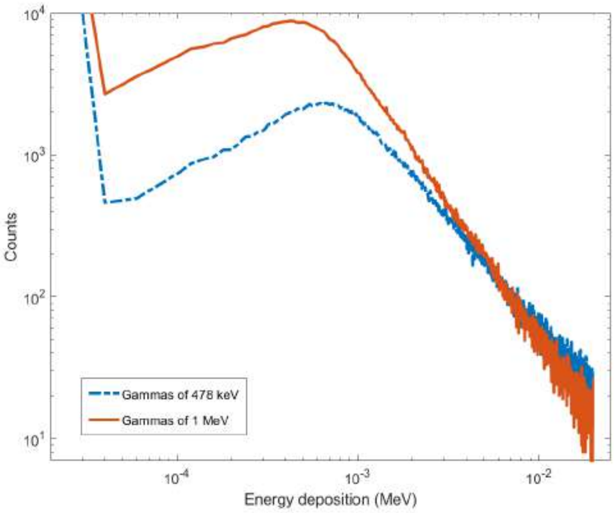

Figure 3.8: 478 keV and 1 MeV gamma energy deposition.

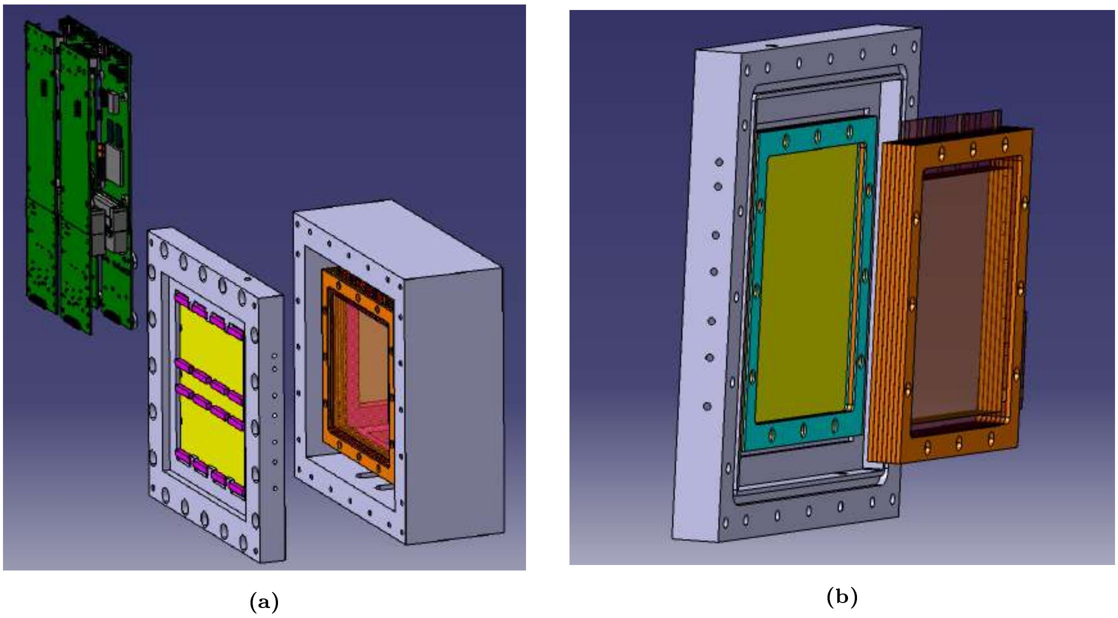

(a) (b)

Figure 3.9: Pictures of the MBGEM CAD model. (a) Detector main components: box with GEM foils, anode and electronic readout. (b) GEM foils and electronic readout zoom.

To maximise the detection efficiency, the boron thickness has been chosen 1 μm and the BGAPs 2 mm thick, in order to have a compact detector. Combining these two parameters, the boron and the gas thicknesses, with the number of BGEM foils, the simulations indicates that the MBGEM detector can be build up with maximum 10 BGEM foils. A higher value brings a plateau suggesting that the detection efficiency can not be increased.

Chapter 4

The 6 Multi-layer Boron-GEM detector

The PhD project reported in this thesis is related to the development and the characterisation of a GEM detector optimised for thermal neutrons. In this chapter, it will be shown the work related of a triple GEM detector coupled with 6 boron-coated GEM foils; the entire system is named 6MBGEM detector.

As mentioned in the previous chapters, neutrons can be detected only via nuclear reactions, thus a suitable converter is needed to convert neutrons into charged particles. From literature, the most efficient neutron converter is the ^{3}He (see chapter 1), but during the last 15 years, the ^{3}He shortage [23] has brought the necessity to develop new neutron detectors.

Since GEM detectors have several good properties, as described in the chapter 2, they can be used to detect neutrons and one of the main method used is to equip the detector with components covered with boron carbide ($^{10}B_4C$). One of first GEM detector for neutron detection was build up with three standard GEM foils, an anode and a 1μm boron-coated cathode [24]. The boron deposition has been performed using natural B_4C, and it has been deposited on an aluminum substrate.

Then several upgrades have been done, in particular coupling GEM detectors with other components covered with boron, such as the lamellas. An example of this device is the I-BANDGEM detector [25] and with this technology, the detection efficiency reached a value around 30% at 25 meV.

In 2011, the CASCADE group from Heidelberg University [26] was able to produce for the first time GEM foils covered with a boron layer. The detector was build up with six boron-GEM foils and the anode was placed in the middle of this boron stack, dividing the device in two parts. With this configuration, the detection efficiency reached at 1.8 Åis around 8%.

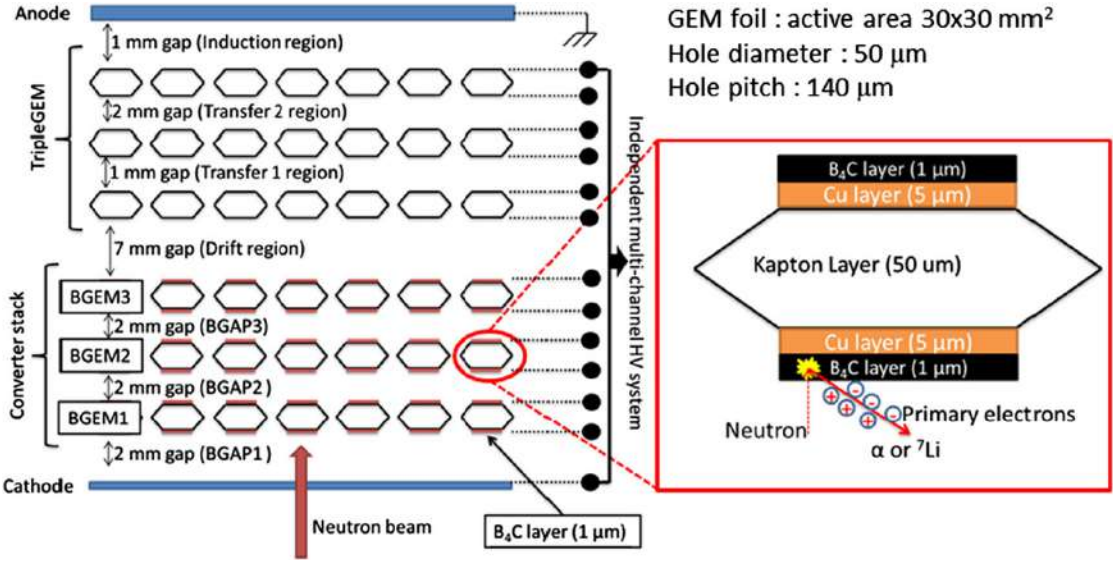

Figure 4.1: The MBGEM detector scheme with three BGEM foils.

From this idea, the neutron group of the Università degli Studi Milano-Bicocca and Istituto per la Scienza e la Tecnologia dei Plasmi (ISTP), in collaboration with CERN and with the ESS Linköping Detector Coatings Workshop (Linköping, Sweden), started the study of the process to deposit the boron on the GEM foils until they were able to realise the BGEM foils (figure 4.2a). The new detector technology, the MBGEM [27] is composed of a conversion region, made of the BGEM foils, and a multiplication region, made of three standard GEM foils (TGEM) (figure 4.1). All foils, with an area of 3×3 cm^2 (figure 4.2a), have been placed between a cathode and a pixelated anode; the used electronic readout was the TIMEPix [28]. The detector (MBGEMPix) has been tested at the TRIGA MARK II reactor located in Pavia at the Laboratorio di Energia Nucleare Applicata (L.E.N.A.) with a thermal neutron beam. Through this characterisation, it has been demonstrated that the count rate scales linearly with the number of active layers (figure 4.2b).

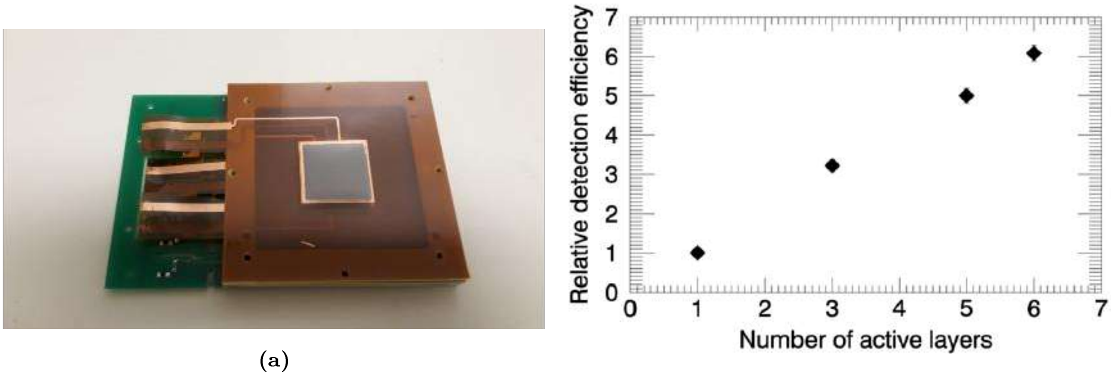

(a)

(b)

Figure 4.2: (a) BGEM foils 3×3 cm^2 picture. (b) Linear response of the MBGEMPix detector with the increase of the active boron layers. [27]

Starting from these results, a new detector with an active area of 10×10 cm^2 and equipped with the new GEMINI electronic readout (widely described in the next chapter), has been realised.

4.1 The $^{10}B_4C$ deposition technology

The process of the boron deposition on the GEM foils starts the raw materials of the GEM foils, which are a kapton layer sandwiched between two copper layers. The GEM raw materials have been covered with an aluminum mask necessary to treat only the internal areas (future GEM foils) and to avoid the electrical contacts damage caused by the boron during the deposition process (figure 4.3a). The foils have been heated until 100 °C and, in the meanwhile, the deposition chamber has been set with a background pressure of $\sim 1.5 \times 10^{-4}$ Pa. Then, the foils have been exposed in pure Ar atmosphere at 0.35 Pa in order to be treated with the radio frequency plasma etching technique. This treatment allows the possible oxide residues to be removed on the Cu layers, and it increases the surface roughness to have a good film adhesion [27]. The samples have been coated with a B_4C layer always in pure Ar at 0.40 Pa plus a Cu layer at 0.30 Pa. After the boron deposition, the GEM foils returned to CERN for the final etching and the photo resist dots have been removed in order to etch the polyamide covered by the boron deposition. Once the holes are created with the hexagonal pattern, the Cu cover has been removed from both layers and the entire process is concluded.

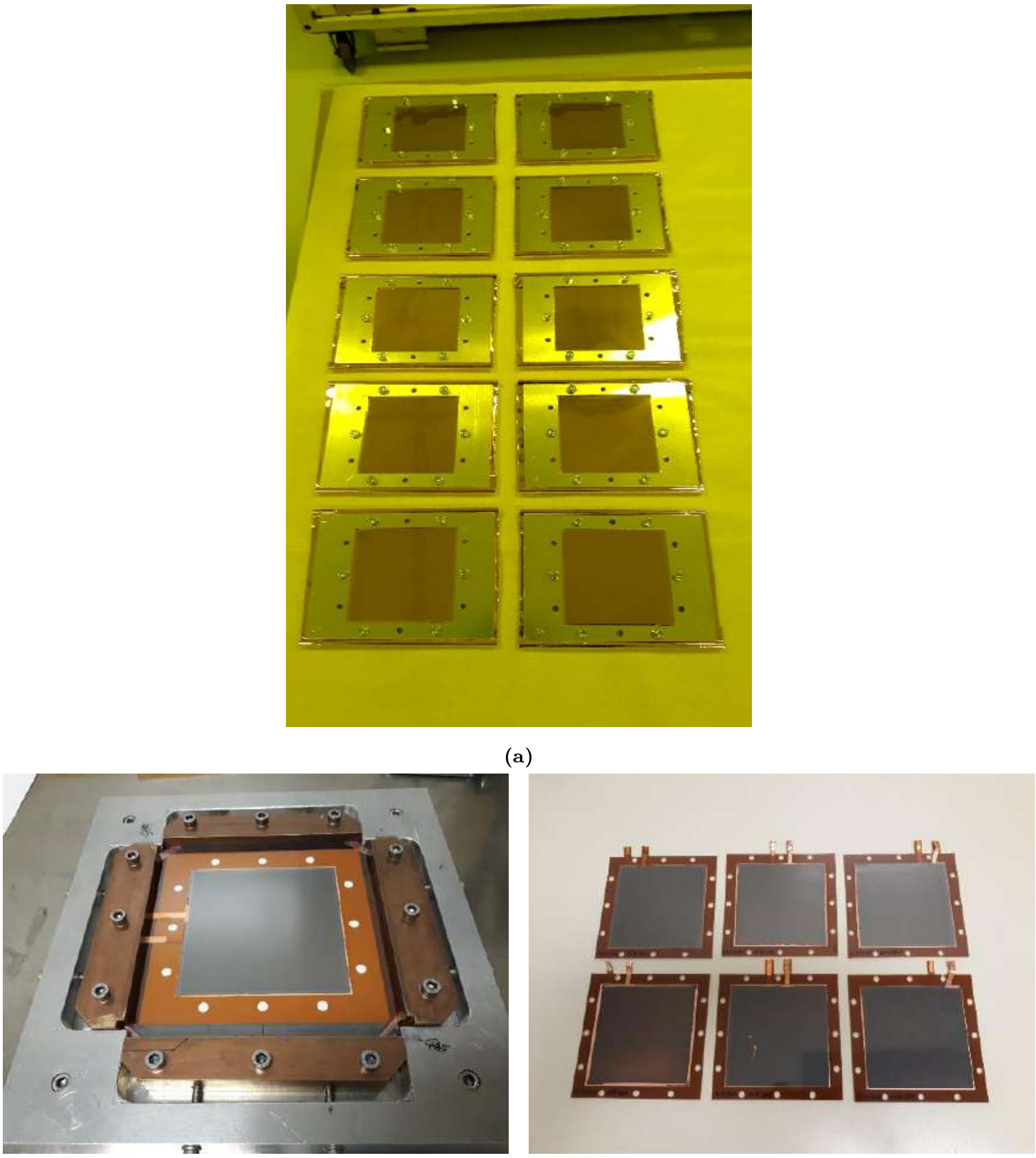

(a)

(b)

(c)

Figure 4.3: (a) Standard GEM foils with the Al masks. (b) Stretched BGEM foil before the frame application. (c) BGEM foils at the end of the stretching process.

4.2 Detector design

The detector has been build up inside the Milano-Bicocca and ISTP laboratories. Six BGEM foils have been stretched and frames 2 mm thick have been applied (figures 4.3b and 4.4a). The detector has been assembled with six BGEM foils, with gaps (BGAP) of 2mm; they have been coupled with three standard GEM foils with the gaps: Drift (D) 5 mm, Transfer 1 (T1) 1 mm, Transfer 1 (T2) 2 mm and Induction (Ind) 1 mm (figure 4.4a). The entire system has been placed in a fiberglass box with a kapton window and a PCB made of 256 pads with a dimension of 6×6 mm^2.

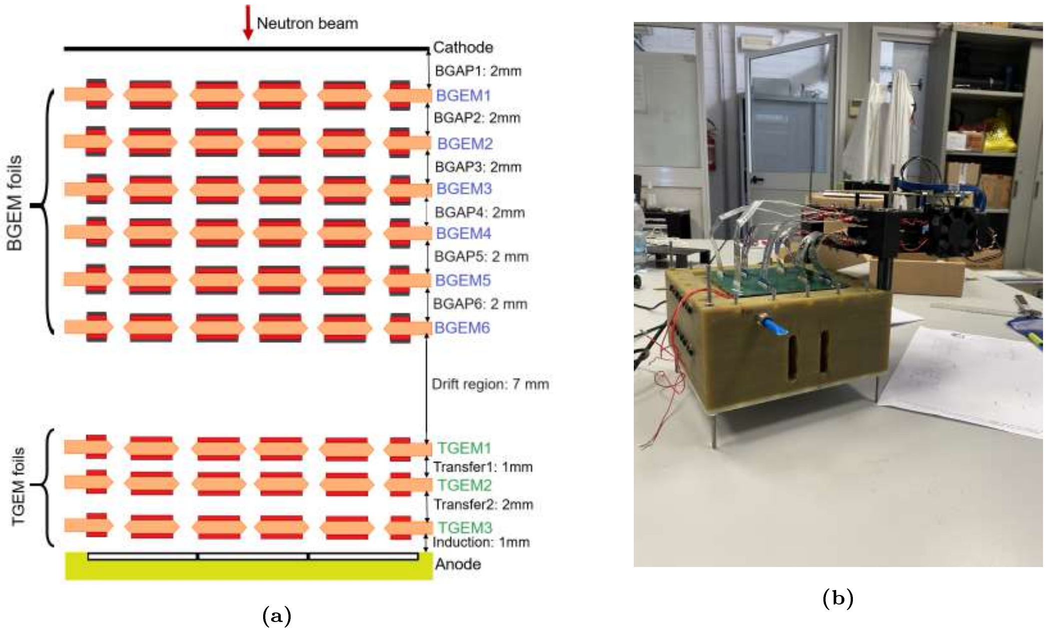

(a)

(b)

Figure 4.4: (a) 6MBGEM detector scheme. (b) Picture of the 6MBGEM detector with the GEMINI electronic readout.

The electronic readout system has been placed aside from the detector to not be exposed to the radiation and it is connected to the detector with a series of flat cables (figure 4.4b). The employed front-end electronics is based on the GEMINI ASIC (see chapter 5). Each GEMINI channel provides as output a digital signal that carries two information:: the Time over Threshold (ToT) and the Time of Arrival (ToA). The ToT is proportional to the deposited charge, thus it is useful to perform spectroscopy experiments. The ToA provides only the information about the time of the signal arrival to the detector. To operate in ToA mode, a start pulse t_0 is needed, and the detector works as a counter.

4.3 Characterisation with X-Rays

Another parameter which affects the detector response is the charge transport along the BGAPs and inside the holes. This section shows the study of the charge transport with the use of an X-Ray source.

The detector, described in the previous section 4.2, has been placed inside a shielding box and the experimental setup is composed of:

- The X-ray source: Amptek-MiniX2 X-Ray Tube [29].
- Cu and Mo Targets.
- CAEN Modules (A1526N and A1561H): HV suppliers for the BGEM stack. They are controlled by the GECO program and by a custom program made with Labview-National Instruments [30].
- HVGEM: HV module for the triple GEM.
- A Linux server: it provides the internal clock signal for the electronic readout and it allows the storage of data.
- The $ArCO_2$ gas system: the gas mixture has been fixed at 70% of Ar and 30% of CO_2 and it is constantly fluxed inside the detector at 5 l/h.

The X-ray tube accelerates electrons against a silver target emitting X-rays from Bremstrahlung; the result is a continuum spectrum with two peaks at 22 and 25 keV, which are the silver K_α and K_β lines. The X-rays impinge on a target, generating a monochromatic fluorescence X-Ray beam, due to the electron re-arrangment inside the electron shells (figure 4.5a). For this test, a Cu (figure 4.5b) and Mo target have been used, which have the emission lines at 8 keV and 17.4 keV respectively.

The detector operating principle has been checked with a series of high voltage (HV) scans. Increasing the applied HV, the primary electrons generated from one event enter inside the holes, and after the multiplication, they are guided to the next foil until the anode. The resulting spectrum shows a peak, whose counting rate increases with the increase of the applied HV. Then, from a certain HV value, all the primary electrons enter inside the holes providing the same counting rate: this condition is the counting rate plateau region, where the counting rate is stable at the variation of the HV. The aim of the HV scans is to determine the detector working point, that is the HV to apply

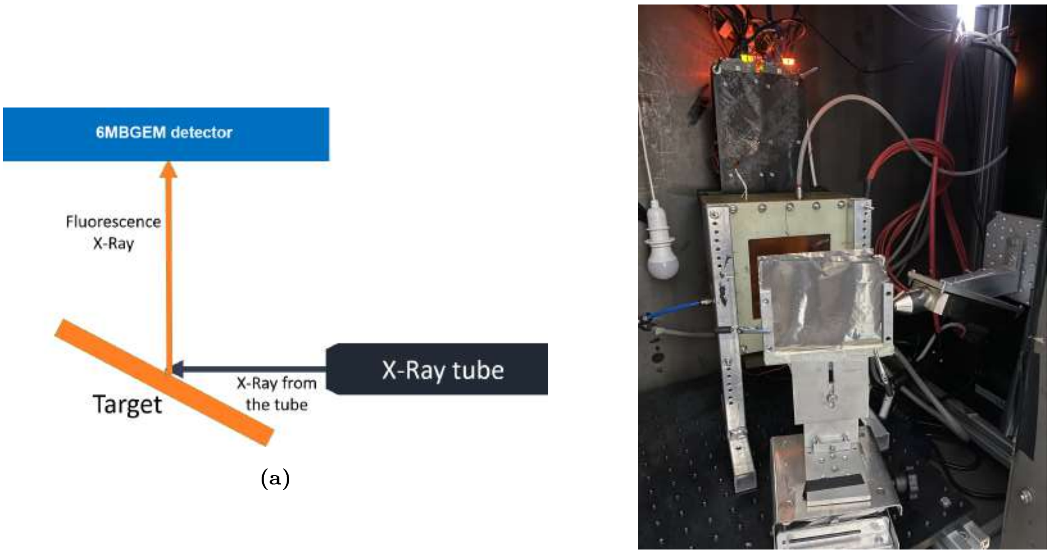

(a)

(b)

Figure 4.5: The 6MBGEM detector X-Rays setup scheme (a) and picture (b).

to have a stable counting rate during the time. Since the detector operates in a gas mixture, different factors can affect the detector stability, in particular temperature and humidity. A variation of these two parameters brings a gain variation and, consequently, a counting rate variation. Then, choosing a suitable HV in the counting rate plateau region, any variation of those parameters does not affect the detector stability.

The first scan determines the HV to set at the TGEM region. The X-ray tube parameters have been fixed with a voltage of 15 kV and a current of 150 μA. The fields of the TGEM have been set at: D=T1=T2=Ind=1 kV/cm. The graph 4.6 shows the counting rate trend at the variation of the total applied HV (the sum of HVs for each GEM foil). The counting rate increases until 1030 V, and then, from 1040 V up to 1100 V, the counting rate is constant (plateau region).

The chosen value is 1080 V (in the middle of the plateau region) and it allows the detector to work in stable conditions.

Starting from the BGEM foil close to the TGEM region, each foil has been turned on and the HV scan has been performed for all the six BGEM foils. In this case the HVs have been chosen to provide a unitary gain during the electron multiplication process. The unitary gain condition is visible in figure 4.8a, where the Cu spectra obtained from each layer are reported. All peaks are superimposed and the ratio between the peak

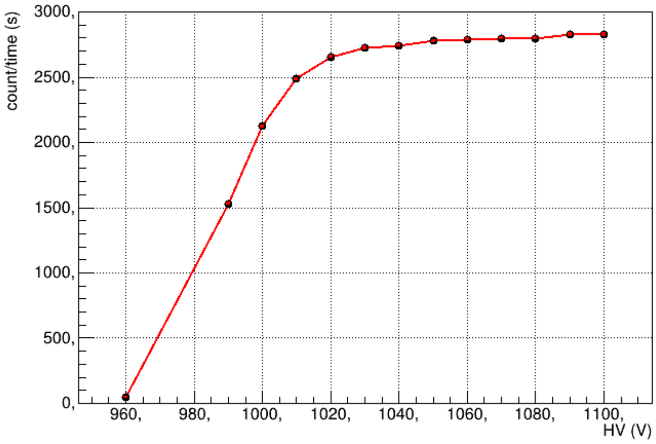

Figure 4.6: The TGEM scan. It shows the increase of the counting rate until the counting rate plateau region with the increase of the applied HV.

values with the peak value obtained in the drift region is about 1

$$\frac{\text{Peak}_{\text{BGAP}_i}}{\text{Peak}_{Drift}} \approx 1 \tag{4.1}$$

If this value is more than 1, the spectra peaks are not superimposed and the spectra are more wide than the spectra reported in figure 4.8a. Then, the HV scan will show a tight count rate plateau, thus reducing the stable condition of the working point and the detector does not have a linear response with the increase of the layers number. Moreover, a value grater the one increase the transported charges along the detector increasing the probability to have discharges through the foils. Setting the HVs to have a unitary gain, the charges are only transported from a BGEM foil to the next one and the detector response will be linear with the increase with number of the BGEM foils.

The chosen values for each scan lie in the middle of each plateau region (see figures 4.7) and they are reported inside table 4.1.

To verify that the set HVs allow only electron transport instead of multiplication, the ToT spectra at the working points for the BGEM foils have been considered. Figure 4.8a shows seven ToT spectra taken at each working point for each BGEM foil. They are well superimposed, which means that the add of a layer with that set HV allows to maintain a unitary gain.

The measurements, obtained with the HVs at the working points, have been used to verify the detector behavior at the increase of the inserted number of layers. The total counts have been normalised for the measurement time and plotted (figure 4.8b)

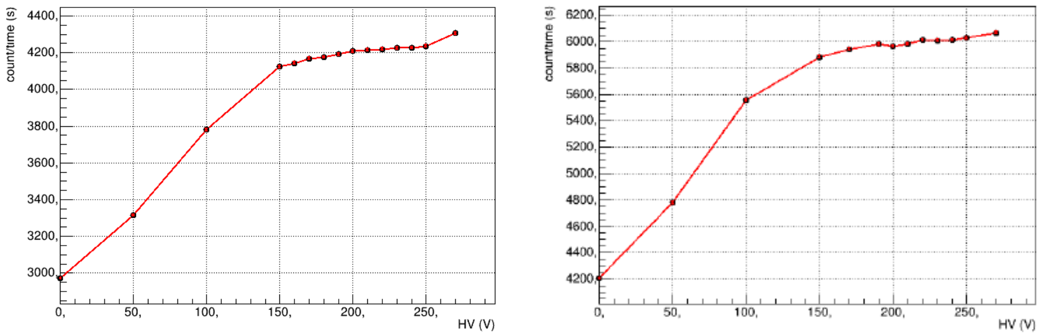

(a) BGEM foil number 6 (close to the TGEM). **(b)** BGEM foil number 5

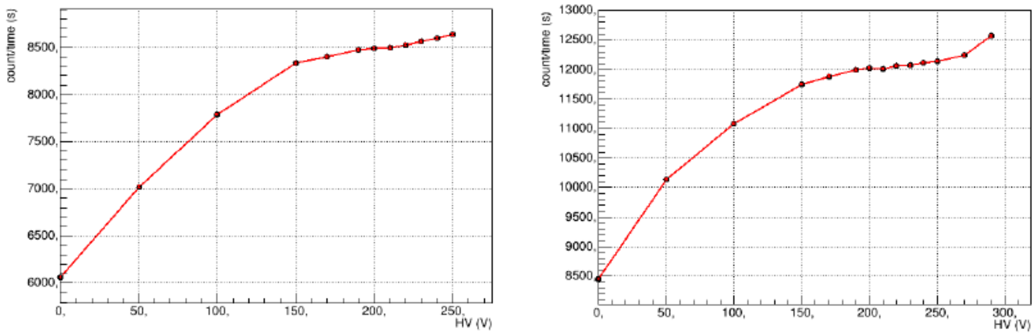

(c) BGEM foil number 4 **(d)** BGEM foil number 3

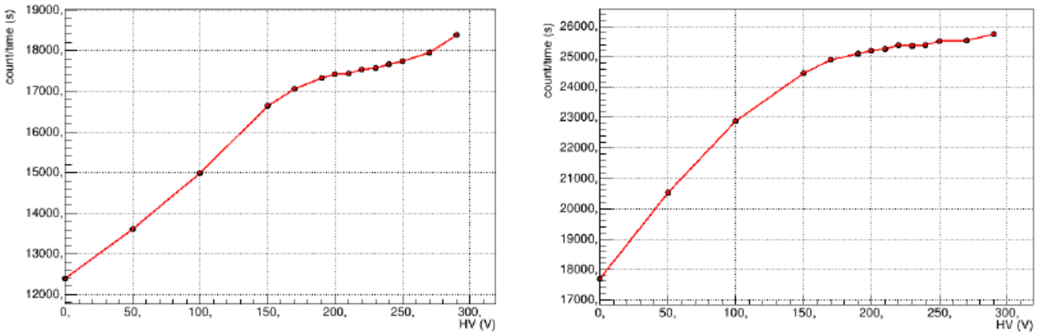

(e) BGEM foil number 2 **(f)** BGEM foil number 1

Figure 4.7: BGEMs HV scan. They show the increase of the count rate at the increase of the applied HV.

Graph	HV BGEM6	HV BGEM5	HV BGEM4	HV BGEM3	HV BGEM2	HV BGEM1
a	220 V	0 V	0 V	0 V	0 V	0 V
b	220 V	220 V	0 V	0 V	0 V	0 V
c	220 V	220 V	230 V	0 V	0 V	0 V
d	220 V	220 V	230 V	230 V	0 V	0 V
e	220 V	220 V	230 V	230 V	230 V	0 V
f	220 V	220 V	230 V	230 V	230 V	230 V

Table 4.1: HV values set to perform the BGEM HV scan.

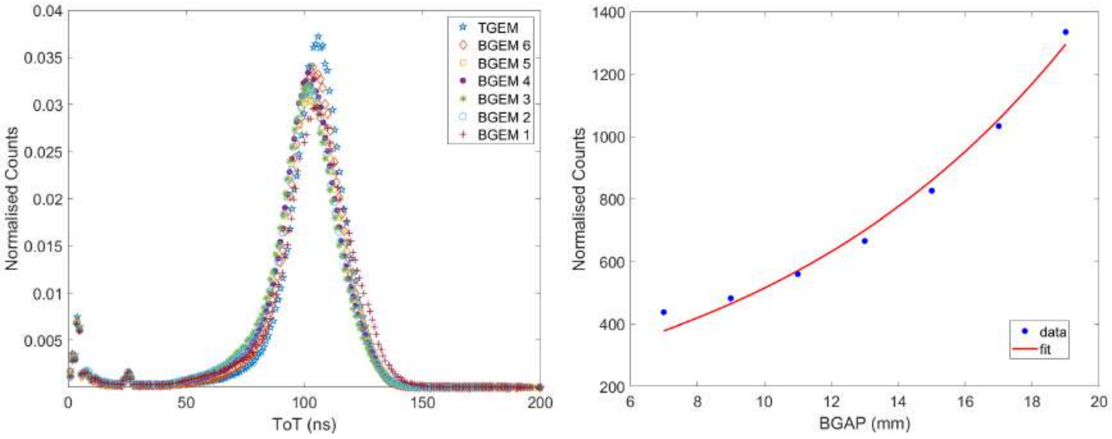

(a) (b)

Figure 4.8: (a)ToT spectra of a copper target performed with the HV reported inside table 4.1. (b) Trend of the total count rate with respect to BGAPs for each active boron layer.

Graph	HV (V)
(a) BGEM6	220 V
(b) BGEM5	210 V
(c) BGEM4	210 V
(d) BGEM3	220 V
(e) BGEM2	230 V
(f) BGEM1	190 V

Table 4.2: HV values provided by the residual analysis.

in function of the distances between the BGEM foils. The curve has been fitted with an exponential curve $a * e^{-bx}$, since this is the expected trend. In fact the beam attenuation follows the Beer-Lambert law $I = I_0 e^{-\mu x}$ where I is the final beam intensity I_0 is the incident beam intensity and μ is the attenuation coefficient. From this fit, the coefficents are: a=I_0=158.4±43 and b=μ=0.103±0.01 m^{-1}.

The last check to the set HV voltage has been performed choosing a reference run and calculating the variation of every run from the reference. The reference run is the measurement performed at the beginning of each scan with the BGEMs HV set to 0 V. The graphs have been obtained applying the relation 4.2

$$\frac{\sum_{bins}(\frac{\text{counts(run)}}{\text{counts(reference)}} - 1)^2}{\text{number of bins}} \tag{4.2}$$

and they are shown in figure 4.9. Each plot shows that the variation from the reference run has a minimum value, which indicates that the two spectra have similar count rates and shapes.

The minimum value for each plot is reported in table 4.2 and they indicate the correct HV to set at the 6MBGEM detector to have unitary gain in the conversion region.

4.4 Detector characterisation at L.E.N.A. reactor

The preliminary tests of the 6MBGEM detector with a neutron source have been conducted at the TRIGA Mark II reactor [31] located at the Laboratorio Energia Nucleare Applicata (L.E.N.A.) in Pavia [32].

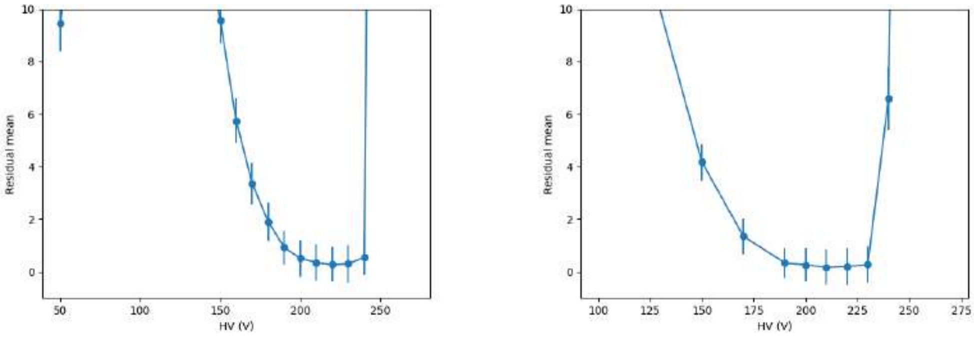

(a) BGEM foil number 6 **(b)** BGEM foil number 5

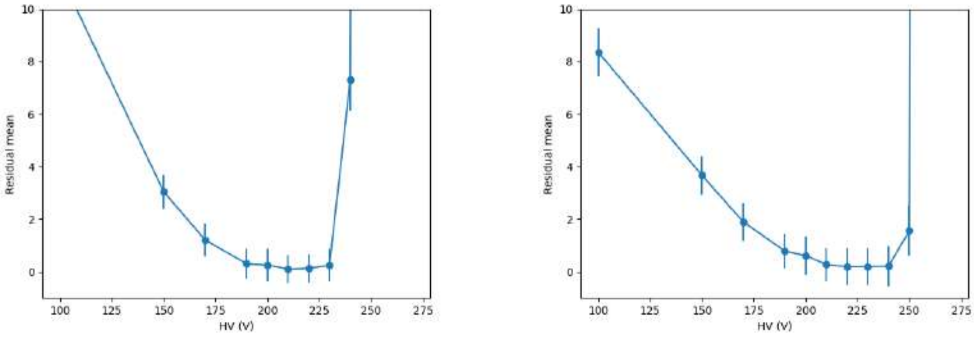

(c) BGEM foil number 4 **(d)** BGEM foil number 3

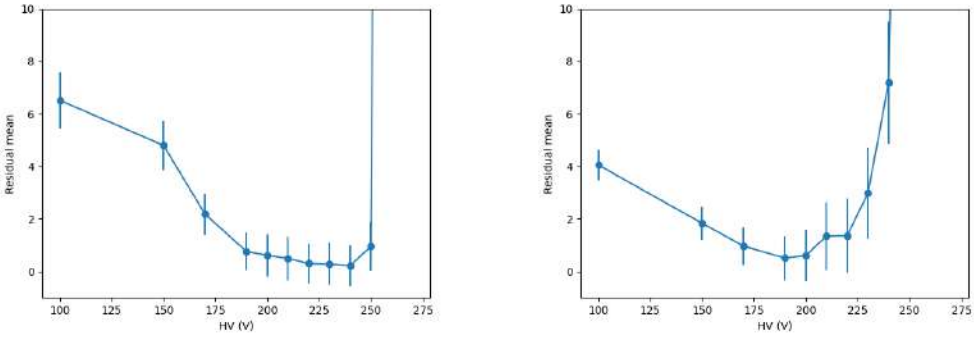

(e) BGEM foil number 2 **(f)** BGEM foil number 1

Figure 4.9: Study of the HV optimum values with the formula 4.2, where they are reached in the minimum point in the graphs.

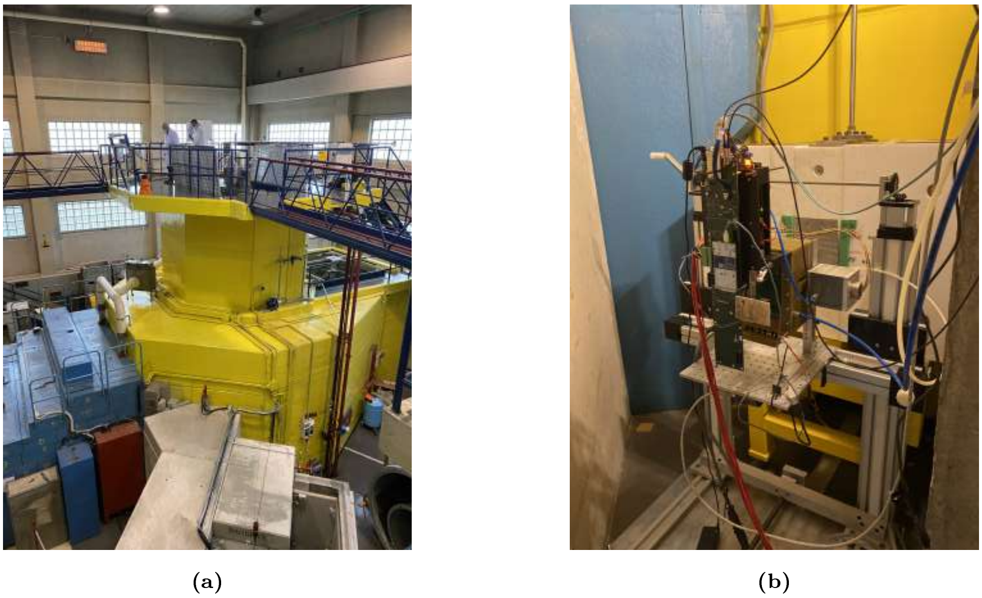
(a) (b)

Figure 4.10: (a) TRIGA Mark II reactor at L.E.N.A., the channel B [33] is the white box. (b) The 6MBGEM detector placed in front of the beam shutter with a Cd mask.

The reactor produces neutrons from the fission reactions n+235U → 236U* and the instable nuclei of 236U make fission producing two fission products and liberating an average of 2-3 neutrons per reaction. These neutrons are available to sustain the fission chain reactions and also to perform experiments [31]. The L.E.N.A. laboratory has recently installed a new thermal neutron beam line aimed to study Prompt Gamma Neutron Activation Analysis (PGNAA) [33].

The beamline is installed at channel B [33] and it is made of a 5.5 m cylindrical collimator and two filters, one of sapphire (100 mm thick) and one of bismuth (70 mm thick) respectively. The sapphire filter absorbs the fast neutrons and the bismuth removes the gamma background from the core. Then a series of iron and polyethylene rings slow down and thermalise the neutrons.

The 6MBGEM detector has been placed at 30 cm from the beam shutter and the active area is orthogonal to the incident neutron beam. A Cd sample 2 mm thick with a hole placed in its center with a diameter of 6 mm is inserted at the end of the beam shutter to have a collimated beam. With this configuration, it has been possible to study locally the detector response. Moreover, decreasing the neutron flux the detector performances can be explored maintaining the detector in a stable conditions, without damage the device or saturate the electronic readout.

Graph	BGEM6	BGEM5	BGEM4	BGEM3	BGEM2	BGEM1
a	300 V	0 V	0 V	0 V	0 V	0 V
b	300 V	230 V	0 V	0 V	0 V	0 V
c	300 V	230 V	230 V	0 V	0 V	0 V
d	300 V	230 V	230 V	230 V	0 V	0 V
e	300 V	230 V	230 V	230 V	230 V	0 V
f	300 V	230 V	230 V	230 V	230 V	230 V

Table 4.3: The BGEM optimum values obtained from the HV scans. The "f" graph is the final configuration.

The Cd collimates the incident neutron beam since it has at 0.5 eV a resonance called *black resonance*, where the neutrons with energies below 0.5 eV are absorbed [34]. The HV scans have been performed to determine the detector working point with this configuration. The TGEM HV has been set 880 V, in the middle of the plateau region. The BGEM HV scans have been performed for each BGEM foil to find the optimum HV values, which lie in the plateau region (figures 4.11). The optimum values allow to have only neutron conversion and they are reported inside table 4.3.

Once it has been determined the detector working point, it has been possible to determine the relative detection efficiency of the detector. The count rate for each addition of the layers set at the working point has been divided for the count rate with only one layer turned on while the others kept at 0 V (equation 4.3).

$$\frac{\sum_{n=1}^{12} (\text{total count rate obtained from each layer})_n}{\text{total count rate of the reference run}} \tag{4.3}$$

Where the reference run is the measurement of the TGEM HV scan in the plateau region (only one layer turned on) and the sum is related by the addition of the boron layers at each measurement up to 12 layers (as reported in table 4.3).

As shown in figure 4.12a, the linear increase of the relative detection efficiency with the addition of the number layers means that the electrons are only extracted from the hole without multiplication. Moreover, the trend is still linear with 12 boron layers and this suggests that it is possible add more layers since the neutrons after 12 boron layers are available to be converted by other layers. As reported in the simulations (chapter 3), the increase of the number of the BGEM foils brings to a plateau region in the detection efficiency, which means that the neutrons are almost fully converted.

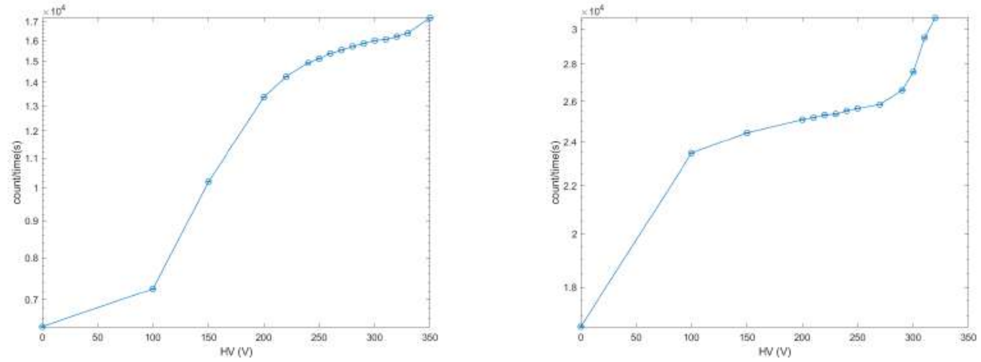

(a) BGEM foil number 6 (close to the TGEM). **(b)** BGEM foil number 5

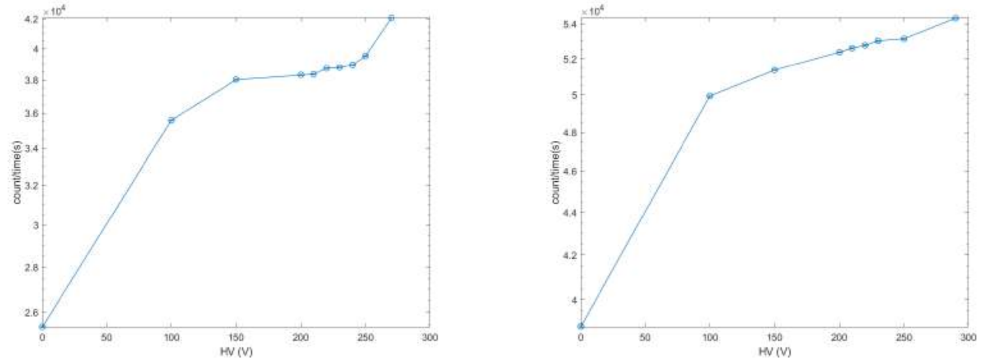

(c) BGEM foil number 4 **(d)** BGEM foil number 3

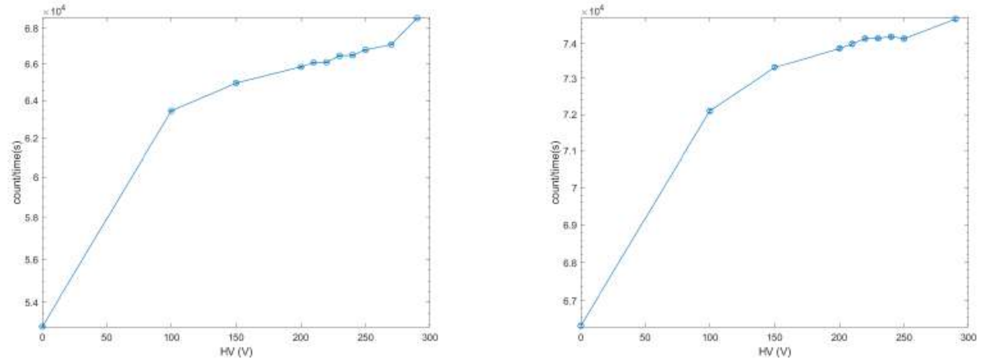

(e) BGEM foil number 2 **(f)** BGEM foil number 1

Figure 4.11: HV scan for the each 6 BGEM foils.

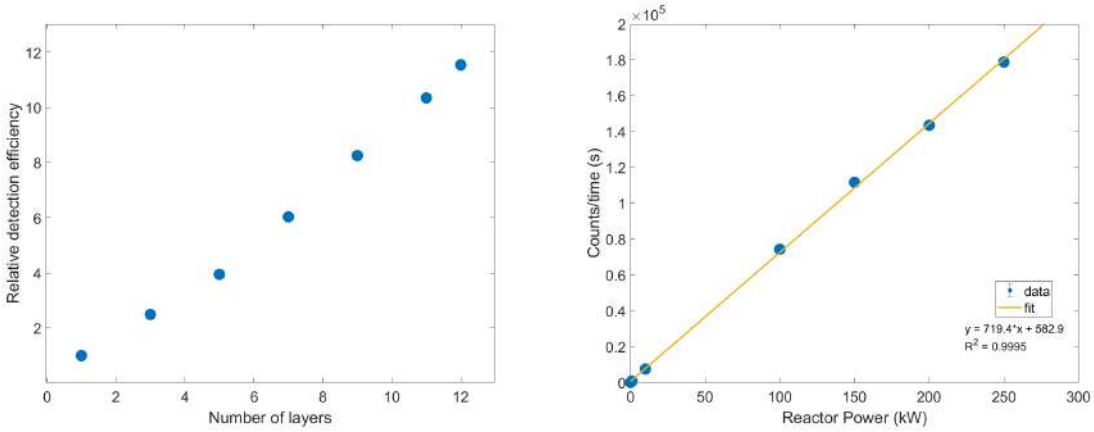

(a) **(b)**

Figure 4.12: (a) Relative detection efficiency with respect to the increase of the number of boron layers. (b) Reactor Power scan.

The graph reported in figure 4.12b shows the capability of the 6MBGEM detector to sustain high neutron fluxes. The beam line provides a thermal neutron flux in the order about 10^6n/s*cm^2 [33] at the maximum reactor power, which is 250 kW. For this test, the reactor power has been varied from 10 W to 250 kW and the detector response is almost linear in this power range.

4.5 Measurements at the ISIS Neutron and Muon Source

The ISIS Neutron and Muon Source [35] is a pulsed neutron facility located at the STFC Rutherford Appleton Laboratory, Oxfordshire (UK). The aim of the experiments performed at ISIS is to understand the nature of the materials.

ISIS is composed of three accelerators, two neutron target stations and two intermediate muon stations, twenty-eight neutron and eight muon experiments [36] (figure 4.13). Ions H^- are accelerated by the first accelerator, a Radio Frequency Quadrupole (RFQ), up to 665 keV. The next step is a linear accelerator (linac), where the ions are accelerated until 70 MeV; then ions enter into the synchrotron where at first electron are removed and the remaining protons are accelerated up to 800 MeV. The proton bunches are extracted with a frequency of 50 Hz and three bunches are directed to the target station one (TS1) and one proton bunch to the target station two (TS2). The targets are usually made with heavy metal materials, in particular ISIS operates with tantalum-clad tungsten targets; when the protons collide against the targets, the reaction called spallation takes place. During this reaction 15-20 neutrons per incident proton are liberated, then $2 * 10^{16}$ neutrons per seconds are produced.

The produced neutrons are emitted in all direction with energies in the order of MeV, thus it is necessary to slow down and guide them to the several instruments [35]. On this purpose, a series of moderators and reflectors are located around the targets. TS1 has two water moderators at 300 K, one liquid methane moderator at 100 K and a liquid hydrogen moderator at 20 K. TS2 has two water moderators, one liquid hydrogen moderator at 20 K and one solid methane moderator at 47 K. After the moderators, the beryllium reflectors are positioned and encapsulated by other moderators. The entire system is covered by a steel and concrete bio-shield called *the monolith*, which absorbs neutrons. Then, neutrons are guided towards the experiments and some beam-lines select the neutron energies through a chopper system, which are a series of rotating disk synchronized with the neutron velocity in order to select only the desired neutrons.

4.5.1 The VESUVIO beam line

VESUVIO [37] is a Time of Flight (ToF) spectrometer, where the ToF information is given by equation 4.4.

$$\mathrm{ToF} = \frac{\mathrm{L_0 + L_1}}{\mathrm{v}} \tag{4.4}$$

where $\mathrm{L_0}$ and $\mathrm{L_1}$ are the distances from the source-sample and sample-detector respectively, while v is the velocity of the incident neutron. Since the neutron energy is $\mathrm{E} = 1/2\ \mathrm{m}_n\mathrm{v}^2$ (m_n is the neutron mass), the neutron energy is linked with ToF by the following equation obtained using the equation 4.4:

$$\mathrm{E} = \frac{1}{2}\mathrm{m}_n\frac{\mathrm{L}^2}{\mathrm{ToF}^2} \tag{4.5}$$

where L is the total flight path ($\mathrm{L_0}$+$\mathrm{L_1}$).

Moreover, knowing the neutron energy, it is possible to determine the neutron wavelength from equation 4.6

$$\lambda = \frac{h * \mathrm{ToF}}{m_n * L} \tag{4.6}$$

where h is the Planck constat ($4.9 * 10^{-15}$ eV*s).

The beam-line (figure 4.14) is equipped with 196 detectors (for back and forward scattering), one incident and one transmitted monitor. The detectors placed in back scattering position are ^{6}Li doped scintillators.

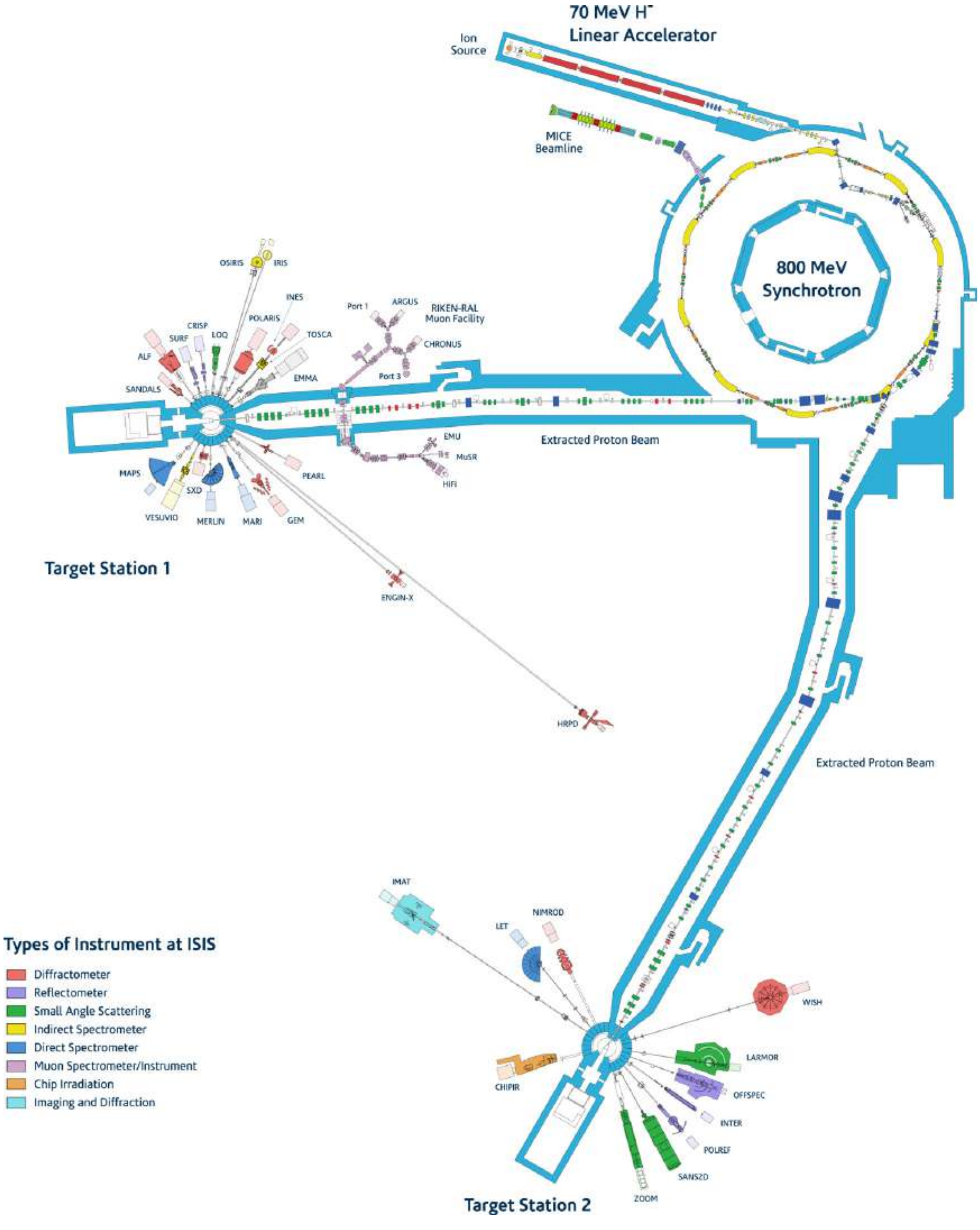

Figure 4.13: Scheme of the ISIS neutron facility [36].

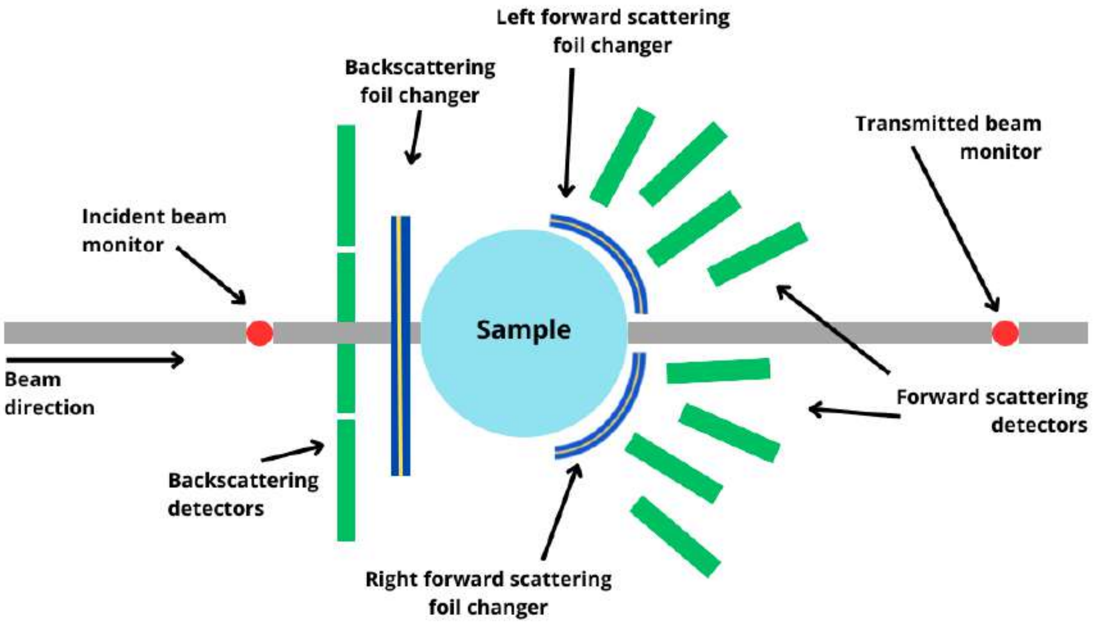

Figure 4.14: VESUVIO experiment scheme.

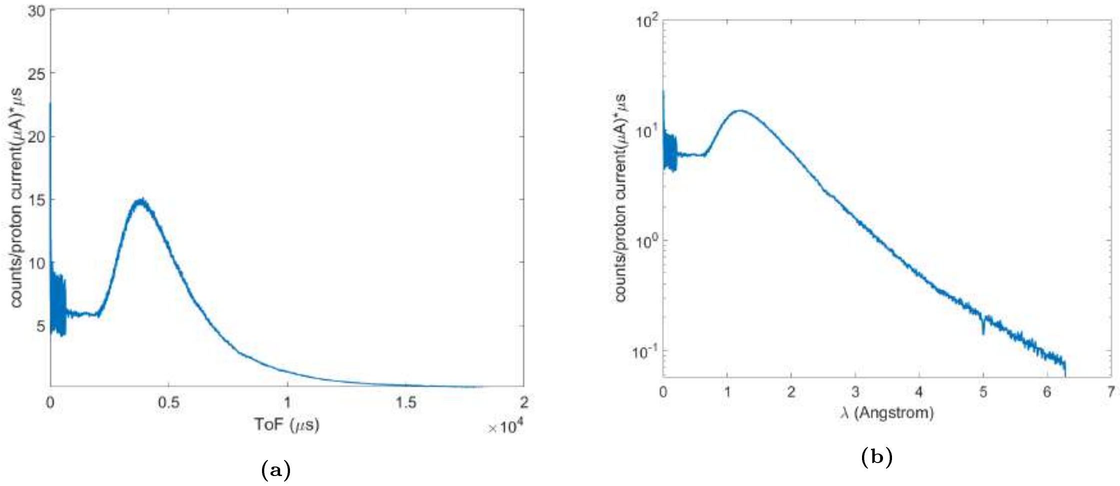

(a)

(b)

Figure 4.15: (a) ToF spectrum obtained with GS20 transmitted monitor. (b) Wavelength spectrum of obtained from (a) using the equation 4.6.

The transmitted beam monitor is the GS20 [38], a ^{6}Li-based scintillator placed at 13.43 m from the sample position. A typical ToF spectrum obtained with the GS20 transmitted monitor is reported in figure 4.15a and the respective wavelength spectrum is shown in figure 4.15b. The wavelength spectrum shows a peak around 1.5 Å with a Maxwellian shape, due to the moderation with water at room temperature, and a tail in the epithermal region [39]. The GS20 has a detection efficiency of 0.6% [40] at 82 meV. Recently in 2019, the beam-line has been equipped with another transmitted detector based on GEM detector with a detection efficiency of 1% [41]. This recent upgrade has demonstrated the possibility to performe experiments reducing the measurement time and to investigate better the cold and the epithermal neutron region [41]. The transmission geometry is very useful on VESUVIO to perform experiments aimed to determine the total neutron cross sections of the samples under study [42].

4.5.2 The 6MBGEM detector characterisation

The 6MBGEM detector has been positioned in transmission geometry (figure 4.16) at almost 1.60 m from the sample holder and in front of the GS20 transmitted monitor (at 40 cm). The t_0 start signal is provided by the hit of the proton bunches on the target and the stop signal (ToF) occurs when the neutron is absorbed and detected. With the ToF information, which correspond to the ToA information of the GEMINI readout, the ToF spectrum is obtained.

Figure 4.17 shows the ToF spectrum obtained with GEM detector and the respective wavelength spectrum. As for the GS20 spectrum in figure 4.15, the Maxwellian peak and the tail are visible .

A Cd sample 2 mm thick with a hole with 6 mm of diameter has been inserted inside the sample holder and the detector characterisation has been repeated as described in paragraph 4.5.1. The detector working point has been found setting the HV obtained from the scans for each foil; these HV values are reported inside table 4.4.

As reported in figure 4.18a, the 6MBGEM is capable to performe 2D spatial map since it is equipped with a padded anode. In fact, the figure shows the VESUVIO neutron beam profile collimated with the Cd mask. The counts present around the hole are due to the beam divergence and to the epithermal components, which are not absorbed from the black resonance.

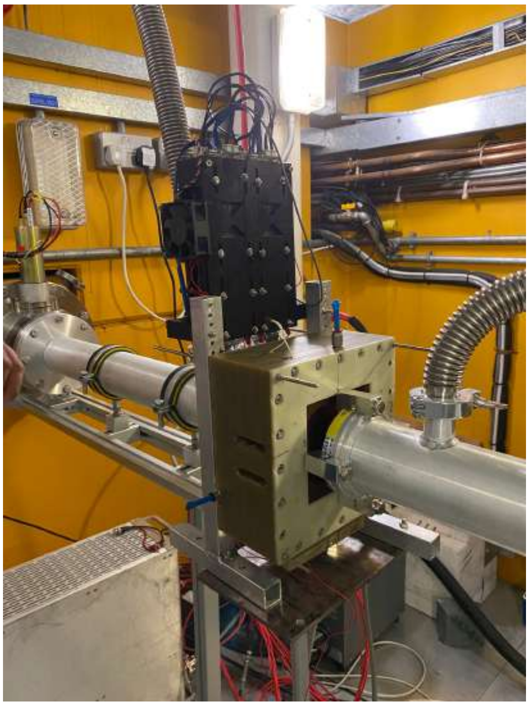

Figure 4.16: The 6MBGEM detector installed at the VESUVIO experiment. On the back is visible the GS20 transmitted monitor.

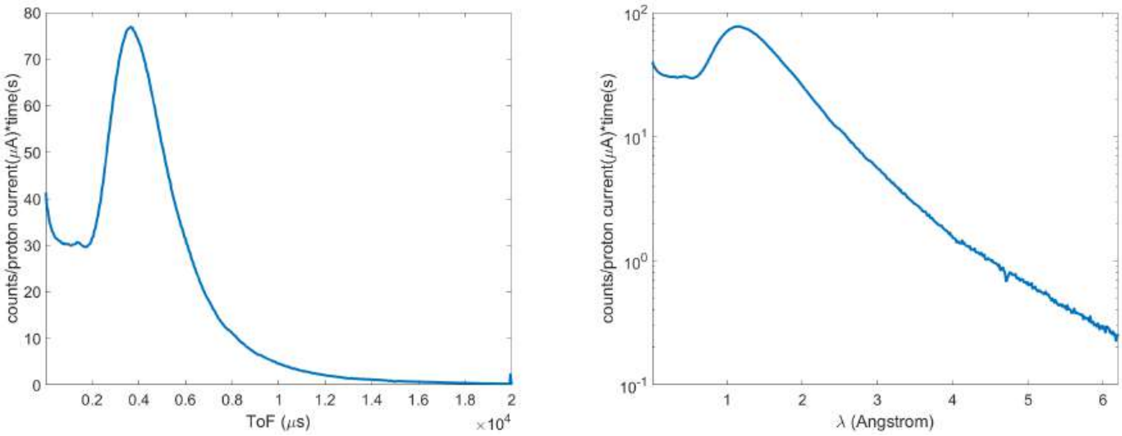

(a) **(b)**

Figure 4.17: (a) ToF spectrum obtained with GEM transmitted monitor. (b) Wavelength spectrum obtained from (a) using the equation 4.6.

Scan	HV (V)
TGEM	890 V
BGEM6	230 V
BGEM5	230 V
BGEM4	230 V
BGEM3	230 V
BGEM2	230 V
BGEM1	230 V

Table 4.4: HV values provided by the residual analysis.

Once the HV values have been fixed, the detector characterisation is aimed to provide:

- The capability to discriminate gamma rays from neutrons.
- The detector stability.
- The detection efficiency.

The detector capability to discriminate gamma rays from neutrons has been studied taking into account two different measuremets, one with the empty tank and the other one with a Cd mask 2 mm thick. This value provides an information about the discrimination of the neutrons from gamma rays of the entire set-up detector plus beamline, since the set up conditions can not allow to have two different system (one for the neutrons and one for the gammas) to estimate the gamma sensitivity.

As reported in figure 4.18b, the measurements have been normalised to the time measuremets and the analysis has been performed considering the total count inside the same ToF interval (from 2.5 μs to 20 ms). Thus, the gamma ray discrimination factor has been calculated as the ratio between the total counts of the measurement with the Cd sample and the total counts of the measurement with the empty tank (orange/dot curve and blu line respectively on figure 4.18b). This ratio has provided a value in the order of $1.36 * 10^{-5} \pm 0.06 * 10^{-5}$.

The detector stability has been analysed considering a series of run acquired in the same conditions for eight hours; for all measuremets the Cd mask with the hole has been inserted. Each run is about one minute long and ten minutes is the pause from one run to another, for a total of 43 runs, and the runs have been normalised for the proton beam current. Then, one run has been chosen has reference run and the total counts for each

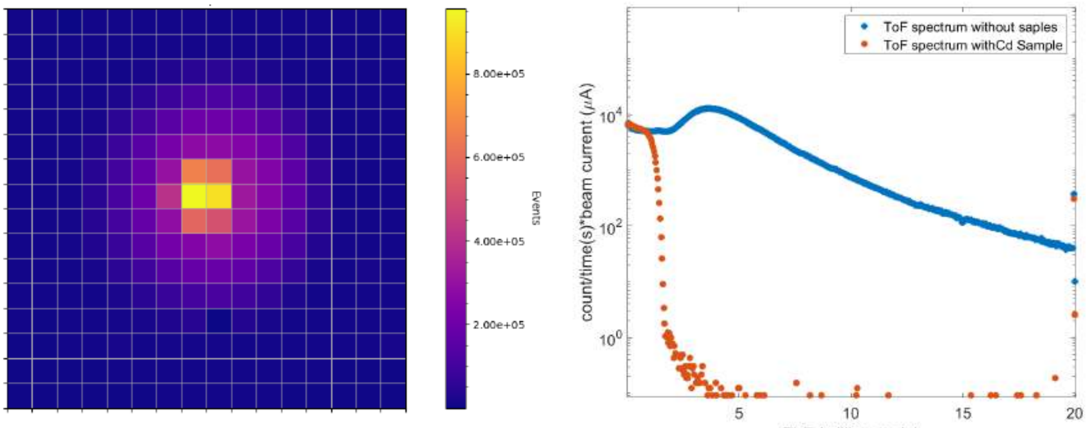

(a)

(b)

Figure 4.18: (a) 2D spatial map showing the VESUVIO neutron beam collimated with a Cd Mask with a hole of 6 mm. (b) The two ToF spectra used for the estimation of the detector capability to discriminate gamma rays from neutrons. The value has been found as the ratio of the total count present inside the black resonance (orange-dot plot, run with the Cd sample) and total counts of a run with empty beam (blue-cross plot) in the same ToF interval (2.5-20 ms).

run has been normalised for it. The graph 4.19b shows the plot of these normlised runs versus the 8 hours of measuremets and these values are positioned around the value 1. To evaluate the spread from the value 1, the values have been histogrammed and the Full Width at Half Maximum (FWHM) associated to the histogram (figure 4.19b) provides the instability of the detector. The FWHM is defined as 2.35 * standard deviation (Std. Dev. in graph (4.19b)) for a gaussian distribution. The obtained value is less than 1%.

The last graph reported in figure 4.20 shows the detection efficiency of the 6MBGEM (ε_{6MBGEM})detector with respect to the wavelength. The graph has been obtained considering the ratio between the count rate of a spectrum obtained with the GS20 transmitted monitor and the count rate obtained with the 6MBGEM detector. Then, following the equation 4.7, the ratio has been multiplied with the detection efficiency of the GS20 detector.

$$\varepsilon_{6MBGEM} = \frac{\text{counts}_{6MBGEM}}{\text{counts}_{GS20}} * \varepsilon_{GS20} \tag{4.7}$$

The values of the detection efficiency are given for each wavelength in the range from 0.5 Å to 6 Å. It increase with the increase of the wavelength in according to the boron

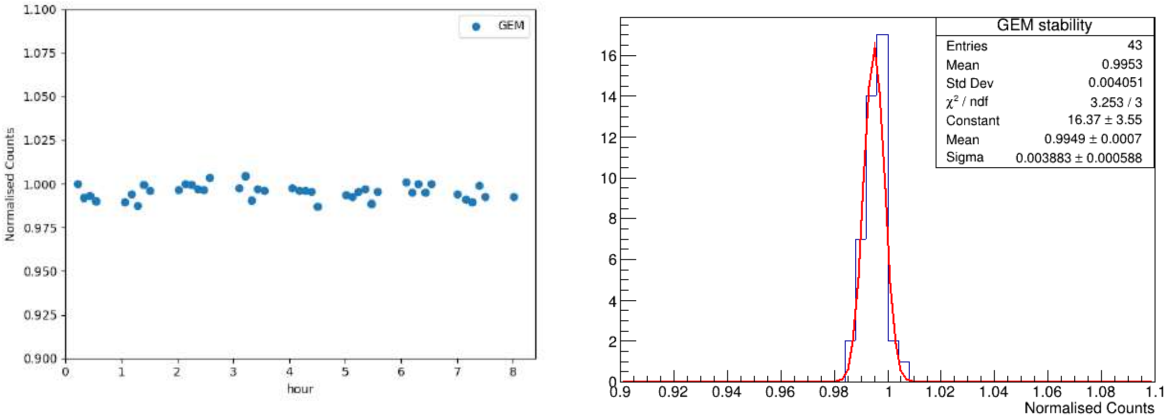

(a)

(b)

Figure 4.19: (a) Stability during time of the 6MBGEM detector. (b) Histogram of the values reported inside graph 4.19a with the gaussian fit (red line).

neutron cross section and it is 16% at 1.8 Å (25 meV). The maximum value is about 50% at 6 Åand the increase of the error bar in the last points is due to the low statistic in this spectrum region of the GS20 detector.

4.6 Conclusions

The 6MBGEM detector has been realised entirely inside Milano-Bicocca and ISTP laboratories and then characterised with an X-ray source and with two neutron sources.

The tests with the X-ray source have demonstrated the capability of the 6MBGEM detector to transport the charge along the BGAPS and through the holes. In particular even if six foils have been added to the standar triple GEM, the primary electrons from ionisation are easily extracted from the holes, guided toward the triple GEM and then multiplied.

The detector has been preliminarily characterised with a thermal neutron beam from a TRIGA Mark II reactor. The 6MBGEM detector can sustain high neutron fluxes and it has a linear response at the increas of the GEM foils inside the device.

Then, the characterisation has been performed at a pulsed neutron source, with neutrons in the energy range from thermal to epithermal neutrons. The detector has shown a good stability during time (99%) and a good capability to discriminate gamma rays from neutrons of $1.36 * 10^{-5} \pm 0.06 * 10^{-5}$. The detection efficiency depends on the

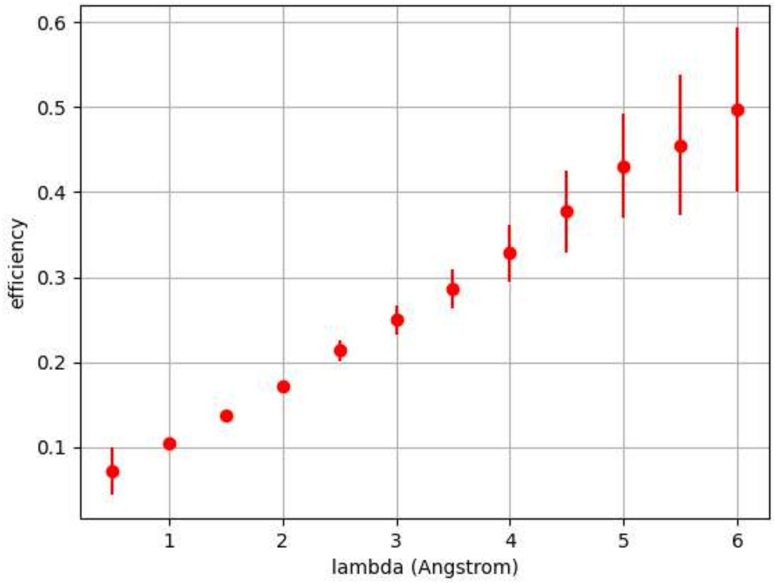

Figure 4.20: 6MBGEM detection efficiency values in function of the neutron wavelength.

wavelength considered and it is less than 10% for neutrons with wavelength 1 Å up to 50% at 6 Å.

Chapter 5

The GEMINI electronic readout

With the development of GEM detectors, a dedicated electronic readout was necessary. Different readout electronic have been developed, but since neutron sources provides high thermal neutron fluxes, such as ISIS or ILL (10^8 n/s*cm^2) [43], operate under this condition requires detectors and readout systems capable to sustain high count rates. One of the mostly used was the CARIOCA chip [44], a 0.25 μm CMOS technology equipped with 8 channels capable to sustain a maximum rate of 0.8 Mcps. Since GEM detectors anode is made of a series of pads, each chip can read 8 pads. Thus, increasing the pad number neither to cover larger areas nor to increase the spatial resolution, it increases the chip number needed.

Moreover, future neutron facilities, such as the European Spallation Source (ESS), will provide a neutron flux in the order of 10^9 n/s*cm^2; thus, a new electronic readout is necessary.

For this reason in 2016 the microelectronic group of Università degli Studi di Milano-Bicocca and Istituto Nazionale Fisica Nucleare (INFN)-Bicocca has developed a new custom chip for GEM detectors, the GEMINI [45] (GEM INtegrated Interface).

5.1 The GEMINI chip and the GEMINI system readout

The GEMINI (figure 5.1) is a System on Chip (SoC), an integrated circuit made of 16 channels, 16 Charge-Sensitive Preamplifiers (CSP) and 16 Discriminators. Each channel provides a charge signal, which is amplified and converted to a voltage signal (V_{PRE}) by the CPS. The voltage signal is compared by the Discriminator with a threshold (V_{TH}) settable for each channel by an R-2R resistive DAC (Digital to Analog converter). If the signal of V_{PRE} exceeds the V_{TH} (figure 5.1), the Time over Threshold (ToT) and the Time of Arrival information of the event are sent to a dedicated driver, which converts the output signal into a LVDS standard signal (see figure 5.2). The LVDS signal from the chip containing the ToT and the ToA information is read by an FPGA made of a series of TDC (Time to Digital Converter), which is able to collect events from all channels and each TDC can sample the input with a time resolution of 0.5 ns. The information is packed in a 64bit word containing the ToT, the ToA and the channel ID. Then, the data are sent with an optical fiber to the Data Aquisition System (DAQ), a Linux server where data are stored (figure 5.3).

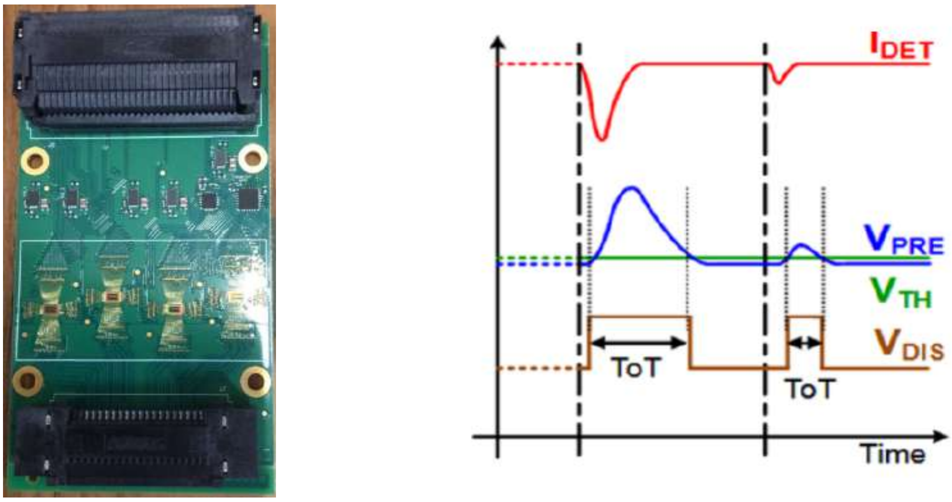

(a)

(b)

Figure 5.1: (a): GEMINI board photo with four GEMINI ASIC. (b): GEMINI signal digitalisation process.[46].

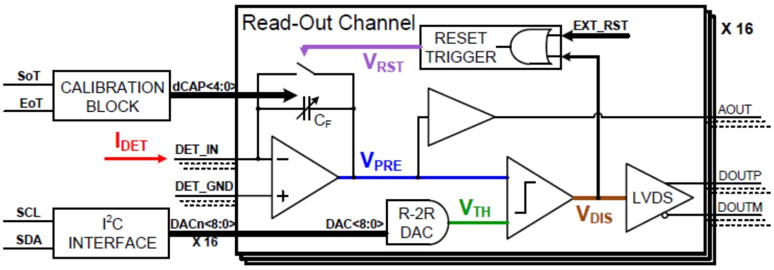

Figure 5.2: GEMINI chip scheme [45].

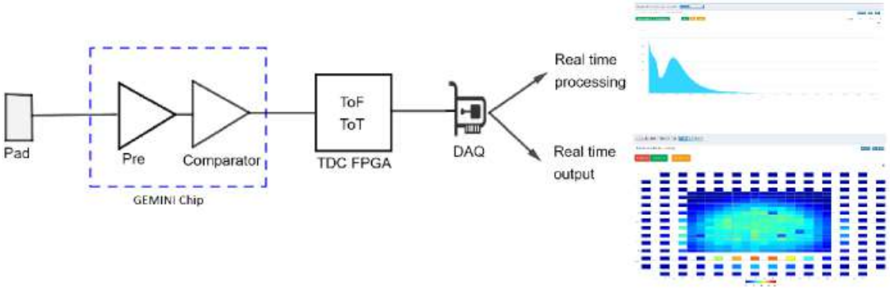

Figure 5.3: GEMINI electronic readout system.

5.2 Characterisation of the GEMINI chip response

The work described in this chapter provides the analysis of the signal coming from the GEMINI chip. With a dedicated board the analog signal has been extracted from the ASIC, analysed and then, compared with the digital signal. The aim of this study is to demonstrate that the information obtained with the GEMINI digital system is the same as a common analog electronic readout chain.

5.2.1 Experimental setup

The study has been performed with a triple GEM detector and two electronic readout systems, which work in parallel (figure 5.5, left). The GEM detector is made of an anode, three GEM foils covered with 5 μm aluminium instead of copper and a cathode. The system is put in an Ar-CO_2 70%-30% gas mixture constantly fluxed at 5 l/h. The measurements have been performed with an X-Ray tube [47], which emits a continuum bremsstrahlung superimposed with two Ag K-line at 22 keV and 25 keV respectevely. The X-Rays collide with a target, i.e. Titanium, and quasi-monochromatic fluorescence X-Rays are emitted to the detector. Different targets, such as titanium (Ti), copper (Cu) and molybdenum (Mo), have been used in order to obtain spectra with peaks at 4.5 keV, 8 keV and 17.4 keV respectevely.

To extract the analog signal from GEMINI, a custom board made of a LEMO connectors (figure 5.5, right) has been connected to the analog output (AOUT in figure 5.2), then 8 channels have been connected from analog output to a CAEN digitizer. For each event, it is obtained the waveform (figure 5.4), then a threshold is inserted (in our tests was 700 LVDS) and considering the time which the waveform stays over the threshold, the ToT information s obtained.

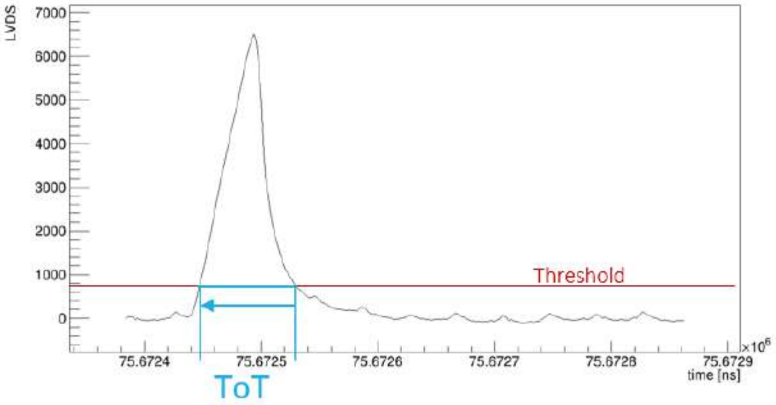

Figure 5.4: Event waveform from the CAEN digitizer. The threshold is set by a custom program and the difference between the last point over the threshold and the first one is the ToT.

At the same time, the event follows the digital chain described in section 5.1.

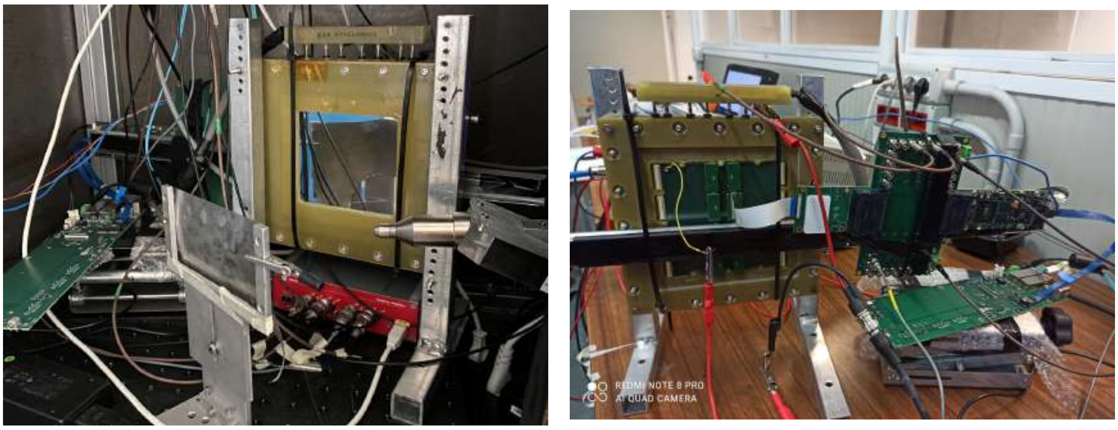

(a)

(b)

Figure 5.5: (a): Experimental setup. It is visible the X-Ray tube, the titanium target and the GEM detector. (b): GEM detector and GEMINI analog board on the right with the GEMINI ASIC and FPGA. Both spectra show the main peak at 4.5 keV and the Ar peak escape at 1.5 keV.

5.2.2 Detector calibration with the analog system

The detector calibration has been performed with two different methods, the ToT and the Pulse High (PH) methods. Both of them allow to obtain the energy spectra of different targets: like Ti, Cu and Mo.

To perform the calibration, a titanium target has been used in order to have spectra with a peak at 4.5 keV. Following the procedure described in the previous subsection the titanium spectra with the ToT and PH have been obtained for all 8 channels. Figures 5.6 show the same spectrum obtained with the two methods.

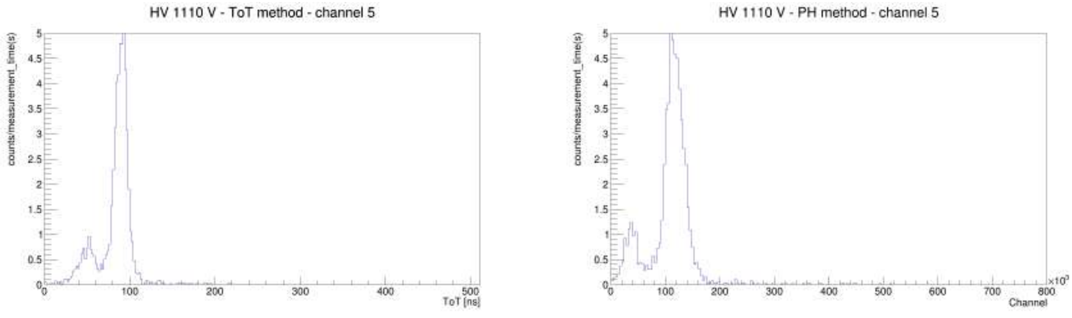

(a) **(b)**

Figure 5.6: (a): Titanium ToT spectrum at 1110 V of channel 5 obtained from the analog signal. ToT spectra have been obtained for all 8 channels. (b): Titanium PH spectrum of the same event reported in the bottom figure obtained at 1110 V of channel 5.

For both cases, the main peak at 4.5 keV and the Ar peak escape at 1.5 keV are visible. Varying the high voltage (HV) of the triple GEM, the detector gain changes. An HV increase means more electron multiplication and this effect is visible with a peak shift in the spectrum from low to high values of ToT and channels. The HV range takes to account is 1020-1140 V. HV lower than 1020 V doesn't allow the waveforms to exceed the threshold resulting in the loss of events, while HV higher than 1140 V brings discharges inside the detector.

The peaks have been fit with a gaussian distribution and the peak positions have been used to obtain the two calibration curves (figure 5.7).

The ToT calibration curve has been fit with the following equation

$$\mathrm{ToT} = a * \mathrm{Charge} + b - \frac{c}{\mathrm{Charge} - d} \tag{5.1}$$

while the PH curve with the straight line charge = a*channel+b.

From the fit parameters the charge spectra have been obtained for both methods, then with the equation 5.2 the corresponding energy spectra have been reported in figure 5.2.

$$\mathrm{Energy} = \frac{\mathrm{Charge} * E_{ion}}{e * G * K} \tag{5.2}$$

where E_{ion} is the energy necessary to create an electron-ion pair, which is 28 eV in

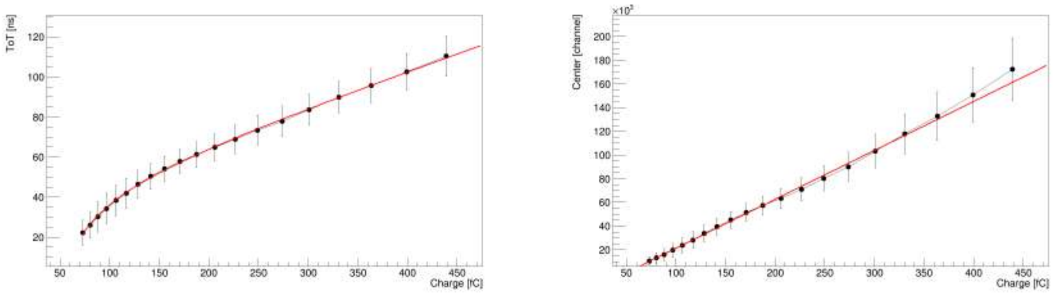

(a) (b)

Figure 5.7: (a): calibration curve obtained with the ToT method. The points are the centroid obtained from a gaussian fit of the main peak reported in figure 5.6. The curve has been fit with the equation 5.1. (b): calibration curve of the PH method fit with a straight line.

$\mathrm{ArCO_2}$, e the electron charge, G the gas gain and K the gain correction factor defined as

$$K = \frac{\text{Measured energy}}{\text{Expected energy}} \tag{5.3}$$

Through this procedure, the energy spectra of the Ti, Cu and Mo targets have been obtained, as reported in figures 5.8.

With a gaussian fit, the K-line for the targets have been found and the values are reported inside table 5.1

Targets	$\mathrm{Peak_{ToT}}$ (eV)	σ_{ToT} (eV)	$\mathrm{Peak_{PH}}$ (eV)	σ_{PH} (eV)
Ti	4555	706	4589	601
Cu	8500	1174	8500	1337
Mo	15800	1286	16600	1981

Table 5.1: Centroids with errors of the spectra reported in figure 5.8.

Comparing the centroid values, the Ti and Cu have a good agreement, in particular for both methods the peaks are centered at 4.5 keV and 8 keV respectevely. The Mo spectra show the peaks centered at 15.5 keV for the ToT and 16.6 keV for the PH method and the two values (obtained and expected) are in agreement within the error bars, as shown in figure 5.9, then it is possible to conclude that the two methods are well compatible.

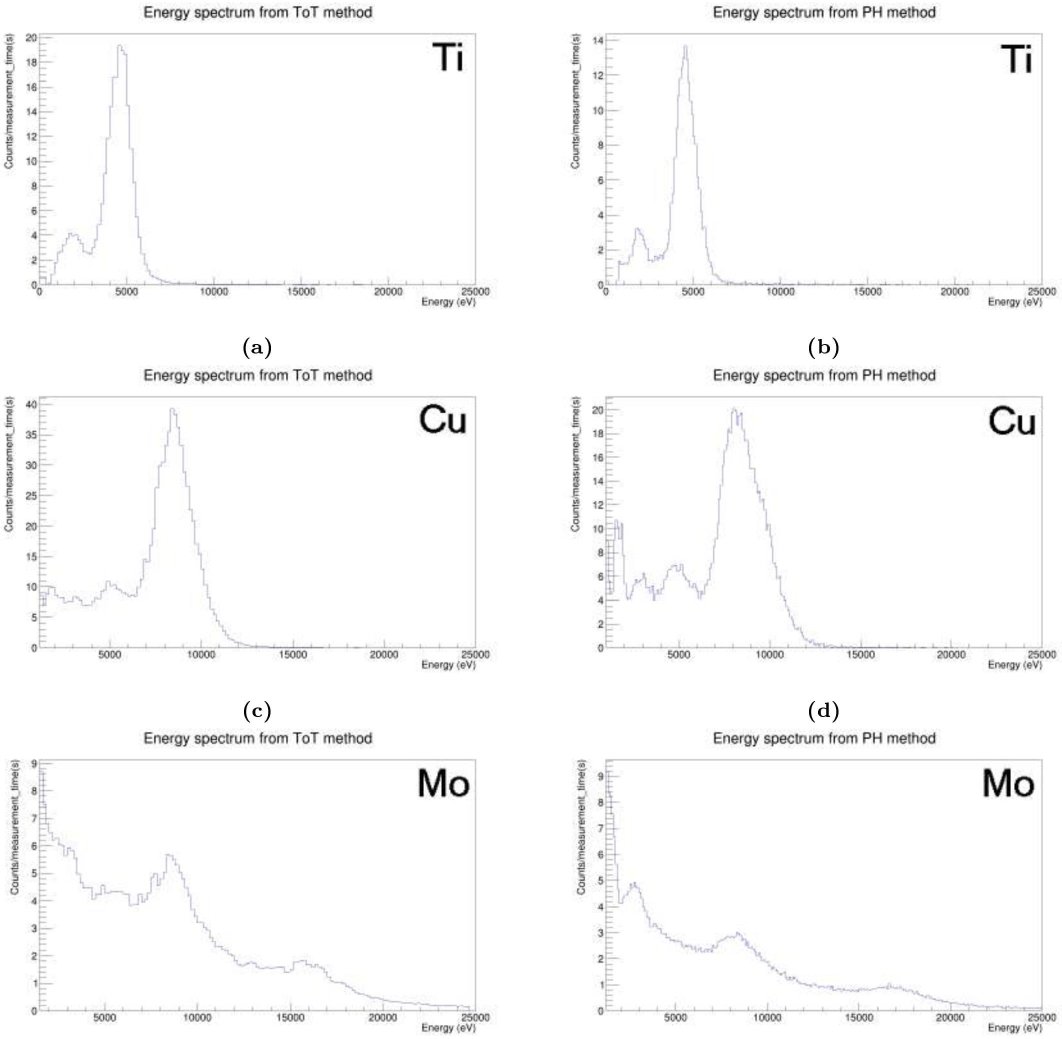

(a) **(b)** **(c)** **(d)** **(e)** **(f)**

Figure 5.8: Energy spectra of Ti, Cu and Mo targets. On the left (a,c,e) the spectra have been obtained with the ToT method, while on the right (b,d,f) with the PH method.

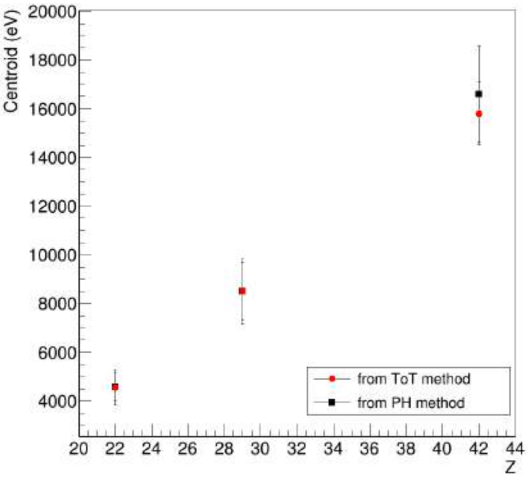

Figure 5.9: Comparison between the peaks obtained with the ToT and PH methods for the Ti, Cu and Mo targets (reported with their Z materials).

5.2.3 Comparison between analog and digital system

The final check is to verify that the ToT spectrum obtained from the analog signals is the same provided from the GEMINI digital chain. Then, the same measurement has been considered, in particular a measurement at 1110 V has been acquired with the digital and the analog system. Two spectra are reported in figure 5.10, showing only spectra of a single channel even if these spectra have been obtained for all 8 CAEN channels and 256 GEMINI channels.

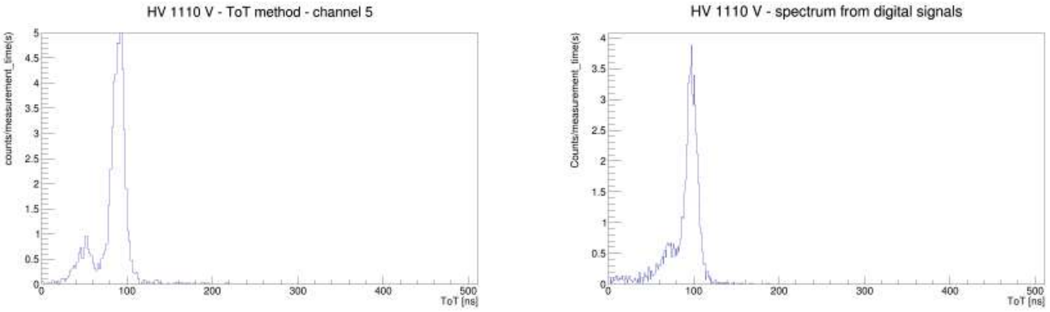

(a) (b)

Figure 5.10: (a): Ti ToT spectrum obtained from analog signals. (b): Ti ToT spectrum from GEMINI digital system.

The two figures don't show significant difference, in particular the main peak is centered at 90 ns and the Ar peak escape are clearly visible. Thus, the analog and digital methods provide the same results indicating that the use of the digital system can replace the old common analog chain providing good results.

5.3 Conclusions

In this chapter the study of the GEMINI electronic readout and a comparison between two GEM detectors has been reported.

The GEMINI signal has been analysed with two electronic chains obtaining the analog and digital signals. From the analog signal, the TOT and PH spectra of different target have been obtained and calibrated, in order to have the target energy spectra, which does not report significant differences. Thus, the TOT method can be used instead of PH, in particular in those applications where intense fluxes are expected, then a fast electronic readout is necessary to avoid event losses. A comparison between the analog TOT and the digital TOT has been done and the obtained TOT spectra for the same measurements don't show differences, thus the GEMINI digital system is a good electronic chain to perform experiments.

This work has been published in [48].

Conclusions

The PhD project reported in this thesis is focused on the development of an innovative GEM-based thermal neutron detector.

Appropriate simulations (Chapter 3) have been performed with the GEANT4 toolkit to determine the optimal gap dimensions between the BGEM foils and the boron thicknesses to apply to each BGEM foil. The chosen configuration consist of MBGEM detector with BGAPs of 2 mm thick and boron layers 1 μm thick; with the selection of such parameters the detection efficiency at 25 meV neutron energy is 18%.

Based on the simulations, a prototype of the MBGEM detector has been realised (chapter 4). The detector has been preliminarily tested with an X-ray source aimed to study the electron extraction capability. With this analysis, it has been demonstrated that the BGEM foils stack (the converting region) couples well with standard triple GEM stack (the electron multiplication region).

Then, the detector has been tested with a thermal neutron flux at the L.E.N.A. research center and it was demonstrated that the MBGEM response is linear with the increase of the BGEM layers number. Moreover, the MBGEM sustains the L.E.N.A. neutron flux up to 10^6 n/s*cm^2 without count rate saturation at the maximum reactor power, which is 250 kW.

Eventually, the MBGEM has been characterised at the ISIS Neutron and Muon source at the VESUVIO beam line with a pulsed thermal and epithermal neutron beam. The detector has shown a detection efficiency in the range from 16% at 1Å neutron wavelength up to 50% at 6Å. Moreover, it was determined that the detector has a counting rate stability of 99% during long periods of measurements (in the order of a few hours), and it is capable to discriminate gamma rays from neutron ($1.36 * 10^{-5} \pm 0.06 * 10^{-5}$ γ/n discrimination factor).

The capability of the MBGEM is also due to the electronic readout coupled with the detector, which is able to sustain high count rate without the pile up phenomenon. The

GEM electronic readout, called GEMINI, is an ASIC with the peculiarity to directly provide digital information. The study of GEMINI (Chapter 5) was aimed to compare the digital information with the corresponding analog information and to demonstrate that the digital "chain" constituted by the ASIC itself provides the same results as a standard, independent analog chain.

Tests on the GEMINI have been conducted with a standard triple GEM detector, an X-ray source and with different targets which emits monochromatic X-rays in the energy range of 1 keV up to 20 keV. The analysis has shown that the two electronic chains process the same signal providing the same result, which is the X-ray energy spectra emitted from the different targets (in units of Time over Threshold). Thus, the GEMINI electronic readout system coupled with the GEM detector provides the same results of an optimised electronic chain, with the added bonus of a very high count rate capability, and its use is indicated to perform experiments where a high neutron flux is expected on the detector.

In conclusion, the MBGEM detector coupled with the GEMINI readout has shown good properties in terms of detection efficiency and capability to sustain high count rates. Future development activity will make use of the MBGEM as a transmission detector to perform experiments aimed to determine the total neutron cross sections of selected physically interesting materials. On the other hand, the detector has demonstrated the capability to sustain high count rates, thus it will be possible to use it at SANS experiments, where high neutron fluxes are expected.

Publications

- S. Cancelli, et Al., "Characterisation of N2-GEM: a beam monitor based on Ar-N2 gas mixture", JINST, (2023), doi: https://doi.org/10.1088/1748-0221/18/05/C05005.
- S. Cancelli, et Al., "Electronic readout characterisation of a new soft X-Ray diagnostic for burning plasma", JINST, (2022), doi: 10.1088/1748-0221/17/08/C08028.
- S. Cancelli, A. Muraro, E. Perelli Cippo et Al., "Development of a ceramic double thick GEM detector for transmission measurements at the VESUVIO instrument at ISIS”, JINST, (2021), doi: 10.1088/1748-0221/16/06/P06003.
- Federico Caruggi, Stephanie Cancelli, et Al., "Performance of a triple GEM detector equipped with Al-GEM foils for X-rays detection", Nuclear Inst. and Methods in Physics Research, A 1047 (2023) 167855, doi: 10.1016/j.nima.2022.167855.
- Putignano, O., Muraro, A., Cancelli, S., Giacomelli, L., Gorini, G., Grosso, G., et al. (2023). Design of a Thick Gas Electron Multiplier based photon pre-amplifier. JOURNAL OF INSTRUMENTATION, 18(6), doi: 10.1088/1748-0221/18/06/C06003.
- O. Putignano, G. Croci, A. Muraro, S. Cancelli, et Al., "Conceptual design of a GEM (gas electron multiplier) based gas Cherenkov detector for measurement of 17 MeV gamma rays from T(D,γ)5He in magnetic confinement fusion plasmas", Rev. Sci. Instrum. 94, 013501 (2023), doi: 10.1063/5.0101761.
- Putignano, O., Croci, G., Muraro, A., S. Cancelli, Giacomelli, L., Gorini, G., et Al. "Investigation of a Cherenkov-based gamma-ray diagnostic for measurement of 17 MeV gamma-rays from T(D, γ)5He in magnetic confinement fusion plasmas", JINST, (2022), doi: 10.1088/1748-0221/17/02/C02021.
- Kushoro, M; Croci, G; Mario, I; Muraro, A; Rigamonti, D; Cancelli, S.; et Al., "Characterization of vacuum HV microdischarges at HVPTF through X-ray bremsstrahlung

spectroscopy", JINST, (2022), doi: 10.1088/1748-0221/17/01/C01054.

- A.Muraro, G.Claps, G.Croci, C.-C. Lai, R.De Oliveira, S.Altieri, S.Cancelli, et Al., (2021) “MBGEM : a stack of Borated GEM detector for high efficiency thermal neutron detection”, Eur. Phys. J. Plus, 10.1140/epjp/s13360-021-01707-2.
- Giovanni Romanelli, Dalila Onorati, Pierfrancesco Ulpiani, Stephanie Cancelli et Al., "Thermal neutron cross sections of amino acids from average contributions of functional groups", Journal of Physics: Condensed Matter, (2021), doi: 10.1088/1361-648X/abfc13.
- M. Rebai, D. Rigamonti, S. Cancelli, G. Croci , et Al., "New thick Silicon Carbide detectors: response to 14 MeV neutrons and comparison with single-crystal diamonds”, Nuclear Inst. And Methods for Physics Research, Volume 946, (2019), doi: 10.1016/j.nima.2019.162637.

Activities

Conferences

- 109∘ Congresso Nazionale, Società Italiana di Fisica (September 2023, Salerno). Short oral: Characterisation of the 6MBGEM: A boron-coated GEM-based neutron detector optimised for transmission measurements at spallation sources.

- 7th International Conference on Micro Pattern Gaseous Detectors (MPGD) (December 2022, Tel Aviv). Poster: Development of a Multi-layer Boron-coated GEM detector for slow neutron detection at spallation sources.

- 6th International Conference Frontiers in Diagnostic Technologies (October 2022, Frascati). Poster: Characterisation of N2-GEM: an innovative beam monitor for thermal neutrons.

- 108∘ Congresso Nazionale, Società Italiana di Fisica (September 2022, Milano). Short oral: A boron-coated GEM detector for thermal neutron transmission: Design and first results.

- 40th Meeting of the International Tokamak Physics Activity (ITPA) Topical Group on Diagnostics-ITER Organization (October 2021, online meeting). Oral: Al-GEM: an improved GEM based soft X-Ray diagnostic for Tokamaks.

- International Conference on diagnostic for fusion reactors (ICFRD 2020) (September 2021). Short oral: Characterisation of an aluminium triple-GEM detector coupled with GEMINI chip for soft X-rays detection in Tokamaks.

Schools

- H2020-ARIEL HISPANOS Hands-On school on the production, detection and use of neutron beams, Sevilla, Spain, September 2022.
- 4th Summer School on Neutron Detectors and Related Applications, Riva del Garda, Italy, July 2022.
- Online Summer School on Parallel Computing, Cineca, July 2021.
- Summer School "Green Energy Management (GEM) ASIA", Baku, Azerbaijan, September 2019.

Prizes

Winner of the award SIF-SoNS "Neutrons Matter" in recognition of her contribution to the development of innovative detectors with high spatial resolution for the advancement of neutron spectroscopy using the Time of Flight technique.

Teaching

- Tutor of the course "Fisica II" organised for the second year students of the Bachelor Degree in Physics at the Università degli Studi Milano-Bicocca, academic year: 2020/2021.
- Tutor of the course "Fisica II" organised for the second year students of the Bachelor Degree in Physics at the Università degli Studi Milano-Bicocca, academic year: 2021/2022.
- Tutor of the course "Fisica II" organised for the second year students of the Bachelor Degree in Physics at the Università degli Studi Milano-Bicocca, academic year: 2022/2023.
- Co-supervisor of the master student Hendry Alimagno (Università degli Studi di Milano-Bicocca). The thesis is titled: Development of GEM-based Beam Monitors operated in N2 for ESS-FREIA, dissertation on September 2022.

Review activities

Reviewer for the Journal Scientific Report.

Journal of Instrumentation

PAPER

Development of a ceramic double thick GEM detector for transmission measurements at the VESUVIO instrument at ISIS

To cite this article: S. Cancelli *et al* 2021 *JINST* **16** P06003

Published by IOP Publishing for Sissa Medialab

Received: *January 22, 2021*
Accepted: *February 25, 2021*
Published: *June 9, 2021*

Development of a ceramic double thick GEM detector for transmission measurements at the VESUVIO instrument at ISIS

S. Cancelli,[a,b,c,*] **A. Muraro,**[b] **E. Perelli Cippo,**[b] **G. Romanelli,**[d] **A. Abba,**[e] **Y. Chen,**[f,g] **G. Grosso,**[b] **G. Gorini,**[a,b,c] **Z. Hu,**[a] **C.-C. Lai,**[h] **O. Mc Cormack,**[a] **L. Robinson,**[h] **P.-O. Svensson,**[h] **M. Tardocchi,**[b] **R. Hall-Wilton,**[a,h] **Y. Xie,**[g] **S. Zhijia,**[f,g] **J. Zhou,**[f,g] **X. Zhou**[f,g] **and G. Croci**[a,b,c]

[a] *University of Milano-Bicocca, Piazza della Scienza 3, Milano, Italy*
[b] *Istituto per la Scienza e Tecnologia dei Plasmi, CNR, via Cozzi 53, 20125 Milan, Italy*
[c] *INFN Sezione Milano-Bicocca, Piazza della Scienza 3, Milano, Italy*
[d] *ISIS Facility, Rutherford Appleton Laboratory, Didcot OX11 0QX, U.K.*
[e] *Nuclear Instrument SRL, Via Lecco 16, Lambrugo (Como), Italy*
[f] *Spallation Neutron Source Science Center, 523803 Dongguan, China*
[g] *Institute of High Energy Physics, Chinese Academy of Sciences, 100049 Beijing, China*
[h] *European Spallation Source ERIC, P.O.176, 22 100, Lund, Sweden*

E-mail: stephanie.cancelli@unimib.it

Abstract: Neutron spallation sources always require new instrument upgrades and innovations in order to improve the quality of their experiments. In this framework, the capability to accurately measure total neutron cross sections at the VESUVIO instrument at the ISIS Facility can be boosted by a tailored transmission detector. For this reason, the first double ceramic thick GEM detector has been realised. Detectors based on GEM technology are broadly developed thanks to their characteristics, such as good spatial resolution (< 0.5 mm), good detection efficiency, high rate capability (MHz/mm^2) and a possible coverage area of some meters at low costs. This article shows the realisation of a GEM detector made of a $^{10}B_4C$ cathode, two ceramic thick GEM foils and a padded anode, as well as the device characterisation on the VESUVIO beam line, where stability, γ-sensitivity, imaging capability and sample analysis have been studied. The successful results confirm that the ceramic thick GEM detector performs well in thermal and epithermal neutron detection and it will allow the scientific user community of the instrument to perform better quality transmission measurements so as to determine more accurate total neutron cross section of condensed-matter systems.

Keywords: Micropattern gaseous detectors (MSGC, GEM, THGEM, RETHGEM, MHSP, MICROPIC, MICROMEGAS, InGrid, etc); Neutron detectors (cold, thermal, fast neutrons); Gaseous detectors

---

[*] Corresponding author.

https://doi.org/10.1088/1748-0221/16/06/P06003

2021 JINST 16 P06003

Contents

2021 JINST 16 P06003

1 Introduction

Thermal and epithermal neutrons are important probes for the study of the structure and dynamics of condensed-matter systems. Neutron experiments, such as spectroscopy, diffraction and radiography, are performed at large-scale neutron sources. At the ISIS [1] Neutron and Muon Source, the VESUVIO [2] spectrometer has a dedicated user programme aimed at the measurement of the total neutron cross sections over a broad energy range for incident neutrons, spanning from ca. 1 meV up to ca. 1 MeV. Current experiments are performed using the GS20 (a ^{6}Li-doped glass scintillator) monitor described in ref. [3], yet the quality of transmission measurements could be largely improved by using a new dedicated detector, tailored to the instrument geometry, with an improved discrimination of neutrons from the gamma rays of the background environment. Furthermore, imaging capabilities of a new detector of this type would allow the measurement of smaller or non-homogeneous samples, as opposed to what is required at present. To this purpose, the best choice which meets these demands is found in the micro-pattern gaseous detector (MPGD) based on the gas electron multiplier (GEM) technology. Thanks to their various advantages, GEM detectors [4] are widely used in many physics fields, such as high-energy physics [5], medical physics [6] and plasma physics [7]. Although GEM-based detectors are mostly used to detect charged particles, these detectors can be adapted to detect neutral particles, such as neutrons and photons [8–19]. Their main characteristics are high rate capability (MHz/mm^2), good detection efficiency, a spatial resolution better than 0.5 mm and the possibility of detector realisation of

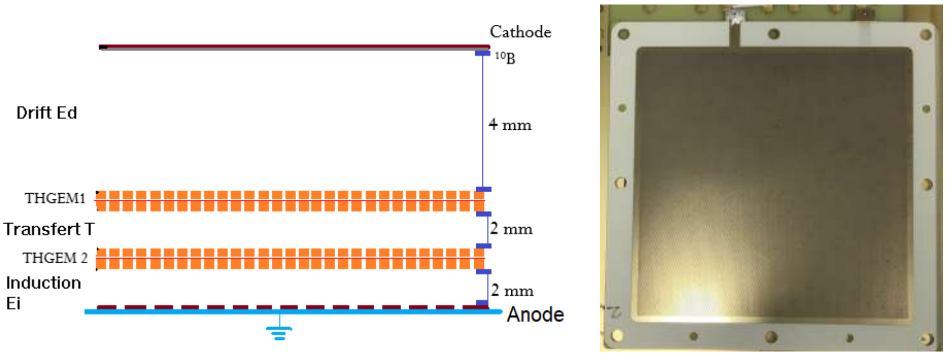

Figure 1. Left: schematic layout of the detector, with a summary of distances between elements. Right: a gold ceramic thick GEM foil.

different sizes (meters) and shapes. This paper describes the development of the first ceramic double thick GEM detector optimised for thermal detection with a cathode coated with $^{10}B_4C$ and the tests at the VESUVIO beam line.

2 Detector realisation

The ceramic double thick GEM (THGEM) detector described in this paper is composed of a $^{10}B_4C$-coated cathode, two ceramic THGEM foils and an anode, made of 384 pads; the entire system is put in an Ar/CO_2 70%/30% gas mixture. The cathode is a 130×130 mm^2 Al sheet of 200 µm thickness coated with 1.2 µm of $^{10}B_4C$ in the center of one side, where the coated active area is masked to about 100×100 mm^2, as can be seen in figure 1. The nominal detection efficiency of this coating is ca. 4% for thermalised neutrons [20, 21]. The deposition of the 10B4C coatings was carried out by direct current magnetron sputtering in Linköping Detector Coatings Workshop of European Spallation Source in Sweden [22]. Properties of the coatings has previously been characterized to meet the standards as neutron converting layers for detectors, e.g. the coatings are radiation hard [22, 23]. In order to have minimum deformation on the Al sheet, a low-temperature ($< 300°C$) coating process was developed to reduce the residual stress in the coatings and thermal expansion of the substrates [24].]. Notice that the thickness of the cathode in this work is only half of what has been published previously [25], while the coating thickness is 1.5 times thicker.

In the $^{10}B_4C$ coatings, the nuclear reaction used for the slow neutron detection is:

$$^{10}\mathrm{B} + \mathrm{n} = \begin{cases} ^{7}\mathrm{Li}{+}\alpha & \text{Q-value=2.792 MeV ground state, B.R.= 6\%} \\ ^{7}\mathrm{Li}^{*}{+}\alpha\ (1.47\,\mathrm{MeV}){+}\gamma(0.48\,\mathrm{MeV}) & \text{Q-value=2.31 MeV excited state, B.R.= 94\%} \end{cases}$$

Since the two charged products have energy in the order of 1 MeV and they are emitted back-to-back, the $^{10}B_4C$ thickness has been chosen in order to allow one of the two charged particles to exit the cathode and to enter inside the drift region, where gas ionization takes place [26].

The two THGEM foils have been developed at the China Spallation Neutron Source (CSNS) [27] and they are made of a 170 µm thick ceramic layer, covered on both sides with 15 µm of gold (THGEM1, figure 1) and copper (THGEM2).

Table 1. Concentration of the elements contained in the ceramic THGEM foils [30] with their neutron cross sections taken from ENDF/B-VIII.0 database and macroscopic cross section of the ceramic.

Element	Cross Section (barns) at 25 meV	Mass Ratio
H	31.6	—
C	4.98	—
O	3.94	48.5%
Na	3.91	2.4%
Ca	3.08	0.2%
Si	2.16	34.3%
Al	1.69	8%
Macroscopic cross section	0.42 cm^{-1}	

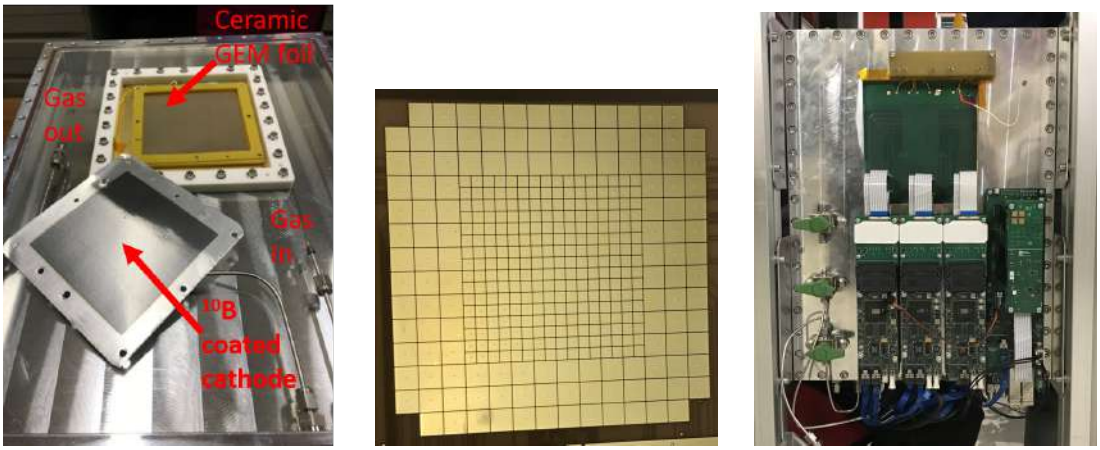

Figure 2. Left: inner structure of the detector. Center: the anode made of 384 pads(256 3×3 mm^2 inner pads and 128 6×6 mm^2 external pads). Right: GEM detector electronic readout: six GEMINI chips have been located on the detector outside the neutron beam.

The holes have a cylindrical shape and they are placed in an hexagonal arrangement with a 600 µm pitch. They have a diameter of 200 µm and a rim of 80 µm [28].

As reported in table 1, the ceramic THGEMs contain oxygen (48.5%), aluminum (8%) and silicon (34.3%) and these elements are characterised by a low total neutron cross sections. The main feature is the absence of hydrogen, which minimizes scattering of neutrons by the foils [29] and makes the ceramic THGEM innovative with respect to standard GEM foils made of Kapton or FR-4. As described by J. Zhou et al. in [30], the ratio between neutrons passing through GEM foils and incident neutrons at 25 meV is 97% for the ceramic THGEM foils. This ratio is 94% for FR-4 GEM foils, then ceramic THGEMs are more suitable than FR-4 GEM foils for neutron detection.

After the two THGEM foils, an anode is composed of 384 pads with different dimensions (256 3×3 mm^2 inner pads and 128 6×6 mm^2 outer pads). The output signal from the anode is processed by GEMINI ASICs [31], a custom electronic readout developed for GEM detectors. Each ASIC has 16 detecting channels and each channel has a Charge Sensitive Preamplifier (CSP)

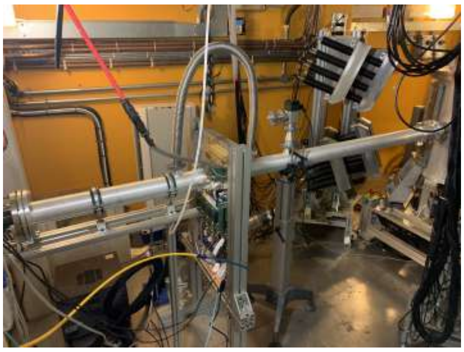

Figure 3. GEM detector in transmission position on the VESUVIO beamline.

and a discriminator.

The discriminator threshold can be set separately for all channels, thus constituting a significant improvement with respect to the previous CARIOCA-based readout [32], where thresholds may be set in groups of 8 channels only. GEMINI ASICs can operate in both Time over Threshold (ToT) [33, 34] and Time of Arrival (ToA) mode at the same time. In the present application, where the use of the neutron Time Of Flight (ToF) technique was envisaged, the ToA mode has been used. The detector has been designed so that the electronic readout is located outside the neutron beam, as shown in figure 3, in order to reduce the back scattered neutron component, the activation of the materials and the soft error probability. The Data Acquisition (DAQ) System is completed by custom FPGA board to store the raw data and to process data in real-time without overloading the system. The data are eventually loaded via a fast (up to 400 Mevents/s) optical fibre system to a remote Linux server.

3 Experimental setup

At the VESUVIO beam line, the detector was placed at a flight distance of L=12.6 m from the neutron source and at 1.6 m from the sample position within the vacuum tank (figure 3). At ISIS target station 1, a 800 MeV proton beam collides with a Ta-W target providing about 30 neutrons per incident proton and 4 bunches reach the target with a frequency of 50 Hz. The VESUVIO beam line has a room temperature water moderator. However, VESUVIO has the characteristic to be slightly under-moderated, thus the available neutrons belong to the thermal and epithermal energy range. The neutron energy spectrum is characterised by a Maxwellian shape in the thermal region with a peak at almost 30 meV and a $E_n^{-0.9}$ shaped tail in the epithermal region [35].

4 Detector Characterisation

The detector characterisation is aimed at setting the detector *working point*, i.e. the total applied voltage (HV) to the GEMs and the threshold of the GEMINI chips. Such parameters may be determined via a high-voltage scan and a threshold scan. The working point determination has allowed to determine in optimum conditions the detector efficiency, the detector stability, the γ-sensitivity and the imaging capability.

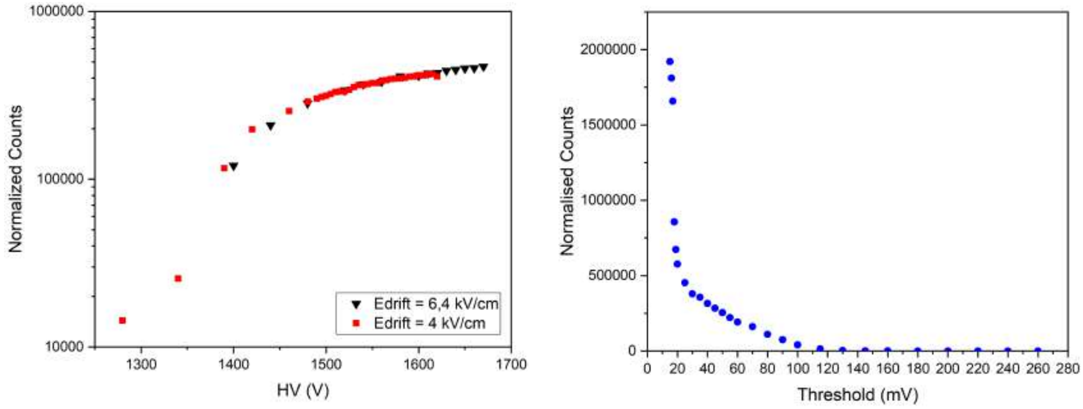

Figure 4. Left: the high-voltage scan shows the rise of the total counts with the increase of the HV applied to GEM foils. Two high voltage scans have been performed, with two different drift fields of 4 kV/cm (red dots) and 6.4 kV/cm (black dots) respectively. Right: threshold scan graph shows the decrease of the total counts with the increase of the threshold from 16 mV to 240 mV. The errors have been calculated for each measurement reported on left and on the right panels. The error bars are present but smaller than points.

4.1 Determination of the working point and detector efficiency

As reported in figure 4, the high-voltage scan has been performed by varying the sum of potentials applied to the two GEM foils ($\Delta V_{GEM1} + \Delta V_{GEM2}$=HV) in two configurations, with a drift field of 4 kV/cm and then 6.4 kV/cm. For both configurations, the total counts have been normalised by the measurement times and by the cluster size value (see subsection 4.1.1). Setting a HV of 1340 V, thermal neutrons start to be detected and the counting rate plateau region is reached at 1600 V (corresponding to an electron gain of almost 200).

The threshold scan has been performed by varying the GEMINI discriminator threshold from 16 mV to 240 mV. The graph on the right panel of figure 4 shows the total counts normalised to the measurement times. From 16 mV to almost 30 mV the signal is dominated by electronic noise. From 30 mV to 100 mV the counts are mostly due to neutrons and last region (100-240 mV) the signal does not exceed the threshold, thus no counts are present. The working point values used in this analysis are reported in section 4.2.

4.1.1 The cluster size value

The cluster size is the quantification of a phenomenon resulting from the energy deposition by the charged particles in the gas. After the conversion of the neutrons into alpha and Lithium particles, these charged products release a fraction of their energy during the motion in the gas (on the order of the mean free path). From an alpha particle, for instance, the primary electrons are produced along a 4 mm track in Ar/CO_2. The resulting electron cascade preserves the dimensions of such a track in first approximation. Therefore, the electronic cloud resulting from a single neutron conversion event may be detected by more than one pad.

The cluster size value is an estimation of the average number of pads fired per single neutron event and it is necessary to estimate the real count rate measured by the detector.

The cluster size of the detector is empirically defined as

$$\text{Cluster size} = \frac{\sum \text{number of fired pads per event}}{\text{number of acquired events}} \tag{4.1}$$

where the acquired events are processed by a custom software developed at the Istituto per la Scienza e Tecnlogia dei Plasmi (ISTP) [36], which identifies adjacent pads highlighted within a time window of 20 ns. These pads are considered highlighted from the same single event.

From the software, the obtained cluster sizes for all the performed measurements lie between 1 and 2 and they increase with HV. In fact, a cluster size of 1 has been obtained applying a HV of 1280 V and a value of 1.81 has been found with HV of 1670 V. These values mean that on average each neutron highlights one pad at 1280 V and 1.81 pads at 1670 V with our pad dimensions.

4.2 Detection efficiency

The THGEM detection efficiency (ε_{GEM}) has been estimated once the detector working point was found. The set values as working point are:

- An HV of 1610 V.
- A threshold of 40 mV.

Applying these parameters, the detection efficiency has been found as

$$\varepsilon_{\text{GEM}} = \frac{\text{Energy spectrum obtained with THGEM}}{\text{Energy spectrum obtained with GS20}}\,\varepsilon_{\text{GS20}} \tag{4.2}$$

where $\varepsilon_{\text{GS20}}$ is the GS20 detection efficiency, which has been estimated as 0.6% [37] at 82 meV. Since $\varepsilon_{\text{GS20}}$ decrease as $\frac{1}{\sqrt{\text{E}_n}}$ in the energy range (0.001-150) eV, different GS20 detection efficiencies have been calculated. The analysis shows an $\varepsilon_{\text{GS20}}$ of 3% at 3 meV, 0.9% at 30 meV and 0.02% in the interval from 100 eV to 200 eV. Making use of the previous values for $\varepsilon_{\text{GS20}}$ in equation (4.2), the obtained GEM detection efficiencies are 2.1%±0.2% at 3 meV, 1.15%±0.01% at 30 meV and 0.88%±0.08% in the interval from 100 eV to 200 eV.

4.3 Detector stability

Figure 5 shows the detector stability compared to the VESUVIO incident monitor. A run series, each run spanning exactly 30 min, for 12 h, has been acquired with the THGEM detector and the GS20 detector. All measurements have been normalised for the measurement times and for a reference run, which is a measurement taken at the beginning of the run series in the same conditions. Moreover, the value of the transmission in the figure corresponds to the average value over all incident neutron energies. The ratio between the measurements and the standard run is expected to be a value around 1. The deviation from this value provides information on the THGEM detector stability.

The right panel on figure 5 shows the distribution of the data reported on the left panel. The value of the FWHM divided by the centre of the distribution provides a stability value of 2%, which is a good result respect to previous GEM detectors [38].

2021 JINST 16 P06003

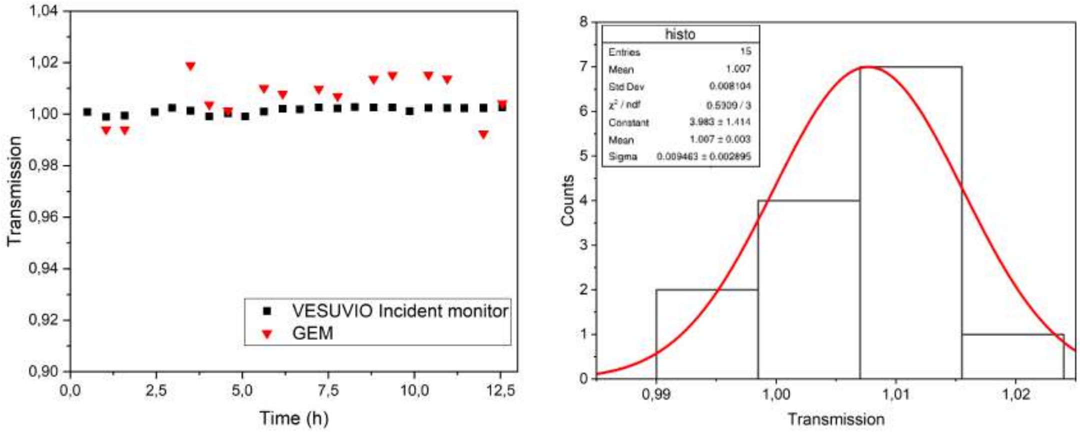

Figure 5. Left: variation of the total counts for GEM detector (red dots) and GS20 incident monitor (black dots) run series during 12 h. The error bars are present but smaller than the points. Right: histogram of total counts of GEM detector run series. For both graphs, the error bars are present but smaller than dot dimensions.

It is important to note that the points in the left panel of the figure correspond to measurements performed concurrently, yet independently, by the GS20 and GEM detectors. In fact, as a considerable number of neutrons are transmitted through the GEM, especially at epithermal energies but also at thermal energies, the two detectors can operate at the same time. This feature provides a powerful tool to correct, a posteriori, for the time-dependent fluctuations in the efficiency of the detector.

In fact, as the fluctuations in figure 5 are found to be constant with respect to the neutron energy, a scaling factor can be applied to the transmission spectra collected by the GEM detector so as to make them overlap to the ones collected by the GS20 monitor. Such self-consistent correction, of which we provide an example in the next section, provides an important tool to guarantee an accurate determination of neutron cross sections that, already in the old set-up of the instrument, corresponded to experimental error bars substantially lower than 1% [39, 40].

In order to improve the THGEM detector stability, a pressure and temperature sensor will be installed on VESUVIO. A correction of the gain variation will be provided by the study of the atmospheric fluctuations, as R. Akimoto et al. have described in [41].

4.4 γ-sensitivity

A desirable feature of neutron detectors is their capability to be insensitive to gamma radiations [42, 43]. On the VESUVIO beam line photons are emitted by the instrumentation components and by the environment after neutron capture. With the use of the THGEM detector, photons of 0.48 MeV are also emitted by the de-excitation of ^{7}Li. THGEM detector γ-discrimination has been studied making use of Cadmium (3 mm) and Tungsten (2 mm) filters installed upstream of the VESUVIO instrumentation at 5 m from the sample tank. This filter has the property (called *black resonance* [44]) to absorb neutrons up to 0.5 eV. In figure 6, two ToF spectra are reported. The left figure is the ToF spectrum without the presence of the filters. On the right, the graph shows the ToF spectra after the insertion of Cadmium and Tungsten filters. The region around 0.002 to 0.02 s corresponds to the black resonance. Assuming that in this region no counts due to neutrons are

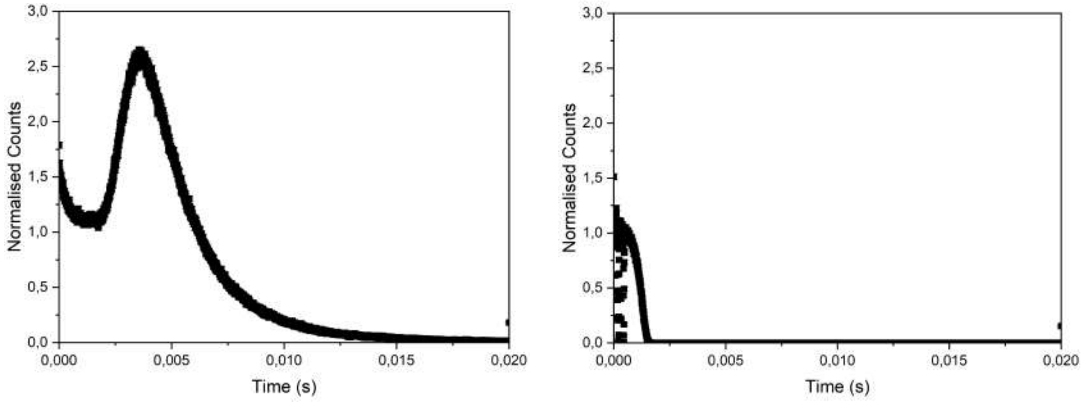

Figure 6. Left: time of Flight spectrum without filters. Right: time of Flight spectrum with Cadmium(Cd) and Tungsten(W) filters.

present, the counts in this region are provided by gamma-rays. The gamma sensitivity is defined as:

$$\gamma_{\text{sensitivity}} = \frac{\text{counts inside the resonance}}{\text{counts outside the resonance}}$$

where the considered intervals are 1710-1740 µs inside the black resonance and 500-530 µs outside the resonance.

The ratio between these two intervals provides the γ sensitivity, which is a value better than $7.6 \times 10^{-5} \gamma/n$.

4.5 Imaging capability

The detector imaging capability has been tested determining the VESUVIO beam profile and with the use of a Cadmium sample. Figure 7 shows the 2D beam profile of the VESUVIO beamline at the detector working point. The profile has been fitted with a bi-gaussian distribution obtaining a

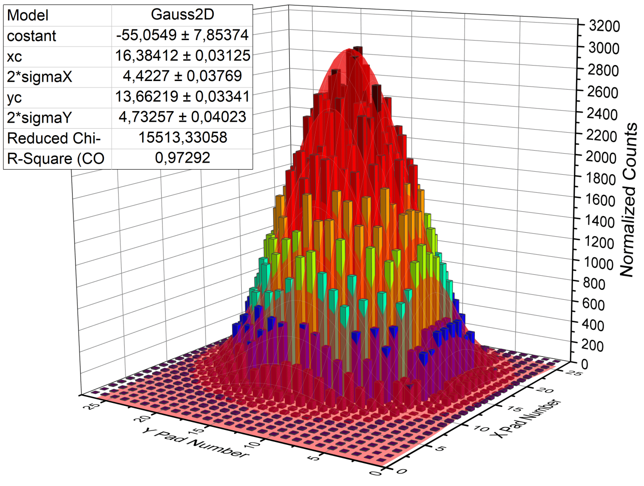

Model	Gauss2D
costant	-55,0549 ± 7,85374
xc	16,38412 ± 0,03125
2*sigmaX	4,4227 ± 0,03769
yc	13,66219 ± 0,03341
2*sigmaY	4,73257 ± 0,04023
Reduced Chi-	15513,33058
R-Square (CO	0,97292

Figure 7. VESUVIO 2D map and bi-gaussian fit.

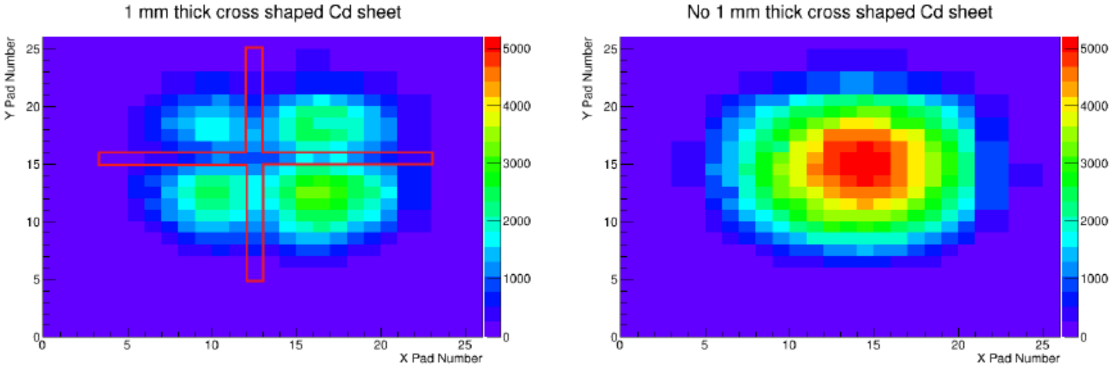

Figure 8. Left: 2D map of cadmium sample with a cross shape of 3 mm wide, 1 mm thick and 6 cm long. Right: 2D map of open beam.

FWHM$_x$=10.7 pads and a FWHM$_y$=10 pads, which correspond to $3 \times 3\,\text{cm}^2$. These values are in accordance with the expected VESUVIO beam profile width [35].

As a further investigation of the THGEM imaging capabilities, making use of a cadmium cross-shaped sample, the 2D sample map has been reproduced. The cadmium sample has a cross shape 3 mm wide, 1 mm thick and 6 cm long. As shown in figure 8, comparing the cadmium and the open beam 2D maps, the cross shape of the sample is quite visible. Inside the cross region the total counts are reduced by a factor of 3-4 compared with the open beam map.

The dimensions of the cross arms have been determined from the fit with gaussian distributions of the profiles along the X and Y axis. An FWHM$_x$ of 4.9 pads, which corresponds to a width of 1.5 cm, and FWHM$_y$ of 3.6 pads, which correspond to a width of 1 cm, have been measured.

A quantitative value, which provides an information about the detector capability to perform imaging, has been found making use of the figure of Merit (FOM):

$$\text{FOM} = \frac{\text{center peak 1 - center peak 2}}{\text{FWHM}_1 + \text{FWHM}_2} \tag{4.3}$$

If the FOM value is around 1, the two figures are distinguishable, whereas if it is around 0 they are overlapped. Figure 9 shows X and Y profile of the cadmium sample with cross shape, where the double peak is due to the absorption of the cadmium. The double peak has been fitted with two Gaussian distributions and FOM has been obtained from the equation (4.3) using the fit parameters.

The FOM values are 0.6 ± 0.1 for both profiles. The same procedure has been repeated for 3 X and Y profiles and the obtained values for the 6 profiles are 0.6 ± 0.1. As a result, the THGEM detector can distinguish two image which lay at least 3 mm apart.

At present, the largest component to the imaging performances is provided by the neutron beam divergence, rather than by the detector characteristics, and the former can be improved in the future using a tailored collimation set-up at the beginning of the instrument blockhouse.

5 Measurements of total neutron cross sections

As mentioned before, VESUVIO is a unique beam line at ISIS which provides transmission measurements over a broad neutron energy range in order to determine the total neutron cross section of

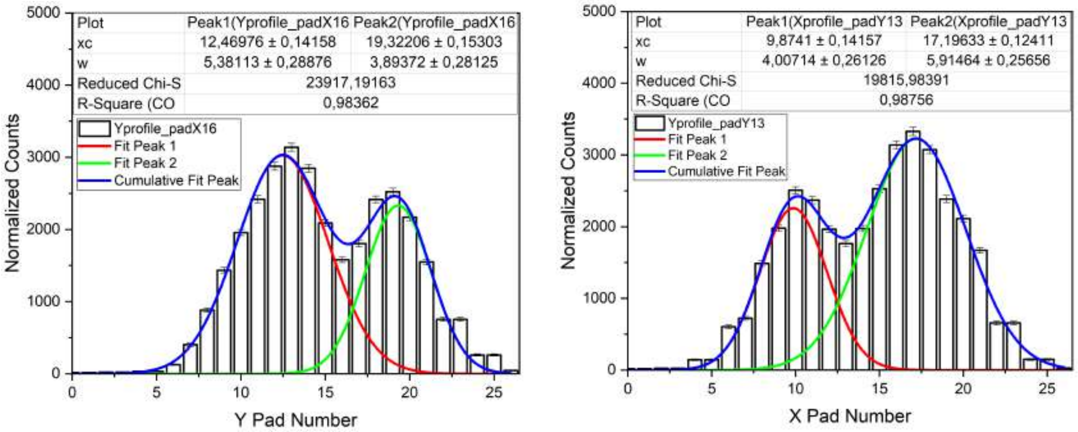

Figure 9. Left: Y profile of the cadmium sample with cross shape (figure 8) with pad X = 16 fixed. Right: X profile with Y = 13 fixed.

molecules, such as normal and deuterated alcohols [45]. As described by J.I. Robledo et al. [46], the neutron cross section from transmission measurements can be obtained by the Beer-Lambert Law:

$$I(E,x) = I_0\, e^{-n\sigma(E)x} \tag{5.1}$$

where $I(E,x)$ is the transmitted intensity through a sample of density n and thickness x, I_0 is the initial intensity and $\sigma(E)$ is the total neutron cross section. Naming the ratio $I(E,x)/I_0$ the transmission spectrum $T(E,x)$ and inverting the equation (5.1), the total neutron cross section is:

$$\sigma(E) = -\frac{\ln T(E,x)}{nx} \tag{5.2}$$

Making use of this procedure, the neutron total cross section in the energy range of thermal and epithermal neutrons of a Vanadium sample with 2 mm of thickness has been determined.

Figure 10 shows the neutron total cross section of the sample obtained from data of both transmission detectors. The two cross sections have the same trend and they are superimposed.

Making use of the THGEM detector, the cross section in the energy region around 10^{-3} eV can be explored. During spectroscopy experiments, which are normally performed at VESUVIO, this energy range provides useful information about the lattice and molecular dynamics of the sample. In this region, the GS20 detector is highly affected by the gamma-ray flash due to the proton bunch of Target Station 2 (TS2) and environmental background. Since the THGEM detector is less sensitive to gammas than the GS20 (as described in section 4.4), accurate cross section measurements are more feasible using the THGEM detector.

The THGEM detector also provides more detailed information (with respect to the GS20) about the cross section up to the keV energy range. Indeed in this energy region, the detection efficiency of the GS20 is significantly lower than THGEM detector, see paragraph 4.2. The higher efficiency of the GEM detector corresponds to markedly less scattered points in the spectrum. This is particularly evident for epithermal neutrons, where the total cross section is generally expected to be constant at the free-scattering value.

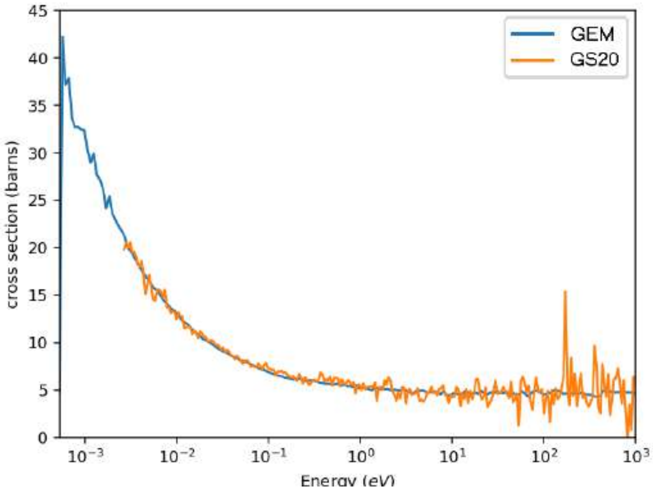

Figure 10. Vanadium neutron total cross section determined with the use of THGEM detector (blue line) and VESUVIO GS20 transmission monitor (orange line).

Therefore, the THGEM detector performs well in these experiments and provides more accurate measurements of neutron cross sections in the thermal and epithermal energy region in agreement with the VESUVIO GS20 transmission monitor.

6 Conclusions

The first double THGEM neutron detector has been successfully developed and tested. Results show the capability to detect thermal neutrons with an efficiency of 1%. The THGEM detector has a counting rate stability of 2%, which is a good stability value for a gas detector, and a capacity to discriminate gammas from neutrons on the order of magnitude of $10^{-5}\gamma/\mathrm{n}$. These results are the main goals achieved by the THGEM detector. An important feature of the THGEM detector analysed in this work is the possibility to do imaging. The VESUVIO beam profile and a cadmium sample dimensions have been determined and the imaging capability has been quantified with a FOM of 0.6. The THGEM detector on theVESUVIO instrument at ISIS has provided accurate measurements of the neutron total cross section of samples. For these reasons, the THGEM detector will be permanently installed at the ISIS-VESUVIO beamline and it will be accessible to future users to do transmission experiments.

Acknowledgments

This work was supported within the CNR-STFC agreement No. 01/9001 concerning collaboration in scientific research at the spallation neutron source, ISIS. The financial support of the Consiglio Nazionale delle Ricerche (CNR-Italy) is hereby acknowledged. We also received finical support from the National Key R&D Program of China (No. 2017YFA0403702), the National Natural Science Foundation of China (No. U1832119, 11635012 and 11775243), and Youth Innovation Promotion Association CAS, China. This work was also set up in collaboration with and with the financial support of INFN-group V.

References

[1] ISIS Neutron and Muon Source webpage, https://www.isis.stfc.ac.uk.

[2] J. Mayers and G Reiter, *The VESUVIO electron volt neutron spectrometer*, *Meas. Sci. Technol.* **23** (2012) 045902.

[3] GS20 scintillator webpage, https://www.scintacor.com.

[4] F. Sauli, *The gas electron multiplier (GEM): Operating principles and applications*, *Nucl. Instrum. Meth. A* **805** (2016) 2.

[5] L. Lavezzi et al., *The new Cylindrical GEM Inner Tracker of BESIII*, *Int. J. Mod. Phys. Conf.* **46** (2018) 1860077.

[6] J. Leidner et al., *3D energy deposition measurements with the GEMPix detector in a water phantom for hadron therapy*, 2018 *JINST* **13** P08009.

[7] A. Muraro et al., *Directionality properties of the nGEM detector of the CNESM diagnostic system for SPIDER*, *Nucl. Instrum. Meth. A* **916** (2019) 47.

[8] M. Alexeev et al., *The quest for a third generation of gaseous photon detectors for Cherenkov imaging counters*, *Nucl. Instrum. Meth. A* **610** (2009) 174.

[9] M. Alexeev et al., *THGEM based photon detector for Cherenkov imaging applications*, *Nucl. Instrum. Meth. A* **617** (2010) 396.

[10] M. Alexeev et al., *Micropattern gaseous photon detectors for Cherenkov imaging counters*, *Nucl. Instrum. Meth. A* **623** (2010) 129.

[11] F. Murtas et al., *Triple GEM gas detectors as real time fast neutron beam monitors for spallation neutron sources*, 2012 *JINST* **7** P07021.

[12] G. Croci et al., *nGEM fast neutron detectors for beam diagnostics*, *Nucl. Instrum. Meth. A* **720** (2013) 144.

[13] G. Croci et al., *Discharge probability measurement of a Triple GEM detector irradiated with neutrons*, *Nucl. Instrum. Meth. A* **712** (2013) 108.

[14] G. Croci et al., *GEM-based detectors for thermal and fast neutrons*, *Eur. Phys. J. Plus* **130** (2015) 61.

[15] G. Croci et al., *Diffraction measurements with a boron-based GEM neutron detector*, *EPL* **107** (2014) 12001.

[16] G. Croci et al., *Characterization of a thermal neutron beam monitor based on gas electron multiplier technology*, *Prog. Theor. Exp. Phys.* (2014) 083H01.

[17] G. Albani et al., *Evolution in boron-based GEM detectors for diffraction measurements: from planar to 3D converters*, *Meas. Sci. Technol.* **27** (2016) 115902.

[18] G. Croci et al., *A high efficiency thermal neutron detector based on thin 3D 10B4C converters for high rate applications*, *EPL* **123** (2018) 52001.

[19] G. Croci et al., *I-BAND-GEM: a new way for improving BAND-GEM efficiency to thermal and cold neutrons*, *Eur. Phys. J. Plus* **134** (2019) 166.

[20] F. Piscitelli and P. Van Esch, *Analytical modeling of thin film neutron converters and its application to thermal neutron gas detectors*, 2013 *JINST* **8** P04020 [`arXiv:1302.3153`].

[21] A.C. Basañez, K. Kanaki and F. Piscitelli, *DECal, a Python tool for the efficiency calculation of thermal neutron detectors based on thin-film converters*, `arXiv:1801.07124`.

[22] C. Höglund et al.,*B_4C thin films for neutron detection*, J. Appl. Phys. **111** (2012) 104908.

[23] C. Höglund et al.,*Stability of $^{10}B_4C$ thin films under neutron radiation*, Radiat. Phys. Chem. **113** (2015) 14.

[24] S. Schmidt et al., *Low-temperature growth of boron carbide coatings by direct current magnetron sputtering and high-power impulse magnetron sputtering*, J. Mater. Sci. **51** (2016) 10418.

[25] G. Croci et al., *Characterization of a thermal neutron beam monitor based on gas electron multiplier technology*, Prog. Theor. Exp. Phys. **2014** (2014) 083H01.

[26] F. Piscitelli et al., *Study of a high spatial resolution ^{10}B-based thermal neutron detector for application in neutron reflectometry: the Multi-Blade prototype*, 2014 *JINST* **9** P03007 [`arXiv:1312.2473`].

[27] China Spallation Neutron Source webpage, http://english.ihep.cas.cn/csns.

[28] Z. Hu et al., *Interpretation of effective gain variations with the drift electric field for a ceramic thick gas electron multiplier*, Nucl. Instrum. Meth. A **988** (2021) 164907.

[29] J. Yan, et al., *Simulation and performance study of ceramic THGEM*, Chin. Phys. C **6** (2015) 066001.

[30] J. Zhou et al., *A novel ceramic GEM used for neutron detection*, Nucl. Eng. Technol. A **962** (2019) 163593.

[31] Nuclear Instrument webpage, http://www.nuclearinstruments.eu.

[32] W. Bonivento et al., *Development of the CARIOCA front-end chip for the LHCb muon detector*, Nucl. Instrum. Meth. A **491** (2002) 233.

[33] L. Mangiagalli et al., *Characterization of GEMINI, a 16-channels programmable readout interface for Triple-GEM detectors in 180nm CMOS*, `PoS(TWEPP2018)165`.

[34] A. Muraro et al., *Development and characterization of a new soft x-ray diagnostic conceptfor tokamaks*, 2019 *JINST* **12** C08012.

[35] G. Romanelli et al., *Characterisation of the incident beam and current diffraction capabilities on the VESUVIO spectrometer*, Meas. Sci. Technol. **28** (2017) 095501.

[36] A. Muraro, *GEM based detectors for fast and thermal neutrons*, Ph.D. thesis, Università degli Studi di Milano-Bicocca, Milano, Italy (2018).

[37] A. Muraro et al., *Performance of the high efficiency thermal neutron BAND-GEM 2 detector*, Prog. Theor. Exp. Fis. **2018** (2018) 023H01.

[38] G. Croci et al., *GEM-based thermal neutron beam monitors for spallation sources*, Nucl. Instrum. Meth. A **732** (2013) 217.

[39] S. C. Capelli and G. Romanelli, *An effective hydrogen scattering cross section for time-of-flight neutron experiments with simple organic molecules*, J. Appl. Cryst. **52** (2019) 1233.

[40] J. I. Marquez Damian at al., *Experimental validation of the temperature behavior of the ENDF/B-VIII.0 thermal scattering kernel for light water*, EPJ Web Conf. **239** (2020) 3.

[41] R. Akimoto et al., *Measurement of basic features of Thick-GEM and Resistive-GEM*, 2010 *JINST* **5** P03002.

[42] G. Croci et al., *Measurements of γ-ray sensitivity of a GEM based detector using a coincidence technique*, 2013 *JINST* **8** P04006.

[43] A. Khaplanov et al. *Investigation of gamma-ray sensitivity of neutron detectors based on thin converter films*, 2013 *JINST* **8** P10025.

[44] G. Leinweber et al., *Cadmium resonance parameters from neutron capture and transmission measurements at the RPI LINAC*, in the proceedings of the 13th *International Topical Meeting on the Nuclear Applications of Accelerators (AccApp17)*, July 13–August 4, Quebec City, Canada (2018).

[45] L.A. Rodríguez Palomino et al., *Neutron total cross-section of hydrogenous and deuterated 1- and 2-propanol and n-butanol measured using the VESUVIO spectrometer*, *Nucl. Instrum. Meth. A* **870** (2017) 84.

[46] J.I. Robledo et al., *Measurement of neutron total cross sections at the VESUVIO spectrometer*, *Nucl. Instrum. Meth. A* **971** (2020) 164096.

Eur. Phys. J. Plus (2021) 136:742
https://doi.org/10.1140/epjp/s13360-021-01707-2

THE EUROPEAN
PHYSICAL JOURNAL PLUS

Regular Article

MBGEM: a stack of borated GEM detector for high efficiency thermal neutron detection

A. Muraro[5,6,10], **G. Claps**[1,4], **G. Croci**[5,6,10], **C. C. Lai**[3,8], **R. De Oliveira**[2], **S. Altieri**[7], **S. Cancelli**[5,6], **G. Gorini**[5,6,10], **R. Hall-Wilton**[6,8], **C. Höglund**[8,9], **E. Perelli Cippo**[5], **L. Robinson**[8], **P. Svensson**[8], **F. Murtas**[1,2,a]

[1] Laboratori Nazionali di Frascati-INFN, Frascati, Italy
[2] CERN, 1211 Geneva, Switzerland
[3] Linköping University, Linköping, Sweden
[4] Centro Ricerche Frascati (ENEA), Frascati, Italy
[5] Istituto per la Scienza e Tecnologia dei Plasmi (ISTP) (CNR), Milan, Italy
[6] Dipartimento di Fisica "G. Occhialini", Università degli Studi di Milano - Bicocca, Milan, Italy
[7] Dip. di Fisica and INFN, Università degli Studi di Pavia, Pavia, Italy
[8] Detector Group, European Spallation Source ERIC (ESS), Lund, Sweden
[9] Impact Coatings AB, Linköping, Sweden
[10] INFN, Sezione di Milano - Bicocca, Milan, Italy

Received: 30 March 2021 / Accepted: 24 June 2021

Abstract A new position-sensitive thermal neutron detector based on boron-coated converters has been developed as an alternative to today's standard ^{3}He-based technology for application to thermal neutron scattering. The key elements of the development are the boron-coated GEM foils (Sauli in Nucl Instrum Methods Phys Res Sect A Accel Spectrom Detect Assoc Equip 386:531, 1997) that are used as a multi-layer neutron converter via the $^{10}B(n, \alpha)^7Li$ reaction together with an efficient collection of the produced secondary electrons. This paper reports the test performed on a 3 layers converter prototype coupled to a GEMPix detector (Murtas in Radiat Meas 138:106421, 2020), carried out in order to study the possibility to produce a large-scale multi-layer neutron detector capable to reach high detection efficiency with high spatial resolution and able to sustain the high neutron flux expected in the new neutron spallation source under development like the ESS.

1 Introduction

The recent ^{3}He shortage [3], which is due to a progressive nuclear disarmament started in 2000, has resulted in reduced availability of this noble gas and a consequent high increase in its price. Nowadays the world's most important suppliers (USA and Russia) are keeping the residual amount of ^{3}He mainly for homeland security and nuclear safeguards applications. As a consequence, the availability of ^{3}He gas for thermal neutron detectors (in the form of high-pressure single-wire proportional counter tubes) has been severely reduced. On the other hand, the scientific community is experiencing the need to realize new large area position-sensitive devices able to fully exploit the increase of neutron flux offered by new spallation

---

[a] e-mail: fabrizio.murtas@cern.ch (corresponding author)

neutron sources like ESS. These two reasons led to the development of new position-sensitive neutron detectors capable of detection efficiencies comparable with ^{3}He tubes, but being able to sustain much higher counting rates than the 30–50 kHz typical for single ^{3}He tubes [4]. A possible approach relies on the use of solid neutron converters (such as boron or lithium) combined to charged particle detectors, like the gas electron multiplier (GEM) [1] detector. GEM detectors are typically used for tracking and triggering application in high energy physics [5], but they can also be used for neutral particles detection like fast [6–9] and thermal [10–14] neutrons or photon [15,16]. Neutral particles detection with GEM is typically performed by adopting a customized cathode configuration, where primary electrons are liberated in the detector gas due to neutrals interactions, followed by an amplification stage (composed by one or multiple GEM foils). Finally, the motion of the multiplied electrons in the induction region induces a signal on an anode (that can be fully customized for the specific application) read out by a dedicated data acquisition system (DAQ). This paper describes the development, the construction and the characterization of a new GEM-based thermal neutron detector called MBGEM (multi-boron GEM), equipped with a converter cathode made of a series of GEM foils coated on both sides with a layer (1 µm thick) of ^{10}B$_4$C. The paper is addressed to study the response of the new converter configuration in view of the production of a large area, high efficiency thermal neutron detector.

2 The MBGEM principle

The efficiency (ϵ) of a thermal neutron detector based on a solid-state converter (such as ^{10}B or ^{6}Li) combined to a charged particle amplifier can be defined as the result of the product of three factors:

- the neutron interaction probability (p),
- the escape probability (ξ) of the charged products generated by the neutron nuclear reaction
- the extraction efficiency (η) of the primary charge liberated by the reaction products.

In case of boron-based converters the nuclear reaction $^{10}\mathrm{B}(n,\alpha)^7\mathrm{Li}$ is exploited whose cross section is about 3844 b for 25 meV neutrons. This reaction is characterized by two main channels:

$$
\begin{aligned}
&^{10}\mathrm{B} + n \rightarrow Li + \alpha \ (Q\mathrm{Value} = 2.792\,\mathrm{MeV, ground\ state}); \mathrm{Branching\ Ratio} = 6\% \\
&^{10}\mathrm{B} + n \rightarrow 7Li^{\star} + \alpha \\
&\quad + \gamma(0.478\,\mathrm{MeV})\ (Q\mathrm{Value} = 2.310\,\mathrm{MeV, excited\ state}); \mathrm{Branching\ Ratio} = 94\%.
\end{aligned}
$$

Therefore when thermal neutrons interact with boron, the reaction leads to ^{7}Li in the excited state 94% of the times, while the remaining 6% are ground state ^{7}Li. Conservation of energy and momentum gives $E_{\mathrm{Li}} = 0.84$ MeV and $E_\alpha = 1.47$ MeV for the excited state reaction, and $E_{\mathrm{Li}} = 1.16$ MeV, $E_\alpha = 1.78$ MeV for the ground state reaction, and implies that the two charged particles (^{7}Li and α) are emitted back to back. It means that at least one of the (charged) reaction products is likely to be revealed into the adjacent detector. In addition when ^{7}Li is left in the excited state, there is always an emission of 478 keV γ ray.

The challenge in the design of novel detectors relies on finding a geometrical and electrical configuration able to simultaneously optimize p, ξ and η parameters. The probability p is related to the macroscopic neutron (absorption) cross section of the converter material used (^{10}B$_4$C in the case of this paper), while ξ is related to the range of the produced charge particles in the converter layer itself. Probability p can be increased by using a thicker converter layer, but this decreases the probability that the nuclear charged products can reach the gas. The α and ^{7}Li ions are emitted isotropically along the $^{10}B_4C$ layer thickness and one or other of these particles may leave the $^{10}B_4C$ layer and ionize the gas volume in which the converter is positioned. Therefore the charge escape probability ξ depends on:

- the neutron interaction point along the thickness of the $^{10}B_4C$ layer;
- the direction of emission of the charged particles;
- the $^{10}B_4C$ layer thickness.

The charged particles escaping from the layer will feature a continuous energy spectrum ranging from 0 to E_α and E_{Li}. The typical range of alpha and lithium ions in $^{10}B_4C$ is about 3.4 µm and 1.7 µm, respectively [17]. Therefore a single converter thicker than 2 µm will imply a large loss of detection efficiency (mainly for the L_i ions) due to ξ reduction. A possible approach to maximize the detection efficiency is the use of multiple stacked thin converter layers that must be able to be transparent to the secondary electrons produced by the gas ionization due to alpha and lithium ions, thus assuring a high extraction probability η. A converter thickness of 1 µm of $^{10}B_4C$ it seems the final good solution as reported also in other works based on a calculated optimization of neutron detection efficiency [18].

2.1 The preparation of the GEM foil

The key element of the present study is the double-face $^{10}B_4C$-coated GEM foil (called BGEM borated GEM) used to detect neutrons via the $^{10}B(n, \alpha)^{7}Li$ reaction. A GEM [19] is made of a thin (50 µm) Kapton foil, copper clad (5 µm thick) on each side, perforated with high surface density of holes, each one acting as an electron multiplication channel. Each hole has a bi-conical structure with an external (internal) diameter of 70 µm (50 µm) and a pitch of 140 µm. The bi-conical shape of the hole minimizes the effect of charging-up of the Kapton inside the holes and is a consequence of the double-mask process used in standard photolithographic technologies. A typical voltage difference of 250–500 V is applied between the two copper sides, giving fields as high as 150 kV/cm into the holes, resulting in an electron multiplication up to a few thousands.

The BGEM foil is produced by introducing a modification to the standard GEM production method. The base material is the usual 50 µm-thick polyimide foil cladded on both sides with copper (5 µm). The standard pattern of holes with a diameter of 70 µm and a pitch of 140 µm have been designed on a square of $30 \times 30\,\mathrm{mm}^2$ both on top and bottom sides of the foil, followed by a photoresist lamination on both faces. Then photoresist dots have been put covering precisely the copper openings followed by the curing. Afterward these foils were individually sandwiched in Milano Bicocca University with two Al masks that have a $30 \times 30\,\mathrm{mm}^2$ opening on each face aligned with the patterned active areas on both side of the foil as shown in Fig. 1.

2.2 The boron carbide deposition

The deposition process for coating-enriched amorphous boron carbide $^{10}B_4C$ layers on the polyimide foils was carried out since 2015 by ESS Linköping Detector Coatings Workshop, located at Linköping, Sweden. In the following ^{10}B enrichment means $> 95\%$. The facility is installed with an industrial deposition unit (CC800/9, CemeCon AG) equipped with four direct-current magnetron sputtering cathodes and a sample loading system for batch production. Details about the deposition unit and process development for neutron detector coatings of other types have been published elsewhere [17,20].

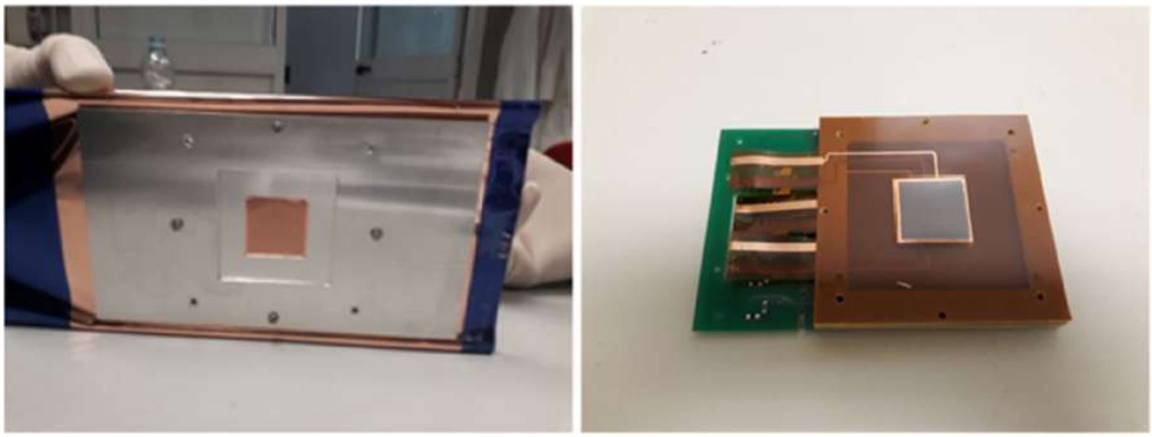

Fig. 1 On the left the GEMPix foil prepared with the aluminum mask before the boron deposition. On the right the final assembling of the multi-layer neutron converter with the electrode detail

The masks realized in Milan ensure good thermal and electrical contact over the surface of the foils to the grounded sample table of the deposition machine, so the foils have less chance to be thermally or electrically damaged during the deposition process. No other treatment, e.g., cleaning, was done to the masked samples prior to the loading of the samples to avoid damages to the photoresist dots.

The deposition chamber was first pumped down to a background pressure of $\sim 1.5 \times 10^{-4}$ Pa, while the samples were heated up to $\sim 100\,^{\circ}$C. Then the surfaces of the samples were treated with radiofrequency plasma etching in pure Ar atmosphere at 0.35 Pa to remove native oxides built up on the Cu surface and to create higher surface roughness for better film adhesion. After the etching, the samples were subsequently coated with a $^{10}B_4C$ layer in pure Ar at ~ 0.40 Pa and with a Cu capping layer in pure Ar at ~ 0.30 Pa without breaking the vacuum.

The selection of the working pressure for the $^{10}B_4C$ layer is mainly a compromise between the residual compressive stress and the increased oxygen content due to a relatively low-temperature process, which has been systematically studied on Si substrates [21]. A simple scratch test has been carried out with tweezers on non-active areas of coated foils, while only the surface of the Cu capping layers can be scratched off due to its softness. No spontaneous spall-off of the $^{10}B_4C$ films was observed either throughout the GEM foils production. The thickness of the coatings was measured with a profilometer (DektakXT, Bruker) on a Si(100) thickness reference mounted at an equivalent position of the deposition chamber in the same deposition run. The overall thickness of the $^{10}B_4C$ plus Cu layer was measured to be $\sim 4.0\,\mu$m on a Si(100) thickness. The individual thickness of the $^{10}B_4C$ layer and the Cu layer was calculated to be $\sim 1.0\,\mu$m and $\sim 3.0\,\mu$m, respectively, according to the deposition rates determined from single material depositions done with the same deposition parameters beforehand. The chemical composition of the $^{10}B_4C$ layer was done by elastic recoil detection analysis in the Tandem Laboratory in Uppsala University, while details on the employed detector set-up can be found in [22] and a discussion of the method and statistical and systematic uncertainties in [23,24]. The measurement was carried out on the same Si reference of the deposition rate determination to avoid the thick Cu capping layer on the samples. The result shows a relative atomic ratio of about 77%B, 18%C, and 5% impurities (mainly O and H).

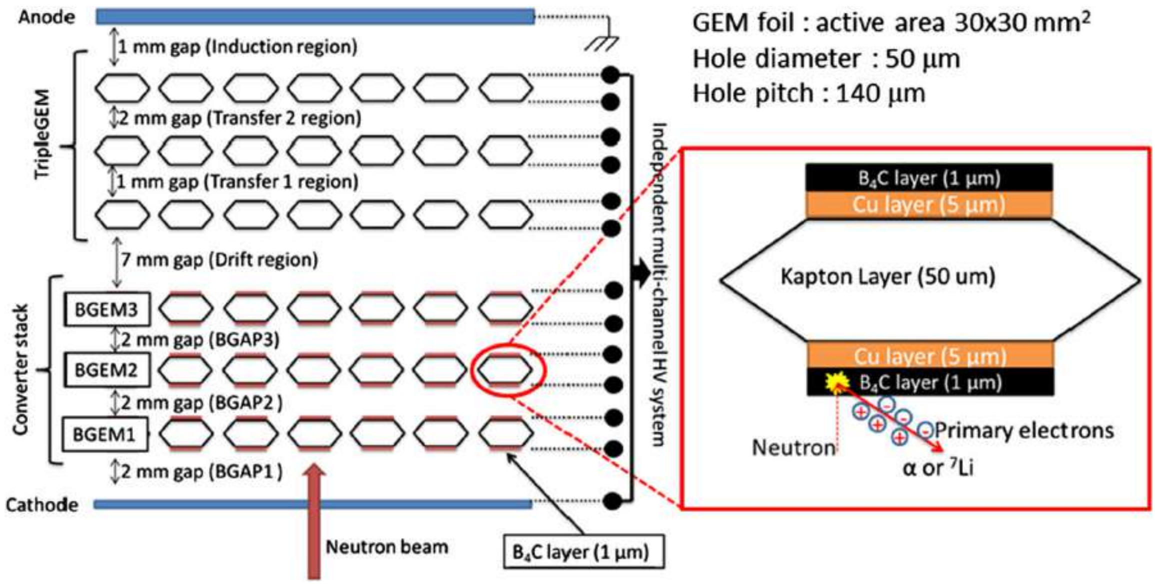

Fig. 2 Schematics of the multi-boron detector. Three BGEM borated GEM foils are stacked and used as neutron converter. Neutron beam impinges orthogonally on the converter and interacts with ^{10}B via the $^{10}\mathrm{B}(n, \alpha)^7\mathrm{Li}$ reaction. One of the two charged products is able to leave the $^{10}\mathrm{B}_4\mathrm{C}$ layer and ionize the gas in which the converter is placed (sketched in the zoomed detail on the right). Electrons liberated by this ionization are able to drift along the converter and reach the triple GEM structure where they are multiplied in order to induce a signal on the pixelated anode constituted by a quad-Timepix chip

2.3 The final BGEM production

After the boron deposition, the GEMPix foils came back to CERN for final working and etching. The photoresist dots were stripped by the foils with the aim to etch the polyimide, masked at this point by the boron deposition. After this procedure for the creation of the holes, the foils appear to have on both faces the usual GEM pattern in the central area and copper cladded on the remaining surface. The external copper is then etched to create the electrodes for the voltage application as shown in Fig. 1. The cleaning and the final electrical test ends the operations on the coated foils, to be ready for the detector assembly. All the six BGEMs produced passed the electrical test, and three of them were used for the detector construction.

2.4 The detector construction

Three GEMPix foils with different electrodes configuration useful for the final HV distribution (see Fig. 1) have been assembled. The gluing of these foils on FR4 frames and the final assembling of the multi-layer neutron converter were performed in a clean room of Laboratori Nazionali di Frascati of INFN.

The multi-boron GEMPix detector is schematically represented in Fig. 2.

The detector has a neutron converter region, composed by a PCB with gold-plated 30 × 30 mm^2 cathode followed by a stack of 3 BGEM foils. Each electrode of the 3 GEM foils is connected to an independent channel of the HV system [25], so that the electric fields and gain can be set individually on each GEM foil. Neutrons enter in the detector orthogonally to the cathode. They can be absorbed in one of the six 1 μm thick $^{10}\mathrm{B}_4\mathrm{C}$ layers of the converter stack (two $^{10}\mathrm{B}_4\mathrm{C}$ layers for each BGEM foil) via the $^{10}\mathrm{B}(n, \alpha)^7\mathrm{Li}$ reaction. The two created charged particles are emitted back to back (momentum conservation), so only one of them can escape from the $^{10}\mathrm{B}_4\mathrm{C}$ layer and ionize the detector gas (a mixture of Ar CO$_2$ CF$_4$ 45/15/40), producing the secondary electrons that will be driven by the applied electric field toward to the holes of the GEM foils, where they are transported and eventually multiplied subjected to the high electric field dipole present in the hole. The HV configuration of the detector must ensure a uniform response independently from the neutron interaction point in the converter stack. The gain of the BGEM composing the converter stack must be close to one, so that the charge will be transfer from one conversion region to another without multiplication.

The ionization charge produced by the multi-boron converter by the single particle is then drifted toward the triple GEM amplifier where will be finally multiplied by a factor 10^2–10^4 depending of the applied voltage generated by the HVGEM module [26]. Below the triple GEM structure at 1 mm distance a pixelated readout is organized using a matrix of 2×2 'naked' Timepix ASICs [27] with an active area of the detector equal to $3 \times 3\,\mathrm{cm}^2$. The movement of the charge in the induction region induces a signal on a group of pads of the Timepix ASIC (dimension of each pad is $55 \times 55\,\mu\mathrm{m}^2$), underlying the so-called charge cluster.

The Timepix ASICs are operated in Time-over-Threshold (ToT) mode and read out by the FITPix [28] (an FPGA-based module) using the Pixelman software [29]. In ToT mode, the Timepix measures the time spent above a fixed threshold by the analogue signal induced on the single pixel, which is proportional to the collected charge and then (after calibration) to the energy deposited in the detector by the radiation. The measurement of the deposited charge (call event) is done for an adjustable time window, here called "exposure time." For the scope of this study, the exposure time must be set with the goal to obtain a limited number of well-separated charge clusters in each event, so that the response to each single interacting particle can be studied. An online cluster analysis algorithm is used in order to produce a file output with the list of the reconstructed charge clusters, reporting for each one the main information such as the start time of the event, the total number of detected clusters, the total charge and some other geometric parameters.

3 Detector characterization

The detector was characterized under X-ray and gamma irradiation at the CERN and under neutron irradiation at the LENA reactor in Pavia [30].

3.1 Optimization of the converter charge extraction efficiency

As highlighted in par. 2, the fundamental parameter of the MBGEM detector is the capability to extract the primary charge created by the incoming radiation from the converter stack. Ideally, the response of the detector should be the same independently from the neutron interaction point in the converter.

Thanks to the independent HV control applied to each BGEM, it is possible to experimentally tune the gain of the BGEMs in order to obtain a uniform response. This optimization was done by irradiating with a ^{55}Fe radioactive source each single gas gap (Bgap) between BGEM foils through small apertures on the frames side. In this way X-rays impinge laterally on the detector and get collimated by the small frame aperture (see Fig. 3).

Figure 4 shows a typical charge spectrum recorded when X-rays convert only in the drift region. As expected, both the main peak (5.9 keV) and the escape peak (3 keV) are clearly visible. Since the X-rays enter the detector in the drift region (i.e., between the triple GEM and the converter) electrons produced in this region by X-rays ionization move toward the triple GEM amplifier. The peak position shown in Fig. 4 is related only to primary ionization

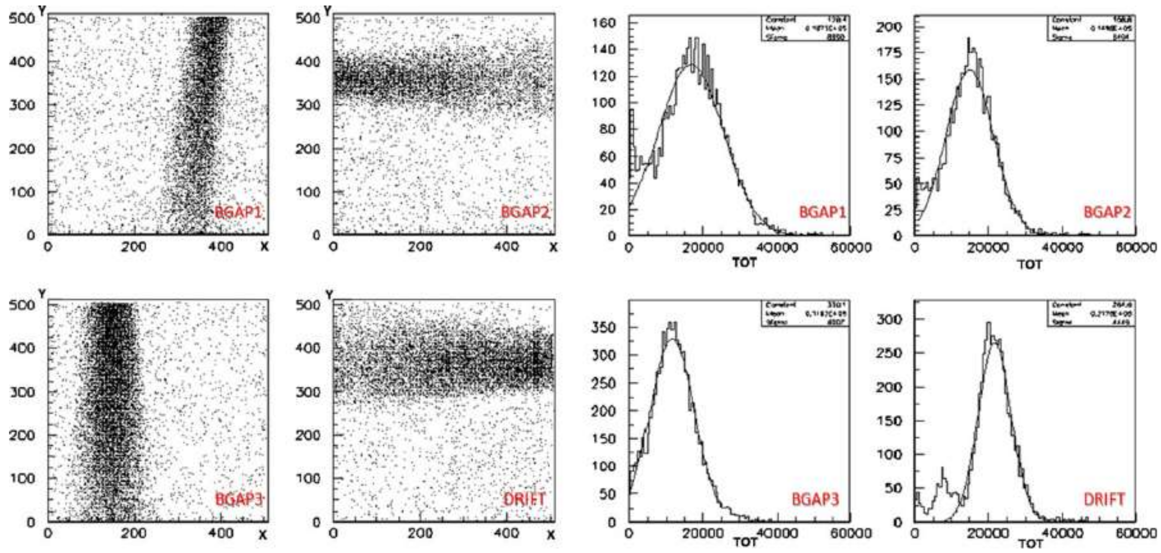

Fig. 3 On the left the 2D images of the X-ray flux entering in the different gap of the multi-boron converter. On the right the spectrum of the ^{55}Fe measured for each gap

Fig. 4 Reference charge deposited spectrum recorded when the detector is irradiated in the induction layer

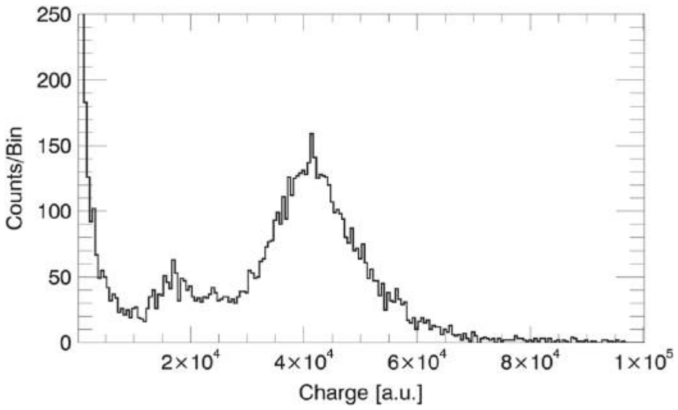

in the drift region and to triple GEM amplification. Therefore a change in the voltage applied to the converter will not affect the peak position.

The source was then moved around in order to irradiate regions between each BGEM one by one. This study allows to disentangle each single BGEM contribution. Each BGEM voltage is then tuned so that the position of main peak position obtained when the detector irradiated in the corresponding Bgap is comparable to the position obtained when X-rays convert only in the drift region. Figure 5 shows the recorded spectra obtained when the detector is irradiated in the different Bgaps with two different HV configuration (300 V and 330 V applied on each BGEM).

Each spectrum is fitted with a Gaussian to obtain the peak position P_{Bgap_i}. The BGEMs potential differences are then tuned so that the charge extraction factor C_{ex_i} is equal to one for each irradiated Bgap volume:

$$C_{\mathrm{ex}_i} = \frac{P_{\mathrm{Bgap}_i}}{P_{(\text{drift region})}} \approx 1. \tag{1}$$

Figure 6 shows the obtained coefficient values for the two HV configurations. The error bars represent the calculated FWHM of the fitted Gaussian.

The left panel shows that with a too low BGEM gain a significant fraction of the deposited charge is lost when the electrons have to transfer from one converter volume to the subsequent.

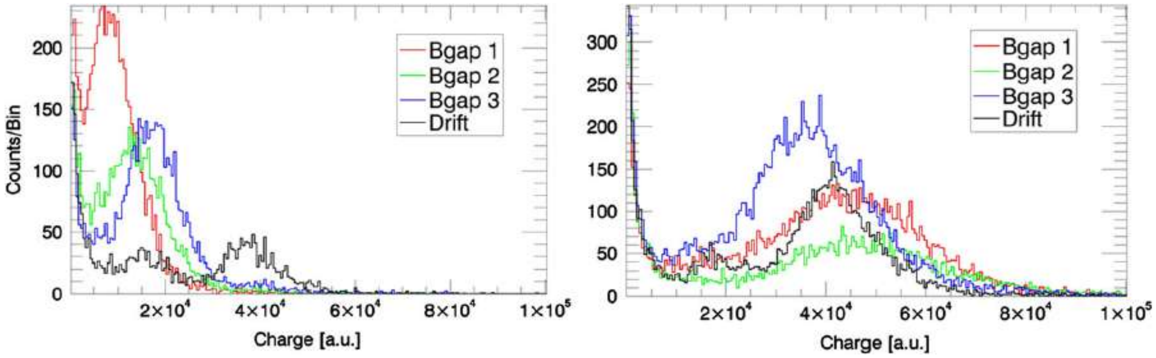

Fig. 5 Deposited charge spectrum recorded with the detector irradiated in the Bgap1 (red), Bgap2 (green), Bgap3 (blue) and drift region (black) with BGEM$_i$ voltage = 300 V (left panel) and 330 V (right panel) applied on each BGEM

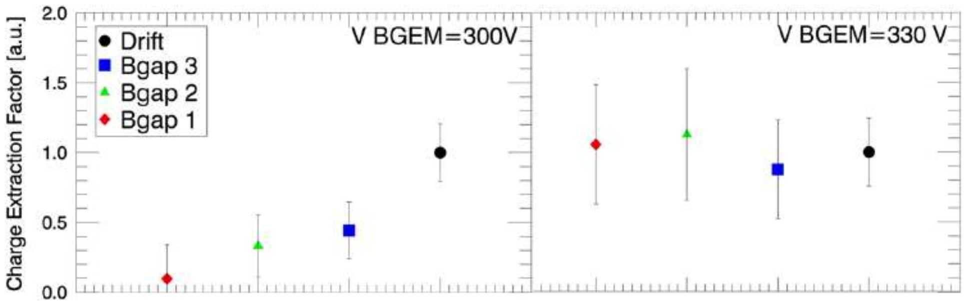

Fig. 6 Charge extraction factor for each i_{th} irradiated volume of the converter obtained with 300 V (left panel) and 330 V (right panel) applied on each BGEM. The error bars represent the calculated FWHM

With the appropriate gain instead (right panel), the deposited charge is successfully transferred from one converter volume to another. Figure 6 shows also a degradation of the energy resolution (represented by the error bars) by increasing the distance of the irradiation point from the drift region. This is maybe due to the fact that a fraction of the created primary electrons is lost on the bottom electrode of each BGEM, but the average deposited charge (center position of the main peak) does not change because the lost electron fraction is replaced by the multiplication of the primary electrons that are able to enter in the BGEMs holes. The energy resolution degradation can be contained by acting on the transfer electric field present between two BGEM, and this optimization will be studied in the future. However, for counting application the energy resolution is not a crucial parameter, and the degradation shown by the 3 BGEM converter with the optimal found HV configuration suggests that the charge will be successfully transfer also in a converter with more than 3 BGEMs, giving the possibility to further increase the thermal neutron efficiency of the detector. The following γ-ray and neutron characterization was done with the converter HV configuration found in this study.

3.2 Gamma ray characterization of the detector

Gamma ray sensitivity is a crucial parameter for neutron detectors, given that they operate in an environment on which a gamma background due to neutron-induced reaction is always present. In a GEM detector gammas interact with the detector material mainly through Compton effect, producing a Compton electron that can give rise to a signal in the readout anode. Compton electrons travelling in the gas medium have a reduced stopping power producing elongated thin tracks typically with a low charge density. On the other hands, the ions pro-

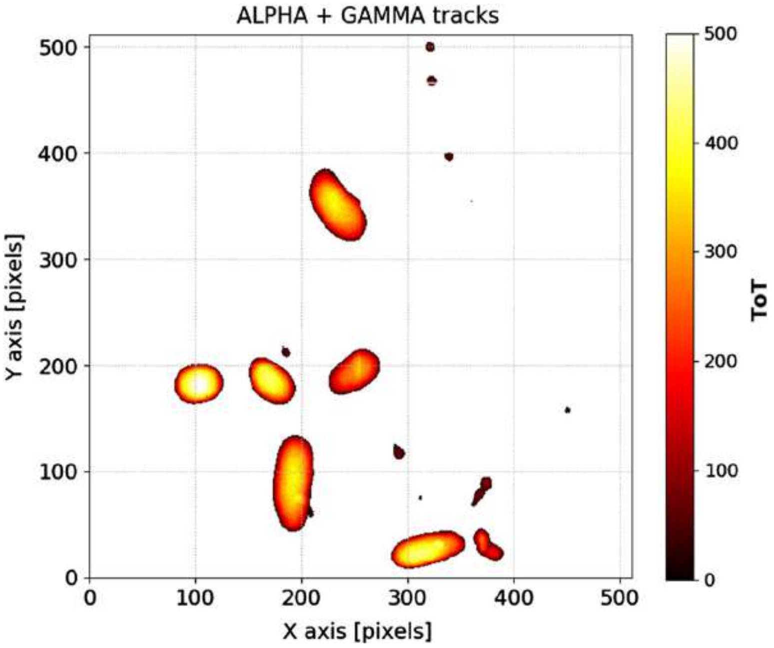

Fig. 7 The online display (512 × 512 pixels $\simeq 3 \times 3$ cm^2) showing six alphas produced by the thermal neutrons reaction and the small clusters produced by gammas (Compton electrons). The width of the clusters is clearly different between alphas and electrons

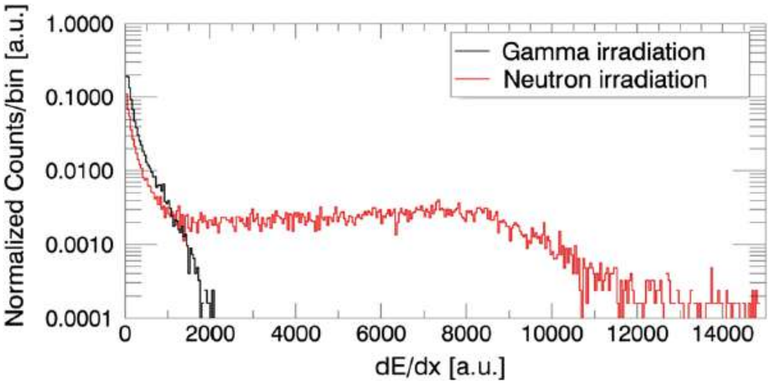

Fig. 8 Distribution of the dE/dx factor recorded with the detector under gammas (black line) and neutron (red line) irradiation with HVGem = 1240 V

duced by the ^{10}B$(n, \alpha)^7$Li reaction have high stopping power in the gas medium, producing circular or elliptical tracks since they have a high charge density. Figure 7 shows an example of the recorded tracks for gammas and neutrons by the online display.

The different stopping power (dE/dx) of the particles interacting with the detector gives a useful tool to perform an effective neutron/gamma discrimination. In fact, for each interacting particle the readout electronic gives both the total deposited charge and width of the produced track. The ratio between these two quantities gives an estimation of the stopping power. Figure 8 shows an example of the distributions of the dE/dx factor obtained with the detector, respectively, under gammas (black line) and neutron (red line) irradiation.

Gamma sensitivity is strictly related to the detector gain, since the lower the gain, the less is the probability that a gamma will produce a trace capable of giving a signal over the threshold on the reading electronics. At the same time, at low gain even the charge produced by ions is lower, affecting the neutron detection efficiency of the detector. It is then crucial to determine a working point for the detector that maximizes the neutron detection efficiency minimizing

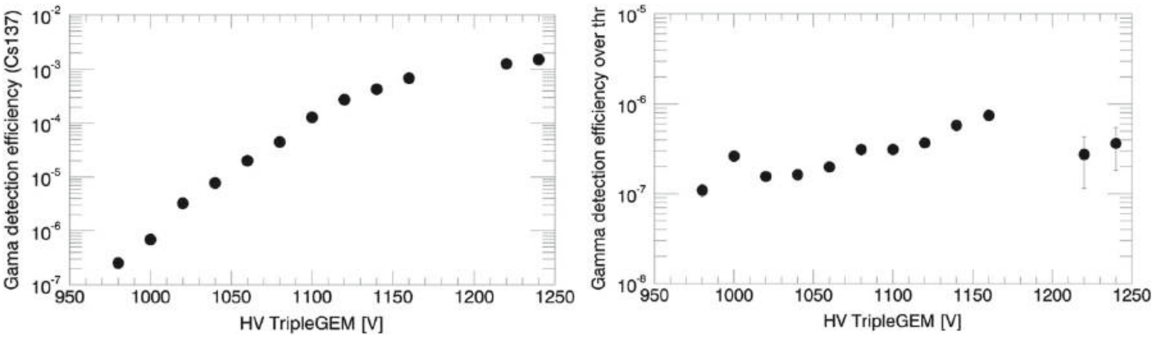

Fig. 9 Detection efficiency obtained for different detector gain under ^{137}Cs γ-rays irradiation. On the left: no dE/dx threshold applied. On the right: applying the set of dE/dx thresholds

the gamma sensitivity. In order to do this, the detector was tested for different gains (applied to the triple GEM detector stage) using a ^{137}Cs source (662 keV photon energy). The gamma efficiency is determined by dividing the total number of recorded events (no threshold applied) with the estimated total flux of photons on the detector. The result of the scan is shown in Fig. 9.

As expected, the gamma sensitivity is an increasing function of the gain, but it is possible to determinate a set of dE/dx thresholds (one threshold for each gain) so that the gamma sensitivity can be below a fixed value even for high gain. By applying the found set of dE/dx threshold the gamma sensitivity obtained as a function of the gain is reported in Fig. 9.

The gamma detection efficiency obtained is less than 10^{-6} with the chosen set of threshold, allowing neutron measurements with a n/γ discrimination factor better than 10^5 assuming a neutron detection efficiency of about 10^{-1}. The results shown in this paragraph highlight also that the detector performance is not influenced by the 478 keV γ-rays emitted during the ^{10}B$(n, \alpha)^7$Li when the ^{7}Li is left in the excited state since we expect a similar gamma sensitivity for γ-rays of this energy.

3.3 Neutron characterization of the detector

The detector was tested at the research nuclear reactor of Applied Nuclear Energy Laboratory (LENA) [30] of Pavia University, a 250-kW power Triga Mark II that offers different neutron irradiation positions; recently in one of the horizontal channels has been realized a collimated thermal neutron beam with a diameter of 49 mm and equipped with a system of shutters that allows the positioning of samples even when the reactor is in operation. The thermal flux at the exit of the channel is about 5×10^6 cm^{-2} s^{-1}.

The neutron beam was collimated using a ^{6}Li-enriched plastic sheet having a hole (5 mm diameter) in the middle. The first test performed was a gain scan in order to determine the detector working point to be used for neutron detection (the minimum gain at which the neutron detection efficiency is maximized). In order to do this study, the same set of threshold found in the gamma scan of par. 3.2 was used. The result of the scan is shown in Fig. 10.

The recorded counting rate is an increasing function of the gain, showing a plateau for HV $\approx$ 1120 V, which represent the working point of the detector under neutron irradiation.

The neutron detection capability was measured as a function of the number of active converter layers in the detector. The BGEMs were initially set to 0 V (no charge transfer between different converter volumes), and the relative detection efficiency was measured by setting to 330 V each BGEM one by one. The relative detection efficiency is calculated as the ratio between the counting rate recorded with all the BGEM set to 0 V (with a single active

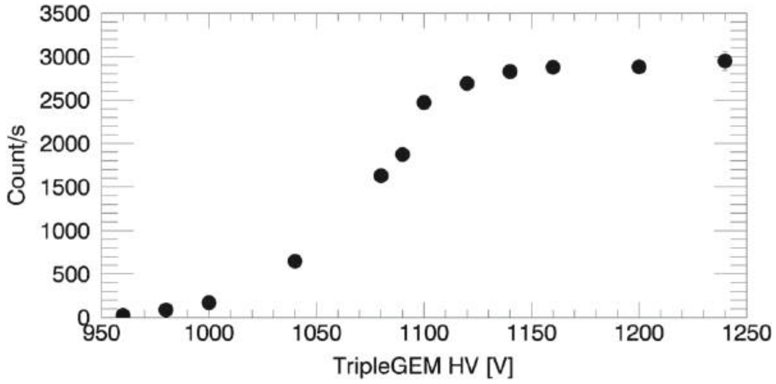

Fig. 10 Recorded over threshold counting rate as a function of the detector gain under thermal neutron irradiation

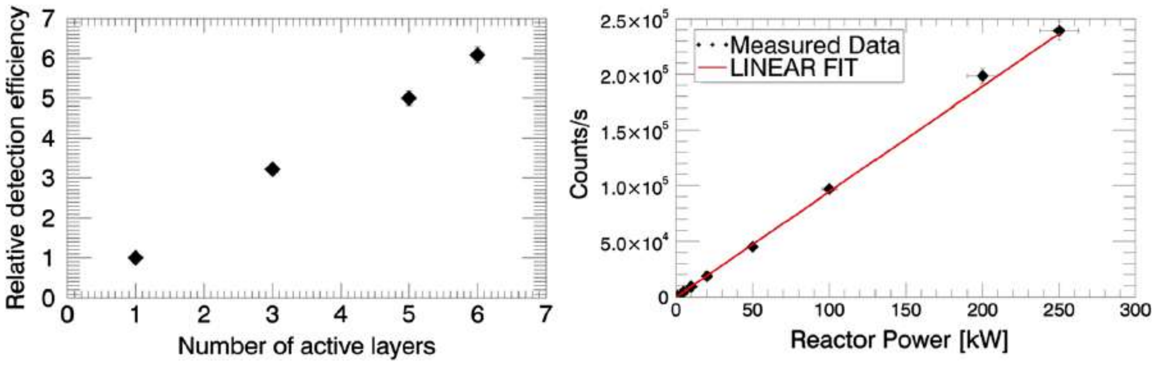

Fig. 11 On the left: relative detection efficiency measured as a function of the number of active converter layers. On the right: recorded counting rate on the detector as a function of the reactor power

converter layer) and the counting rate recorded with one, two or three BGEM set to 330 V (each active BGEM adds two active converter layers to the conversion stack). The result of this test is shown in Fig. 11, where the relative detection efficiency is reported as a function of the number of active converter layers.

As one can see, the measured relative neutron detection efficiency matches number of active converter layers, confirming the good charge extraction capability of the detector found in par. 3.1. The obtained results show that the detector is no lack of efficiency even when all the converter layers are active, giving the possibility to further increase the number of BGEMs and then to further increase the neutron detection efficiency. The last measurement was carried out in order to check the response of the detector under high neutron flux. The reactor power was varied from 1 to 250 kW, and the detector was set to the best HV configuration with all the BGEMs active. Figure 11 shows the recorded counting rate on the detector as a function of the reactor power.

As one can see, the detector response is almost linear up to 250 kHz corresponding to 250 kW of reactor power. This counting rate has been obtained with a neutron beam of 5 mm diameter that thus corresponds to a flux of 1.2 MHz/cm^2. Further study, with a dedicated electronic readout for very high counting rate applications, will be carried out in the future in order to investigate the behavior of the detector in the very high counting rate region.

In order to estimate the expected neutron detection efficiency, simple calculations have been performed considering an average neutron energy $E_n = 25$ meV. The calculation is performed by using the Beer–Lambert law:

$$I(E, x) = I_0 e^{-n\sigma(E_n)x} \tag{2}$$

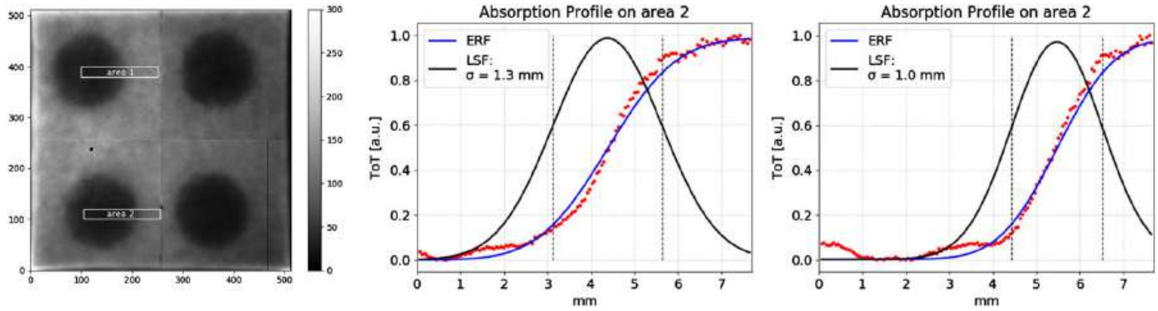

Fig. 12 On the left: the image obtained with 1-min exposition to the thermal neutron beam. On the right: the two profiles obtained from area 1 and area 2 (140 × 20 pixels) fitted with ERF and the corresponding LSF

where $I(E, x)$ is the transmitted intensity through a sample of density n and thickness x, I_0 is intensity before the sample, and $\sigma(E_n)$ is the total neutron cross section. Therefore the absorbed neutron intensity is defined as $I_0 - I = I_0(1 - e^{-n\sigma(E_n)x})$. By considering $\sigma(E_n = 25\ \text{meV}) = 3844\ b$, $n = 8.76 \times 10^{22}\ \text{nuclei/cm}^3$ and $x = 1\ \mu\text{m}$, a single layer absorption efficiency $p = 3\%$ is obtained. The escape probability ξ for $x = 1\ \mu\text{m}$ is about 65% [17], and the borated GEM foils have an optical transparency (ot) (ratio between empty and total area) of 78%. Therefore a total efficiency expected for six $^{10}B_4C$ stacked layers can be defined as $(1 - e^{-6n\sigma(E_n)x}) \times \xi \times ot \times \eta$. Assuming a unitary extraction efficiency η, the expected total efficiency is about 8.76%. Further measurement will be performed in order to assess this value by using an absolutely calibrated ^{3}He tube.

3.4 Spatial resolution

A first estimate of the spatial resolution has been performed using four disks of cadmium having a thickness of 1 mm and a diameter of 8 mm placed just in front of the detector. Neutron absorption from cadmium produces circular shadow images (see Fig. 12) that are obtained integrating the total charge released by alphas and Li ions after neutron absorption and, to a lesser extent, to gammas produced by unstable nuclei. The image has been acquired with an high voltage of 1120 V.

A measurement of the spatial resolution was obtained from the normalized edge response function (ERF) which has been calculated along the shadow edge profiles measured in area 1 and 2 as shown in Fig. 12. The length of this profile extends over 140 bins of 55 µm each, the content of which is filled with the mean value on 20 pixels along the orthogonal direction. These normalized profiles have been fitted with the ERF, obtaining the corresponding derivative line spread function (LSF). According to Sparrow criterion, two shadow images can be considered distinct if their separation is equal to 2σ of the LSF and this value can be considered a reasonable estimate of the spatial resolution ranging between 2.0 and 2.6 mm.

4 Conclusions and future work

A first batch of GEM foils with boron coating (1 µm thick $^{10}B_4C$) on both side was successfully realized and tested in a neutron detector equipped with a 3-layer converter readout by a GEMPix detector. All the six BGEMs produced passed the electrical tests, and three of them were used for the detector construction. The neutron characterization showed that in the optimized HV configuration, the MBGEM detector is able to increase the neutron detection efficiency obtained with a single layer of $^{10}B_4C$ by a factor directly proportional to the number of active converter foils, with a n/γ discrimination factor better than 10^5. With six layer of $^{10}B_4C$ the expected total efficiency is about 8.7%. The detector response is almost linear up to 250 kHz counting rate, corresponding to a flux of 1.2 MHz/cm^2. A preliminary study showed a spatial resolution ranging between $2.0 \div 2.6$ mm.

The obtained results suggest the possibility to further increase the neutron detection efficiency by augmenting the number of borated GEM foils in the converter stack. The next step is the production of a bigger detector with an active area $10 \times 10\,\mathrm{cm}^2$ with an higher number of BGEM foils and read out by the GEMINI DAQ system [31], for high counting rate applications. This detector will also be characterized in terms of absolute neutron detection efficiency by comparing its performance to an absolutely calibrated ^{3}He tube. These measurements will be subject of a future publication.

Acknowledgements We wish to thank various people for their contribution to this detector; M. Silari, M. Cambell, for their valuable financial and technical support on the development of the GEMPix detector; G. Corradi and D. Tagnani for the design of the high- voltage and readout boards, and finally J. Alozy for the software and hardware support on Timepix chips. Support from the Swedish Research Council VR-RFI (2017-00646-9) for the accelerator-based ion-technological center and from the Swedish Foundation for Strategic Research (Contract RIF14-0053) for the Tandem Accelerator Laboratory in Uppsala is gratefully acknowledged.

Funding Open Access funding provided by CERN.

References

1. F. Sauli, Nucl. Instrum. Methods Phys. Res. Sect. A Accel. Spectrom. Detect. Assoc. Equip. **386**, 531 (1997)
2. F. Murtas, Radiat. Meas. **138**, 106421 (2020)
3. R.T. Kouzes, OSTI.GOV: Technical Report (2009)
4. G.F. Knoll, *Radiation Detection and Measurement* (Wiley, New York, 2010)
5. G. Bencivenni, G. Felici, F. Murtas, P. Valente, W. Bonivento, A. Cardini, A. Lai, D. Pinci, B. Saitta, C. Bosio, Nucl. Instrum. Methods Phys. Res. Sect. A Accel. Spectrom. Detect. Assoc. Equip. **488**, 493 (2002)
6. G. Croci, G. Claps, M. Cavenago, M. Dalla Palma, G. Grosso, F. Murtas, R. Pasqualotto, E. Perelli Cippo, A. Pietropaolo, M. Rebai et al., Nucl. Instrum. Methods Phys. Res. Sect. A Accel. Spectrom. Detect. Assoc. Equip. **720**, 144 (2013), selected papers from the 2nd International Conference Frontiers in Diagnostic Technologies (ICFDT2)
7. G. Croci, M. Rebai, G. Claps, M. Cavenago, M.D. Palma, G. Gervasini, G. Grosso, F. Murtas, R. Pasqualotto, E.P. Cippo et al., J. Instrum. **7**, C03010 (2012)
8. F. Murtas, G. Croci, A. Pietropaolo, G. Claps, C.D. Frost, E.P. Cippo, D. Raspino, M. Rebai, N.J. Rhodes, E.M. Schooneveld et al., J. Instrum. **7**, P07021 (2012)
9. A. Muraro, G. Croci, G. Albani, G. Claps, M. Cavenago, C. Cazzaniga, M. Dalla Palma, G. Grosso, F. Murtas, R. Pasqualotto et al., Nucl. Instrum. Methods Phys. Res. Sect. A Accel. Spectrom. Detect. Assoc. Equip. **813**, 147 (2016)
10. M. Klein, C.J. Schmidt, Nucl. Instrum. Methods Phys. Res. Sect. A Accel. Spectrom. Detect. Assoc. Equip. **628**, 9 (2011)

11. G. Croci, G. Claps, R. Caniello, C. Cazzaniga, G. Grosso, F. Murtas, M. Tardocchi, E. Vassallo, G. Gorini, C. Horstmann et al., Nucl. Instrum. Methods Phys. Res. Sect. A Accel. Spectrom. Detect. Assoc. Equip. **732**, 217 (2013), Vienna Conference on Instrumentation 2013
12. G. Croci, A. Muraro, E.P. Cippo, M. Tardocchi, G. Grosso, G. Albani, G. Angella, I. Defendi, R. Hall-Wilton, C. Höglund et al., EPL (Europhys. Lett.) **123**, 52001 (2018)
13. A. Muraro, G. Croci, E. Perelli Cippo, G. Grosso, C. Höglund, G. Albani, R. Hall-Wilton, K. Kanaki, F. Murtas, D. Raspino et al., Prog. Theor. Exp. Phys. **2018**, 023H01 (2018)
14. A. Pietropaolo, G. Claps, A. Fedrigo, F. Grazzi, C. Hoglund, F. Murtas, A. Scherillo, S. Schmidt, E.M. Schooneveld, EPL **121**, 62001-1–62001-4 (2018)
15. A. Curioni, N. Dinar, F. La Torre, J. Leidner, F. Murtas, S. Puddu, M. Silari, Nucl. Instrum. Methods Phys. Res. Sect. A Accel. Spectrom. Detect. Assoc. Equip. **849**, 60 (2017)
16. G. Claps, D. Pacella, F. Murtas, K. Jakubowska, G. Boutoux, F. Burgy, J.E. Ducret, D. Batani, Rev. Sci. Instrum. **87**, 103505 (2016). https://doi.org/10.1063/1.4964731
17. C. Hoglund, J. Birch, K. Andersen, T. Bigault, J.C. Buffet, J. Correa, P. Van Esch, B. Guerard, R. Hall-Wilton, J. Jensen et al., J. Appl. Phys. **111**, 104908-1–104908-8 (2012)
18. F. Piscitelli, P.V. Esch, J. Instrum. **8**, P04020 (2013)
19. R. de Oliveira (2010), https://kt.cern/technologies/gas-electron-multiplier. Accessed 2021 CERN
20. C. Höglund, K. Zeitelhack, P. Kudejova, J. Jensen, G. Greczynski, J. Lu, L. Hultman, J. Birch, R. Hall-Wilton, Radiat. Phys. Chem. **113**, 14 (2015)
21. S. Schmidt, C. Hoglund, J. Jensen, L. Hultman, J. Birch, R. Hall-Wilton, J. Mater. Sci. **51**, 10418 (2016)
22. Y. Zhang, H.J. Whitlow, T. Winzell, I.F. Bubb, T. Sajavaara, K. Arstila, J. Keinonen, Nucl. Instrum. Methods Phys. Res. Sect. B Beam Interact. Mater. Atoms **149**, 477 (1999)
23. M. Moro, R. Holeňák, L. Zendejas Medina, U. Jansson, D. Primetzhofer, Thin Solid Films **686**, 137416 (2019)
24. H.Y. Qu, D. Primetzhofer, M.A. Arvizu, Z. Qiu, U. Cindemir, C.G. Granqvist, G.A. Niklasson, A.C.S. Appl, Mater. Interfaces **9**, 42420 (2017)
25. CAEN (2019). https://www.caen.it/products/A1561h/. Accessed 2021 CAEN
26. G. Corradi, F. Murtas, D. Tagnani, Nucl. Instrum. Methods Phys. Res. Sect. A Accel. Spectrom. Detect. Assoc. Equip. **572**, 96 (2007), frontier Detectors for Frontier Physics
27. X. Llopart, R. Ballabriga, M. Campbell, L. Tlustos, W. Wong, Nucl. Instrum. Methods Phys. Res. Sect. A Accel. Spectrom. Detect. Assoc. Equip. **581**, 485 (2007)
28. V. Kraus, M. Holik, J. Jakubek, M. Kroupa, P. Soukup, Z. Vykydal, J. Instrum. **6**, C01079 (2011)
29. D. Turecek, T. Holy, J. Jakubek, S. Pospisil, Z. Vykydal, J. Instrum. **6**, C01046 (2011)
30. LENA (2010). https://lena.unipv.it/en/homepage/. Accessed 2021 LENA
31. A. Pezzotta, G. Corradi, G. Croci, M. De Matteis, F. Murtas, G. Gorini, A. Baschirotto, *GEMINI: A Triple-GEM Detector Read-Out Mixed-Signal ASIC in 180 nm CMOS*, in *2015 IEEE International Symposium on Circuits and Systems (ISCAS)*, IEEE (IEEE, 345 E 47th St, New York, NY 10017 USA, 2015), IEEE International Symposium on Circuits and Systems, pp. 1718–1721, ISBN 978-1-4799-8391-9, ISSN 0271-4302, IEEE International Symposium on Circuits and Systems (ISCAS), Lisbon, PORTUGAL, MAY 24–27, 2015

Journal of Instrumentation

PAPER

Electronic readout characterisation of a new soft X-ray diagnostic for burning plasma

To cite this article: S. Cancelli *et al* 2022 *JINST* **17** C08028

Published by IOP Publishing for Sissa Medialab

Received: *February 11, 2022*
Accepted: *April 1, 2022*
Published: *August 30, 2022*

International Conference on Fusion Reactor Diagnostics
7–11 September, 2020
Villa Monastero, Varenna, Italy

Electronic readout characterisation of a new soft X-ray diagnostic for burning plasma

S. Cancelli,[a,b,*] A. Muraro,[c] E. Perelli Cippo,[c] A. Abba,[d] G. Corradi,[e] G. Grosso,[c] G. Gorini,[a,b,c] M.H. Kushoro,[a] F. Murtas,[e] O. Putignano,[a,b] J. Scionti,[c] D. Tagnani,[e] M. Tardocchi[b,c] and G. Croci[a,b,c]

[a] *University of Milano-Bicocca,*
Piazza della Scienza 3, Milano, Italy
[b] *INFN Sezione Milano-Bicocca,*
Piazza della Scienza 3, Milano, Italy
[c] *Istituto per la Scienza e Tecnologia dei Plasmi, CNR,*
via Cozzi 53, Milano, Italy
[d] *Nuclear Instrument SRL,*
Via Lecco 16, Lambrugo (Como), Italy
[e] *INFN-Laboratori Nazionali di Frascati,*
Via Enrico Fermi 40, Frascati, Italy

E-mail: stephanie.cancelli@unimib.it

Abstract: In fusion plasma scenario, soft X-rays are important tools to study impurities inside plasma. However state-of-the-art silicon detectors cannot survive for long time to the heavy damages due to harsh conditions in tokamaks. GEM detectors are a good alternative thanks to their resilience to radiation damage. In this paper, a GEM detector coupled with new dedicated electronic readout based on GEMINI chip is described. In particular, the detector response has been studied comparing the well established PH method and the ToT method implemented in GEMINI. The results indicate the possibility of using this electronic readout to do soft X-ray spectroscopy measurements in the energy range up to about 10–20 keV.

Keywords: Micropattern gaseous detectors (MSGC, GEM, THGEM, RETHGEM, MHSP, MICROPIC, MICROMEGAS, InGrid, etc.); Gaseous detectors; X-ray detectors

2022 JINST 17 C08028

---

[*] Corresponding author.

https://doi.org/10.1088/1748-0221/17/08/C08028

Contents

1 Introduction

Gas detectors based on Gas Electron Multiplier (GEM) [1] technology are nowadays widely used in different physics field, such as neutron physics [2–7], particle physics [8], medical physics [9] and plasma physics [10].

Belonging to the Micro Pattern Gas Detector (MPGD) category, GEM detectors distinguish themselves from other gas detectors by the possibility to cover large areas, good spatial resolution and detection efficiency, count rate stability and capability to sustain high rate (MHz).

Thanks to these features, in plasma physics, they are one of the prominent diagnostic to detect soft X-ray emissions [11]. The typical X-ray spectrum of a plasma shows several lines in the energy region from 2 keV up to 30 keV. These lines are due to the impurities inside plasma, therefore soft X-rays are an important tool to study their presence [12]. In this field, a detector with good energy resolution and capable to survive in harsh environments, such as tokamaks, is required. GEM detectors are good candidates specially if they are coupled with an electronic readout capable to sustain the high rate of the incoming events.

On this purpose, a custom electronic readout for GEM detectors, called GEMINI [13], has been designed by Istituto Nazionale di Fisica Nucleare (INFN) and Milano-Bicocca University.

This work provides the characterisation of the GEMINI chip whit a comparison between GEMINI digital (64D) system and GEMINI analog (64A) system. The aim of the characterisation is to verify that the digital GEMINI signals can be used to reconstruct an X-ray spectrum from burning plasma, at least at the point of identifying the main X-ray peaks.

2 The GEMINI chip and the entire electronic readout

GEMINI [14] is an ASIC designed in CMOS 180 nm technology made of 16 readout channels (features in table 1). From each channel (figure 1) the charge signal is converted to a voltage signal by a charge-sensitive preamplifier and this conversion is possible thanks to an auto-calibrated system on chip [15]. A discriminator compares the voltage signal with a threshold set by a Digital to Analog Converter (DAC) independently for each channel. A driver converts the output into a standard Low-Voltage differential signal (LVDS) [16], corresponding to digital signal with an offset of 1.2 V. The LVDS signal is given by the voltage difference on two connectors, represented by DOUTP and DOUTM in figure 1.

Table 1. GEMINI features.

Feature	GEMINI
CMOS technology	180 nm
N° of channels	16
Max pixel capacitance	40 pF
Max count rate	5 Mcps
Min detectable charge	2.5 fC

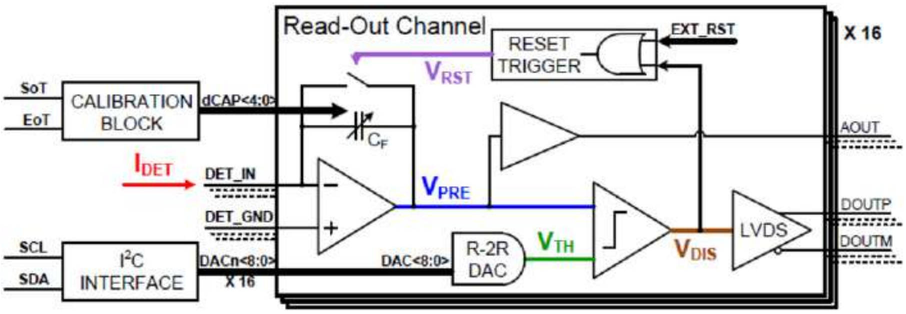

Figure 1. GEMINI scheme [15]. The analog signal is extracted directly from the preamplifier (V_{PRE}), labelled in the figure as *AOUT*. The digital signal output is labelled as *DOUT*.

The LVDS signal from GEMINI is processed by a custom FPGA, which provides the corresponding Time of Arrival (ToA) and Time over Threshold (ToT). The ToA corresponds to the time where the signal exceed the threshold and ToT is the time that the signal stays over threshold (figure 3). The information of each event is a 64 bit word containing information about ToT and the number of channel that records the event.

Data are transmitted by the FPGA to a server through an optical link; a custom made software allows to analyse the data and provides both ToT spectra and 2D spatial map of the recorded events (thanks to the padded nature of the used detector, see section 3 for details) in real time without overloading the system.

The entire readout allows to sustain up to 5 Mcps count rate without loss of information.

3 The experimental set-up

The characterisation has been performed at the Istituto per la Scienza e Tecnologia del Plasma (ISTP) of CNR and Milano-Bicocca University laboratories.

2022 JINST 17 C08028

The set-up (figure 2) is composed of a X-ray source Amptek MINI-X [17], directed to a suitable target (and namely titanium, copper and molybdenum) only to detect the X-ray fluorescence photons emitted from the latter (4.5 keV, 8 keV and 17 keV respectively). The GEM detector has been built with three aluminium GEM foils, a padded anode (256 pads of $6 \times 6\,\mathrm{mm}^2$) and coupled with the GEMINI system. For this analysis only 32 pads have been considered and 8 of these have been also connected at a custom module able to extract the analog signal from the preamplifier of the GEMINI chip (figure 1). The 8 channels have been connected to a QDC — DT5730B CAEN digitizer. The entire system was positioned inside a steel-wall shielding chamber; the shielding material is thus a source of spurious peaks due to X-ray fluorescence background of the wall. Other possible sources of background are the materials of the detector itself, that are invested by the X-rays from the target, like for instance copper (present in the anode and circuits) and the argon (used with CO_2 as a multiplication gas in GEMs).

2022 JINST 17 C08028

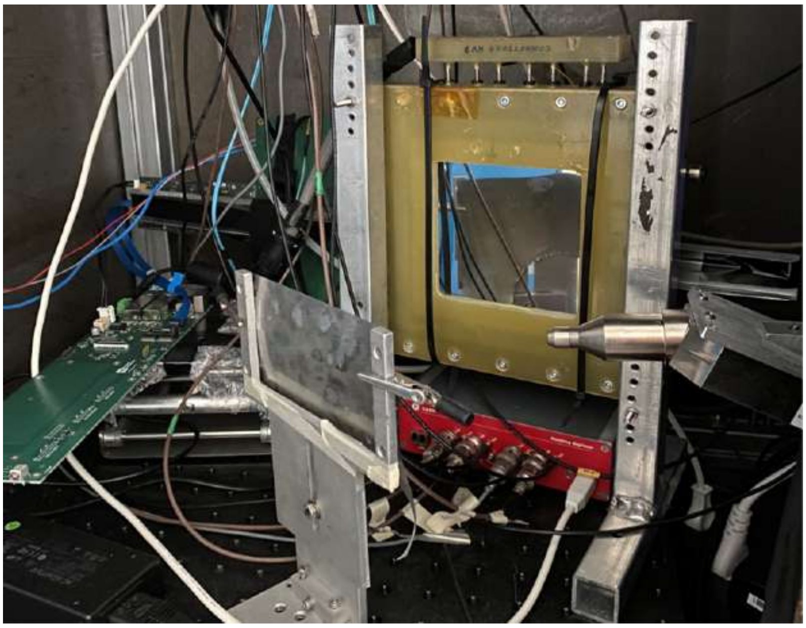

Figure 2. Experimental set-up: the X-ray source at ISTP-CNR laboratory, the molybdenum target, the Al-GEM detector and the electronic readout.

4 GEMINI response analysis

Aim of the characterisation is to extract both the analog and the digital signals from GEMINI and study them at the same time in order to verify that ToT digital technique allows to reconstruct spectra. The analysis has been conducted via a comparison between two copies of the same signal (the X-ray measurement) from the analog and digital output of GEMINI. From the analog signals the Pulse High (PH) and the ToT spectra have been obtained in order to verify their correspondence; the comparison has been performed after the conversion of the ToT and PH spectra into deposited charge spectra (see subsection 4.1). The ToT spectra obtained from the analog signals have been compared with the analogues ToT spectra from the digital channels.

4.1 GEMINI analog system

The analog signal from GEMINI chip is digitized with 500 Ms/s and 10 bit resolution to obtain the waveform for every single event (figure 3).

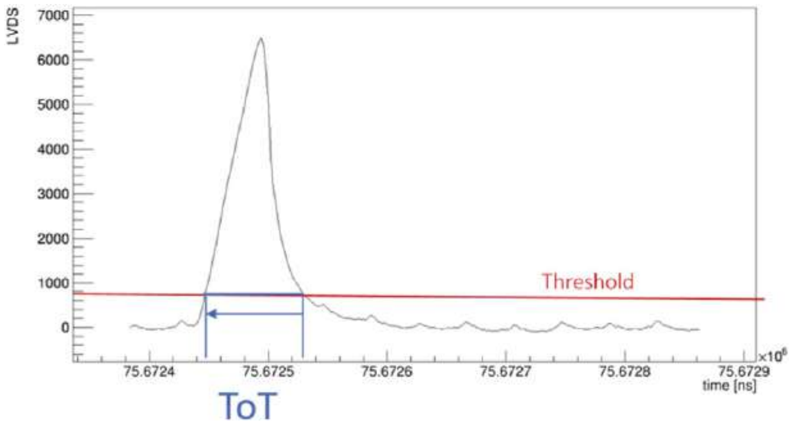

Figure 3. Waveform of an event from the analog signal with the set threshold. The difference between the time when the signal exceed the threshold and the signal goes under the threshold is the ToT.

For each waveform a threshold of 700 LVDS has been set and considering the time where the signal stays over the threshold and the pulse integral over the threshold, both ToT and PH spectra have been obtained (figure 4) for each chip channel. For sake of simplicity, only the data of a single reference channel are reported.

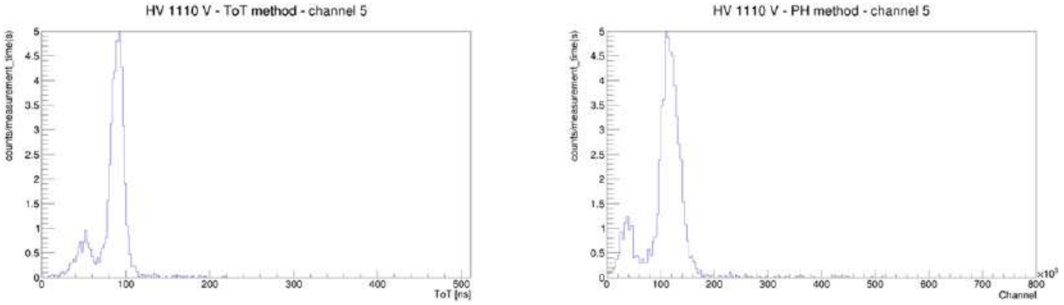

Figure 4. Left: spectrum of a titanium target obtained with ToT method. Right: spectrum of a titanium target obtained with PH method. Both spectra are reconstructed through the analog signals collected by the GEMINI chip. The main peak is the 4.5 keV Kα line from titanium; the small peak at the left is identified as the argon escape peak at 1.5 keV.

Both PH and TOT spectra show a prominent peak, the position of which depends on both the energy of the X-ray line and the detector gain. The X-ray photon in fact deposits energy into the GEM filling gas, creating a number of charged couples (ion-e) depending on the initial photon

2022 JINST 17 C08028

energy; the electrons are collected by the anode after being multiplied by the GEM stages and the amount of multiplication depends on the detector gain. Thus decreasing the detector gain, the main peak shifts to the left. Gaussian-fitting each peak at different gains, the peak positions vs. charge have been plotted in order to obtain the calibration curve for both methods, as shown in figure 5. For a direct comparison, spectra obtained with both methods have to be represented as a function of the deposited charge, that can be exactly calculated by an analytical method ([11]) for all the X-ray photons and different gains.

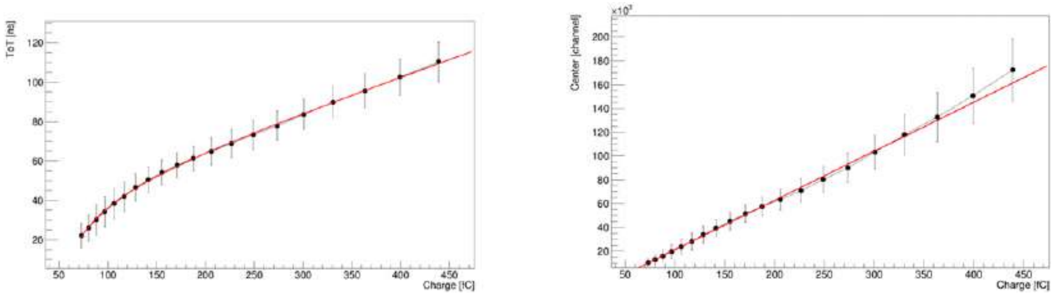

Figure 5. Left: calibration curve for ToT method. The ToT points have been found fitting the ToT spectra of titanium target at different gains. The relative charge values have been calculated inverting the equation (4.2). The calibration curve has been fit with equation (4.1). Right: calibration curve of the PH method fit with a straight line. The charge values have been obtained with the same procedure of the figure reported on the right.

The ToT vs. charge (at different gains) calibration curve has been fit with

$$\text{ToT} = a * q + b - \frac{c}{q - d} \tag{4.1}$$

where q is the deposited charge and a–d are the fit parameters. The PH calibration curve was fit with a straight line. Making use of the fit parameters, the charge spectra and eventually the energy spectra for both methods can be obtained through:

$$E_i = \frac{q_i * E_{\text{ion}}}{e * G * K} \tag{4.2}$$

where q_i is the deposited charge, E_{ion} is the ionization energy (28 eV for the ArCO_2 gas mixture), e is the electron charge, G the detector gain and K is the gain corrective factor [11] given by

$$K = \frac{\text{Measured energy}}{\text{Expected energy}}.$$

Since the calibration curves for each channel provide energy calibrated spectra, it is possible to sum the spectra in order to improve the statistic. In fact, in figure 6 the energy spectra of titanium, copper and molybdenum of three pads are reported for both methods with reference HV = 1110 V, corresponding to $G = 12914$. The table 2 reports the results of the fit (centroid and σ) of the spectra obtained from the analog signals for both ToT and PH method. These values indicate the agreement of the two methods and not the ultimate resolution of the detector. With this consideration, the two obtained spectra are compatible, thus it is possible use the ToT method to reconstruct X-ray spectra.

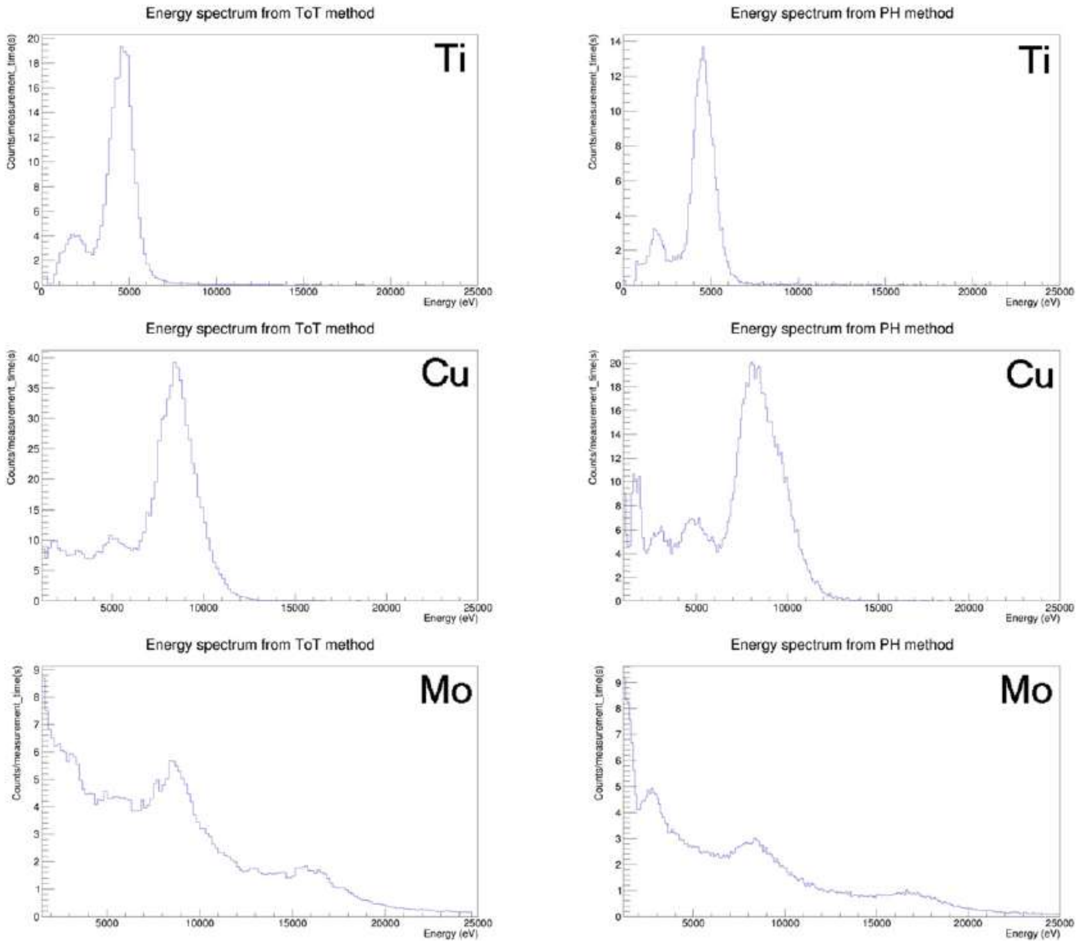

Figure 6. Energy spectra of titanium (Ti), copper (Cu) and molybdenum (Mo) obtained with the ToT (left) and PH (right) method. The main peaks are the evidenced ones (energy values in table 2); other visible structures, like argon escape peaks (at 1.5 keV) or background peaks, are not to be considered in this analysis.

Table 2. Table with center and σ values obtained with a Gaussian fit of the energy spectra reported in figure 6 for the ToT method and for the PH method.

Targets	$\mathrm{Peak_{ToT}}$ (eV)	σ_{ToT} (eV)	$\mathrm{Peak_{PH}}$ (eV)	σ_{PH} (eV)
Ti	4555	706	4589	601
Cu	8500	1174	8500	1337
Mo	15800	1286	16600	1981

As shown in figure 7, the peak centroids obtained with ToT and PH spectra from analog signals for each targets are superimposed and within the errors; because we consider that the peak positions are the main parameters to be considered, thus we conclude that the two methods are well compatible.

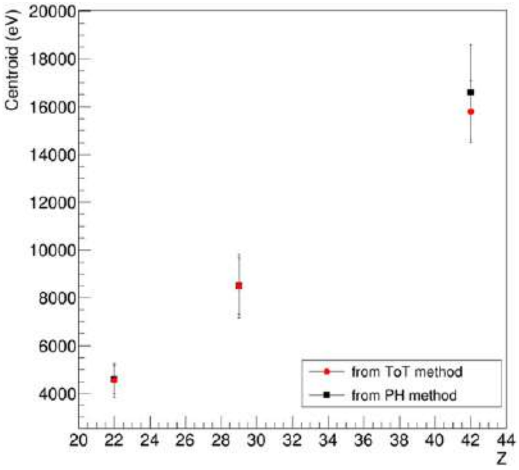

Figure 7. Compatibility of ToT and PH method. The centroids of the X-ray peaks obtained from each target (identified by its atomic number Z) have been plotted with the relative errors given by the σ. The values are well compatible within the errors.

4.2 Comparison between analog and digital system

As mention made before, analog and digital signals have been obtained from GEMINI ASIC at the same time. The digital ToT signals were also analysed in order to obtain the spectra of all the reference targets in table 2. For sake of simplicity in figure 8 it is shown only a comparison between the ToT spectra of the titanium target obtained from the analog and the digital signals from the same measurement. The two spectra showing no sign of significant differences, we conclude that GEMINI provides the same results as a common digitizer and thus its ToT spectra can be used for X-ray identification with GEM detectors.

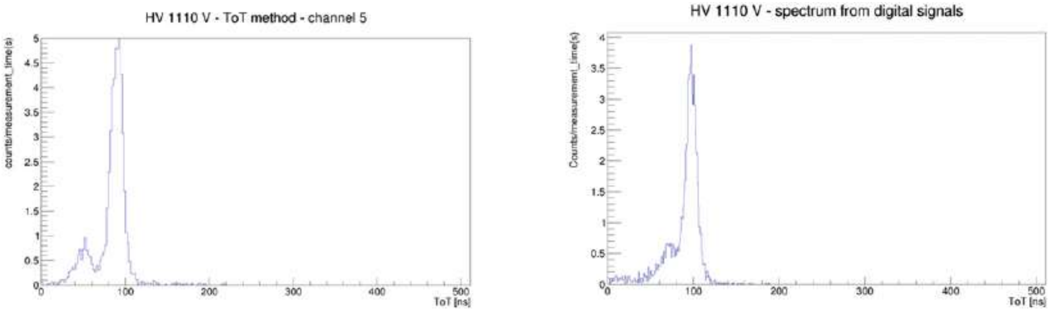

Figure 8. Left: ToT titanium spectrum obtained from analog signals. Right: ToT titanium spectrum obtained from digital signals. Both spectra are obtained from the same measurement.

5 Conclusions

The GEMINI analog and the digital electronic readout systems provide compatible results at least in terms of X-ray peaks position reconstruction when coupled to a GEM detector. The analysis shows some limits due to the calibration PH-deposited energy-ToT method until 20 keV and due to presence of the peaks from the copper from the surroundings. Nevertheless, it is possible to support that GEMINI can provide reasonable X-ray spectra with the digital ToT method. Because when operating in digital ToT mode the GEMINI can sustain high count rate with a high number of channels [15], therefore it is a good candidate to be used with GEM detector during burning plasma experiments to detect soft X-rays.

Acknowledgments

This work has been carried out within the framework of the EUROfusion consortium and has received funding from the Euratom Research and Training Programme 2019–2020 under Grant Agreement No. 633053. The views and opinions expressed herein do not necessarily reflect those of the European Commission.

References

[1] F. Sauli, *The gas electron multiplier (GEM): operating principles and applications*, *Nucl. Instrum. Meth. A* **805** (2016) 2.

[2] F. Murtas et al., *Triple GEM gas detectors as real time fast neutron beam monitors for spallation neutron sources*, 2012 *JINST* **7** P07021.

[3] G. Croci et al., *nGEM fast neutron detectors for beam diagnostics*, *Nucl. Instrum. Meth. A* **720** (2013) 144.

[4] G. Croci et al., *Discharge probability measurement of a triple GEM detector irradiated with neutrons*, *Nucl. Instrum. Meth. A* **712** (2013) 108.

[5] S. Cancelli et al., *Development of a ceramic double thick GEM detector for transmission measurements at the VESUVIO instrument at ISIS*, 2021 *JINST* **16** P06003.

[6] G. Croci et al., *GEM-based detectors for thermal and fast neutrons*, *Eur. Phys. J. Plus* **130** (2015) 118.

[7] G. Croci et al., *I-BAND-GEM: a new way for improving BAND-GEM efficiency to thermal and cold neutrons*, *Eur. Phys. J. Plus* **134** (2019) 166.

[8] G. Bencivenni et al., *A triple GEM detector with pad readout for high rate charged particle triggering*, *Nucl. Instrum. Meth. A* **488** (2002) 493.

[9] J. Leidner et al., *3D energy deposition measurements with the GEMPix detector in a water phantom for hadron therapy*, 2018 *JINST* **13** P08009.

[10] A. Muraro et al., *Directionality properties of the nGEM detector of the CNESM diagnostic system for SPIDER*, *Nucl. Instrum. Meth. A* **916** (2019) 47.

[11] A. Muraro et al., *Development and characterization of a new soft X-ray diagnostic concept for tokamaks*, 2019 *JINST* **14** C08012.

2022 JINST 17 C08028

[12] S. Von Goeler et al., *Thermal X-ray spectra and impurities in the ST tokamak*, *Nucl. Fusion* **15** (1975) 301.

[13] L. Mangiagalli et al., *Characterization of GEMINI, a 16-channels programmable readout interface for triple-GEM detectors in 180 nm CMOS*, *PoS* **TWEPP2018** (2019) 165.

[14] *Nuclear Instrument webpage*, http://nuclearinstruments.eu.

[15] A. Pezzotta et al., *GEMINI: a triple-GEM detector read-out mixed-signal ASIC in 180 nm CMOS*, *IEEE — International Symposium on Circuits and Systems (ISCAS)* (2015).

[16] TIA, *TIA/EIA-644: Electrical Characteristics of Low Voltage Differential Signaling (LVDS) Interface Circuits*.

[17] *Amptek website*, https://amptek.com/.

2022 JINST 17 C08028

Bibliography

[1] J. Chadwick. “The existence of a Neutron”. In: *Proceedings of the Royal Society of London. Series A, Containing Papers of a Mathematical and Physical Character* 136.830 (1932).

[2] G. Knoll. *Radiation Detection and Measurement.* Ed. by Wiley. 4th. 2010.

[3] Raymond L. Murray and Keith E. Holbert. *Chapter 6 - Fission.* Ed. by Raymond L. Murray and Keith E. Holbert. Eighth Edition. Butterworth-Heinemann, 2020, pp. 101–114.

[4] C. Windsor. *Pulsed neutron scattering.* Jan. 1981.

[5] A. Oed. “Position-sensitive detector with microstrip anode for electron multiplication with gases”. In: *Nuclear Instruments and Methods in Physics Research Section A: Accelerators, Spectrometers, Detectors and Associated Equipment* 263.2 (1988), pp. 351–359.

[6] A. Barr et al. “Construction, test and operation in a high intensity beam of a small system of micro-strip gas chambers”. In: *Nuclear Instruments and Methods in Physics Research Section A: Accelerators, Spectrometers, Detectors and Associated Equipment* 403.1 (1998), pp. 31–56.

[7] P. Abbon et al. “The COMPASS experiment at CERN”. In: *Nuclear Instruments and Methods in Physics Research Section A: Accelerators, Spectrometers, Detectors and Associated Equipment* 577.3 (2007), pp. 455–518.

[8] K. Abe et al. “The T2K experiment”. In: *Nuclear Instruments and Methods in Physics Research Section A: Accelerators, Spectrometers, Detectors and Associated Equipment* 659.1 (Dec. 2011), pp. 106–135.

[9] G Charpak et al. "Micromegas, a multipurpose gaseous detector". In: *Nuclear Instruments and Methods in Physics Research Section A: Accelerators, Spectrometers, Detectors and Associated Equipment* 478.1 (2002). Proceedings of the ninth Int.Conf. on Instrumentation, pp. 26–36.

[10] M. Abbrescia et al. "Beam test results on double-gap resistive plate chambers proposed for CMS experiment". In: *Nuclear Instruments and Methods in Physics Research Section A: Accelerators, Spectrometers, Detectors and Associated Equipment* 414.2 (1998), pp. 135–148.

[11] Piet Verwilligen and on behalf of the CMS Muon group. "GEM detectors for the CMS endcap muon system: status of three new detector stations". In: *Journal of Instrumentation* 18.07 (July 2023), p. C07006.

[12] J. Leidner et al. "3D energy deposition measurements with the GEMPix detector in a water phantom for hadron therapy". In: *Journal of Instrumentation* 13.08 (Aug. 2018), P08009.

[13] D. Mazon et al. "First GEM measurements at WEST and perspectives for fast electrons and heavy impurities transport studies in tokamaks". In: *Journal of Instrumentation* 17.01 (Jan. 2022), p. C01073.

[14] Fabio Sauli. "The gas electron multiplier (GEM): Operating principles and applications". In: *Nuclear Instruments and Methods in Physics Research Section A: Accelerators, Spectrometers, Detectors and Associated Equipment* 805 (2016), pp. 2–24.

[15] Fabio Sauli. *Gaseous radiation detectors : fundamentals and applications.* Cambridge University press, 2014.

[16] A. Muraro et al. "Performance of the full size nGEM detector for the SPIDER experiment". In: *Nuclear Instruments and Methods in Physics Research Section A: Accelerators, Spectrometers, Detectors and Associated Equipment* 813 (2016), pp. 147–152.

[17] CERN Gas detector group site. "https://gdd.web.cern.ch/gem-compass". In: ().

[18] G CROCI et al. *GEM-based detectors for thermal and fast neutrons.* Springer Verlag, 2015.

[19] G. Bencivenni et al. "Measurement of GEM parameters with X-rays". In: *IEEE Transactions on Nuclear Science* 50.5 (2003), pp. 1297–1302.

[20] Geant4 website. In: *https://geant4.web.cern.ch/* ().

[21] CERN website. In: *https://home.cern/* ().

[22] CATiA website. In: *https://www.3ds.com/it/prodotti-e-servizi/catia/* ().

[23] Dana Shea and D. Morgan. "The Helium-3 Shortage: Supply, Demand, and Options for Congress". In: *Congressional Research Service* (Jan. 2011), R41419.

[24] G. Croci et al. "GEM-based thermal neutron beam monitors for spallation sources". In: *Nuclear Instruments and Methods in Physics Research Section A: Accelerators, Spectrometers, Detectors and Associated Equipment* 732 (2013). Vienna Conference on Instrumentation 2013, pp. 217–220.

[25] Gabriele Croci et al. "I-BAND-GEM: a new way for improving BAND-GEM efficiency to thermal and cold neutrons". In: *Eur. Phys. J. Plus* 134.4 (2019), p. 166.

[26] Martin Klein and Christian Schmidt. "CASCADE, neutron detectors for highest count rates in combination with ASIC/FPGA based readout electronics". In: *Nuclear Instruments and Methods in Physics Research Section A: Accelerators, Spectrometers, Detectors and Associated Equipment* 628 (Feb. 2011), pp. 9–18.

[27] G Muraro et al. "MBGEM: a stack of borated GEM detector for high efficiency thermal neutron detection". In: *The European Physical Journal Plus* 136 (2021).

[28] Lawrence S. Pinsky and Stanislav Pospisil. "Timepix-based detectors in mixed-field charged-particle radiation dosimetry applications". In: *Radiation Measurements* 138 (2020), p. 106229.

[29] Amptek MiniX2 X-Ray Tube website. In: *https://www.amptek.com/products/mini-x2-x-ray-tube* ().

[30] National Instruments website Labview. In: *https://www.ni.com/it-it/shop/product/labview.html* ().

[31] Antonio Cammi et al. "Characterization of the TRIGA Mark II reactor full-power steady state". In: *Nuclear Engineering and Design* 300 (2016), pp. 308–321.

[32] Laboratorio di Energia Nucleare Applicata website. In: *https://lena.unipv.it/il-reattore/* ().

[33] Giulia Marcucci. "New advances in neutron imaging techniques and a quantitative development of Neutron Resonance Transmission Imaging". PhD thesis. Università degli Studi Milano-Bicocca, 2023.

[34] R. W. Stoughton and J. Halperin. “Effective Cutoff Energies for Boron, Cadmium, Gadolinium, and Samarium Filters”. In: *Nuclear Science and Engineering* 15.3 (1963), pp. 314–324.

[35] ISIS Neutron and Muon Source website. In: *https://www.isis.stfc.ac.uk/Pages/home.aspx* ().

[36] Adrian Hillier et al. “Muons at ISIS”. In: *Philosophical Transactions of The Royal Society A Mathematical Physical and Engineering Sciences* 377 (Dec. 2018), p. 20180064.

[37] A G Seel, M Krzystyniak, and F Fernandez-Alonso. “The VESUVIO Spectrometer Now and When?” In: *Journal of Physics: Conference Series* 571.1 (Dec. 2014), p. 012006.

[38] GS20 scintillator website. In: *https://scintacor.com/products/6-lithium-glass/* ().

[39] G Romanelli et al. “Characterisation of the incident beam and current diffraction capabilities on the VESUVIO spectrometer”. In: *Measurement Science and Technology* 28.9 (Aug. 2017), p. 095501.

[40] Andrea Muraro et al. “Performance of the high-efficiency thermal neutron BAND-GEM detector”. In: *Progress of Theoretical and Experimental Physics* 2018.2 (Feb. 2018), 023H01. eprint: `https://academic.oup.com/ptep/article-pdf/2018/2/023H01/24195547/pty005.pdf`.

[41] S. Cancelli et al. “Development of a ceramic double thick GEM detector for transmission measurements at the VESUVIO instrument at ISIS”. In: *Journal of Instrumentation* 16.06 (June 2021), P06003.

[42] Giovanni Romanelli et al. “Thermal neutron cross sections of amino acids from average contributions of functional groups”. In: *Journal of Physics: Condensed Matter* 33.28 (May 2021), p. 285901.

[43] Ken Andersen and Colin Carlile. “A Proposal for a Next Generation European Neutron Source”. In: *Journal of Physics: Conference Series* 746 (Sept. 2016), p. 012030.

[44] W Bonivento et al. “Development of the CARIOCA front-end chip for the LHCb muon detector”. In: *Nuclear Instruments and Methods in Physics Research Section A: Accelerators, Spectrometers, Detectors and Associated Equipment* 491.1 (2002), pp. 233–243.

[45] A. Pezzotta et al. “GEMMA and GEMINI, two dedicated mixed-signal ASICs for Triple-GEM detectors readout”. In: *Journal of Instrumentation* 11.03 (Mar. 2016), p. C03058.

[46] A. Muraro et al. “Development and characterization of a new soft x-ray diagnostic concept for tokamaks”. In: *Journal of Instrumentation* 14.08 (Aug. 2019), p. C08012.

[47] Amptek M. *Mini-X2 X-Ray tube system for XRF.*

[48] S. Cancelli et al. “Electronic readout characterisation of a new soft X-ray diagnostic for burning plasma”. In: *Journal of Instrumentation* 17.08 (Aug. 2022), p. C08028.

[49] S. Von Goeler et al. “Thermal X-ray spectra and impurities in the ST Tokamak”. In: *Nuclear Fusion* 15.2 (Apr. 1975), p. 301.

[50] Federico Caruggi et al. “Performance of a triple GEM detector equipped with Al-GEM foils for X-rays detection”. In: *Nuclear Instruments and Methods in Physics Research Section A: Accelerators, Spectrometers, Detectors and Associated Equipment* 1047 (2023), p. 167855.

[51] CC800/9 (CemeCon) sputtering machine site. In: *https://catalog.cemecon.com/en/pvd-technology/* ().

[52] B. Despax and J.L. Flouttard. “Synthesis of gold carbon composites by simultaneous sputtering and plasma polymerization of propane in r.f. capacitively coupled diode system (13.56 MHz)”. In: *Thin Solid Films* 168.1 (1989), pp. 81–88.

[53] Richard T. Kouzes et al. “Neutron detection alternatives to 3He for national security applications”. In: *Nuclear Instruments and Methods in Physics Research Section A: Accelerators, Spectrometers, Detectors and Associated Equipment* 623.3 (2010), pp. 1035–1045.